UQAC
Université du Québec
à Chicoutimi

OPTIMISATION DU LIT RÉSISTIF DANS CUVES D'ÉLECTROLYSE PENDANT LA PHASE DE PRÉCHAUFFAGE

Par **Rohini Nandan Tripathy**

UN MÉMOIRE PRÉSENTÉ À
L'UNIVERSITÉ DU QUÉBEC À CHICOUTIMI
COMME EXIGENCE PARTIELLE
DE LA MAÎTRISE EN INGÉNIERIE

Membres du jury :

Prof. Daniel Marceau, *Directeur de recherche, UQAC*
Prof. Duygu Kocaefe, *Codirecteur de recherche, UQAC*
Prof. Lukas Dion, *Évaluateur externe, UQAC*
Prof. émérite Halvor Kvande, *Évaluateur externe, NTNU*

Avril 2026
Centre universitaire de recherche sur l'aluminium (CURAL)
Saguenay, Québec, Canada

UQAC
Université du Québec
à Chicoutimi

OPTIMISATION OF THE LYING-BED IN ALUMINIUM REDUCTION CELLS DURING PREHEATING PHASE

By **Rohini Nandan Tripathy**

A THESIS SUBMITTED TO
THE UNIVERSITY OF QUEBEC AT CHICOUTIMI
IN PARTIAL FULFILMENT OF THE REQUIREMENTS FOR THE
DEGREE OF MASTER OF ENGINEERING

Jury Members :

Prof. Daniel Marceau, *Research Director, UQAC*
Prof. Duygu Kocaefe, *Research Co-director, UQAC*
Prof. Lukas Dion, *External Evaluator, UQAC*
Emeritus Prof. Halvor Kvande, *External Evaluator, NTNU*

April 2026
University Research Centre on Aluminium (CURAL)
Saguenay, Quebec, Canada

With love and gratitude,
dedicated to my parents:

Bijaylaxmi Tripathy
Rama Chandra Tripathy

for their endless love & support

ABSTRACT

The Hall–Héroult process remains the only industrially viable method for commercial primary aluminium production, despite ongoing efforts to decarbonise and improve its environmental performance. Aluminium reduction cells operate at elevated temperature with expensive cathode linings, whose performance and longevity are strongly influenced by start-up and early operational conditions.

Preheating of aluminium reduction cells is a critical transitional phase during which the cathode temperature rises from ambient to cell operating temperature. This phase involves significant thermal, electrical, chemical, and mechanical changes. Thus, improper preheating can cause thermal shock, deformation, and reduced cathode life. Consequently, effective preheating is essential for stable early operation, extended cell lifetime, and enhanced smelter productivity.

Modern smelters, particularly those using (semi- or fully-) graphitic or graphitised cathode blocks, increasingly adopt electrical preheating with a lying-bed due to its economic advantages. The lying-bed typically consists of a mixture of calcined petroleum coke and graphite (granular blends), and its thermal and electrical properties vary with temperature and applied pressure, making conventional trial-and-error optimisation challenging.

In this work, the physical and electrical properties of the granular blends used in lying-bed were experimentally characterised. The physical properties were used to optimise the lying-bed configurations, while the electrical properties were fed into thermo-electrical simulations. The results demonstrate the influence of blend coke content on both physical and electrical behaviour, highlighting its critical role in optimising preheating process. These findings provide the foundation of practical guidelines for improved electrical preheating strategies and contribute to enhanced performance and longevity of modern aluminium reduction cells.

RÉSUMÉ

Malgré les efforts continus visant à décarboner le procédé et à améliorer sa performance environnementale, le procédé Hall–Héroult demeure la seule méthode industriellement viable pour la production commerciale d'aluminium primaire. Les cuves d'électrolyse de l'aluminium fonctionnent à haute température avec des revêtements cathodiques coûteux, dont la performance et la longévité dépendent fortement des conditions de démarrage et des premières phases de fonctionnement.

Le préchauffage des cuves d'électrolyse de l'aluminium constitue une phase transitoire critique au cours duquel la température de la cathode augmente de la température ambiante à la température d'opération de la cuve. Cette phase implique des changements thermiques, électriques, chimiques et mécaniques importantes, et un préchauffage inadéquat peut provoquer des chocs thermiques ainsi que des gradients de déformation importants pouvant altérer la durée de vie de la cathode. Par conséquent, un préchauffage efficace est essentiel pour un fonctionnement stable des premières heures, une longévité prolongée de la cuve et une productivité accrue de l'aluminerie.

Les alumineries modernes, en particulier cuves utilisant des blocs cathodiques semi-graphitiques ou graphitisés, adoptent de plus en plus le préchauffage électrique à l'aide d'un lit de préchauffage en raison de ses avantages économiques. Le lit de préchauffage est généralement constitué d'un mélange de coke de pétrole calciné et de graphite, dont les propriétés thermiques et électriques varient en fonction de la température et de la pression appliquée, rendant l'optimisation par essai-erreur conventionnel difficile.

Dans ce travail, les propriétés physiques et électriques de différents mélanges de coke et graphite ont été caractérisées expérimentalement. Les propriétés physiques ont été utilisées pour optimiser les configurations du lit de préchauffage, tandis que les propriétés électriques ont servi à alimenter des simulations thermoélectriques. Les résultats montrent l'influence de la teneur en coke du mélange sur le comportement physique et électrique, soulignant son rôle crucial dans l'optimisation du préchauffage. Ces résultats fournissent une base pour des recommandations pratiques visant à améliorer les stratégies de préchauffage électrique et contribuent à la performance ainsi qu'à la longévité des cuves d'électrolyse modernes.

ACKNOWLEDGEMENT

The author gratefully acknowledges Aluminerie Alouette Inc. (AAI), Sept-Îles, Québec, for its invaluable support as the industrial partner of this project. This research was made possible through the financial support of Aluminerie Alouette Inc. (AAI) and the Fonds de recherche du Québec – Nature et technologies (FRQNT).

The author also acknowledges the Université du Québec à Chicoutimi (UQAC), the Centre universitaire de recherche sur l'aluminium (CURAL), and the Regroupement stratégique sur l'aluminium (REGAL) for their association during this project and for providing access to essential research facilities, including the Geotechnical Laboratory and the Groupe de recherche en ingénierie des procédés et systèmes (GRIPS), which were instrumental in conducting this work.

First, I would like to express my heartfelt gratitude to my project director, Prof. Daniel Marceau, for providing me with this research opportunity at the Centre Universitaire de Recherche sur l'Aluminium (CURAL). He has consistently guided me in the right direction whenever needed. His support, understanding, and trust in me have been invaluable.

I would also like to extend my sincere appreciation to my project co-director, Prof. Duygu Kocaefe, for her encouragement throughout this research. Additionally, I am deeply grateful to Prof. Yasar Kocaefe for his valuable insights and constructive feedback which helped broaden my research perspectives.

A special acknowledgment goes to my friend and research professional, Mr. Simon-Olivier Tremblay, whom I first met at the 2013 TMS Industrial Aluminium Electrolysis Course in Doha, Qatar. I am also truly thankful to our talented technician, Mr. Martin Truchon, and research professional, Mr. Guillaume Bonneau, for their unwavering assistance, kindness, patience, and technical expertise throughout the experimental phases of this work.

I would like to highlight the profound inspiration I have drawn from Prof. Halvor Kvande, who has been a guiding force in addressing my queries related to aluminium smelting since my early professional days. Additionally, Prof. Barry J. Welch played a pivotal role in inspiring me during my Postgraduate Certificate in Light Metals Reduction Technology at The University of Auckland (UoA), New Zealand.

I am also grateful to my friends and colleagues for their unwavering support and companionship. A heartfelt thanks to Mr. Alexandre Rufin, who not only welcomed me into his home but also into his heart when I first arrived in the Saguenay-Lac-Saint-Jean region. I also deeply appreciate the teachers who helped me learn French, an essential skill for living and integrating here.

Finally, I wish to express my deepest love and gratitude to both my parents for their continuous support, unconditional love, and unwavering faith in me from an early age, which shaped my dreams into reality. None of this would have been possible without the passion they ignited in me. Finally, I offer a heartfelt and special thanks to my loving mother for her endless support, patience, and encouragement throughout this journey.

TABLE OF CONTENTS

LIST OF FIGURES

LIST OF TABLES

GLOSSARY OF ACRONYMS

Acronym	Definition
AAI	Aluminerie Alouette Inc.
ABRF	Anode Beam Raising Frame
ACD	Anode to Cathode Distance
ACM	Anode Covering Material
AE	Anode Effect
AED	Anode Effect Duration
AEF	Anode Effect Frequency
BET	Brunauer-Emmett-Teller
BR	Bath Ratio
CAD	Canadian Dollar
CAGR	Compound Annual Growth Rate
CE	Current Efficiency
CR	Cryolite Ratio
DC	Direct Current
DPCS	Dense Phase Conveying System
ECC	Electrical Contact Conductance
ECE	Electrochemical Equivalent
EE	Energy Efficiency
FM	Fineness Modulus
FTP	Fume Treatment Plant
GCC	Gross Carbon Consumption
GHG	Green House Gas

Acronym	Definition
GP	Global Performance
GRG	Generalized Reduced Gradient
GTC	Gas Treatment Centre
HDPS	Hyper Dense Phase System
HSS	Horizontal Stud Söderberg
IAI	International Aluminium Institute
KPI	Key Performance Indicator
LoI	Loss on Ignition
LRF	Laboratoire de recherches des fabrications
NEUI	Northeastern University Engineering & Research Institute
NCC	Net Carbon Consumption
PI	Performance Indicator
PSD	Particle Size Distribution
PTA or PTM	Pot Tending Assembly or Pot Tending Machine
RSD	Relative Standard Deviation
SDG	Sustainable Development Goal
SEC	Specific Energy Consumption
SECR	Specific Electrical Contact Resistivity
SF	Scaling Factor
SGA	Smelter Grade Alumina
SPL	Spent Pot Lining
TCC	Thermal Contact Conductance
VSS	Vertical Stud Söderberg

GLOSSARY OF SYMBOLS

Symbol	Definition	Unit
a	Length	$[\,m\,]$
C_s	Cohesive strength	$[\,Pa\,]$
c	Blend coke content	$[\,-\,]$
C_c	Coefficient of curvature	$[\,-\,]$
C_u	Coefficient of uniformity	$[\,-\,]$
D	Diameter after load application	$[\,m\,]$
D_i	Diameter before load application	$[\,m\,]$
D_0	Mould diameter	$[\,m\,]$
d_0	Puck initial diameter	$[\,m\,]$
d_f	Puck final diameter	$[\,m\,]$
d_i^t	Puck intermediate top diameter	$[\,m\,]$
d_i^b	Puck intermediate bottom diameter	$[\,m\,]$
F	Faraday's constant	$[\,C \cdot mol^{-1}\,]$
g	Gravitational constant	$[\,m \cdot s^{-2}\,]$
H	Height after load application	$[\,m\,]$
H_i	Height before load application	$[\,m\,]$
H_0	Mould height	$[\,m\,]$
h	Height	$[\,m\,]$
h_0	Initial puck height	$[\,m\,]$
h_f	Final puck height	$[\,m\,]$
I	Electric current intensity	$[\,A\,]$
I_p	Potline current intensity	$[\,kA\,]$

Symbol	Definition	Unit
j	Electric current density	$[\ A \cdot m^{-2}\ ]$
L	Length	$[\ m\ ]$
$L_{i,\ (i=1,2,3,4)}$	Lengths in the electrical test	$[\ m\ ]$
L_g	Length in the granular material	$[\ m\ ]$
M	Molar mass of Al	$[\ kg \cdot mol^{-1}\ ]$
m	Mass	$[\ kg\ ]$
m_{aa}	Mass of anode with ACM on it	$[\ kg\ ]$
P	Power	$[\ W\ ]$
P_0	Power with puck initial geometry	$[\ W\ ]$
P_f	Power with puck final geometry	$[\ W\ ]$
p	Pressure	$[\ Pa\ ]$
p_0	Pressure on initial puck geometry	$[\ Pa\ ]$
p_f	Pressure on final puck geometry	$[\ Pa\ ]$
R	Electrical resistance	$[\ \Omega\ ]$
r	Sample shape ratio	$[\ -\ ]$
R_c	Electrical contact resistance	$[\ \Omega\ ]$
S	Surface area	$[\ m^2\ ]$
S_c	Common contact surface area	$[\ m^2\ ]$
S_0	Surface area of initial puck	$[\ m^2\ ]$
S_f	Surface area of final puck	$[\ m^2\ ]$
T	Temperature	$[\ °C\ ]$
ΔT	Superheat	$[\ °C\ ]$
T_1	Temperature at reference point 1	$[\ °C\ ]$
T_2	Temperature at reference point 2	$[\ °C\ ]$
T_g	Granular temperature	$[\ °C\ ]$

Symbol	Definition	Unit
T_{cs}	Temperature at contact surface	$[\,°C\,]$
t	Time	$[\,s\,]$
V	Electrical potential	$[\,V\,]$
$V_{i,\ (i=1.2,3,4)}$	Voltage drops in electrical test	$[V]$
V_c	Contact voltage drop	$[\,V\,]$
V_g	Granular voltage drop	$[\,V\,]$
V_{cell}	Cell voltage	$[\,V\,]$
$V_{cell-cell}$	Cell to cell voltage	$[\,V\,]$
V_{up}	Voltage at upper interface	$[\,V\,]$
V_{down}	Voltage at lower interface	$[\,V\,]$
$V_{initial}$	Initial puck volume	$[\,m^3\,]$
$V_{intermediate}$	Intermediate puck volume	$[\,m^3\,]$
W_i	Weightage for KPI	$[-]$
Z	Electrochemical equivalent of Al	$[\,kg \cdot C^{-1}\ \,]$
z	Valency of Al	$[-]$

Greek Symbol	Definition	Unit
α	Intermediate diametral ratio	$[-]$
α_T	Temperature coefficient of electrical resistivity	$[\,°C^{-1}\,]$
β	Strain ratio	$[-]$
ε	Normal strain	$[-]$
ε_a	Axial strain	$[-]$
ε_d	Diametral strain	$[-]$
ϕ	Angle of internal friction	$[\,°\,]$
θ_r	Angle of repose	$[\,°\,]$
θ_r^{eff}	Effective angle of repose	$[\,°\,]$

Greek Symbol	Definition	Unit
ν	Poisson's ratio	$[-]$
η_c	Current efficiency	$[-]$
σ	Normal stress	$[Pa]$
σ_f	Critical normal stress	$[Pa]$
ρ	Electrical resistivity	$[\Omega \cdot m]$
$\bar{\rho}$	Equivalent electrical resistivity	$[\Omega \cdot m]$
ρ_1	Electrical resistivity at T_1	$[\Omega \cdot m]$
ρ_2	Electrical resistivity at T_2	$[\Omega \cdot m]$
ρ_g	Granular electrical resistivity	$[\Omega \cdot m]$
ρ_{gf}	Granular electrical resistivity-final puck	$[\Omega \cdot m]$
ρ_c^{a-g}	Anode-granular SECR	$[\Omega \cdot m^2]$
ρ_{cf}^{a-g}	Anode-granular SECR-final puck	$[\Omega \cdot m^2]$
ρ_c^{c-g}	Cathode-granular SECR	$[\Omega \cdot m^2]$
ρ_{cf}^{c-g}	Cathode-granular SECR-final puck	$[\Omega \cdot m^2]$
ρ_c	Specific electrical contact resistivity	$[\Omega \cdot m^2]$
τ	Shear stress	$[Pa]$
τ_f	Critical shear stress	$[Pa]$

Parameter Symbol	Definition	Unit
ε_0	Parameter of axial strain, ε_a	$[-]$
A	Parameter of axial strain, ε_a	$[kPa^{-1}]$
e_0, e_1	Calibration parameters of ε_0	$[-]$
a_0	Calibration parameter of A	$[kPa^{-1}]$
a_1	Calibration parameter of A	$[-]$
$e_{00}^*, e_{01}^*, e_{02}^*$	Fine calibration parameters of e_0	$[-]$
$e_{10}^*, e_{11}^*, e_{12}^*$	Fine calibration parameters of e_1	$[-]$

Parameter Symbol	Definition	Unit
$a_{00}^*, a_{01}^*, a_{02}^*$	Fine calibration parameters of a_0	$[\ kPa^{-1}\ ]$
$a_{10}^*, a_{11}^*, a_{12}^*$	Fine calibration parameters of a_1	$[-]$
b_0, b_1	Parameters of β	$[-]$
$b_{00}^*, b_{01}^*, b_{02}^*$	Fine calibration parameters of b_0	$[-]$
$b_{10}^*, b_{11}^*, b_{12}^*$	Fine calibration parameters of b_1	$[-]$
d_0, d_1	Parameters of α	$[-]$
$d_{00}^*, d_{01}^*, d_{02}^*$	Fine calibration parameters of d_0	$[-]$
$d_{10}^*, d_{11}^*, d_{12}^*$	Fine calibration parameters of d_1	$[-]$
C_1	Function of ρ_g	$[\ \Omega \cdot m \cdot kPa^{-1}\ ]$
C_2	Function of ρ_g	$[-]$
A_1	Function of C_1	$[\ \Omega \cdot m \cdot kPa^{-1}\ ]$
B_1	Function of C_1	$[-]$
a_{10}	Calibration parameter of A_1	$[\ \Omega \cdot m \cdot kPa^{-1}\ ]$
a_{11}	Calibration parameter of A_1	$[\ \Omega \cdot m \cdot kPa^{-1} \cdot {}^{\circ}C^{-1}\ ]$
b_{10}, b_{11}	Calibration parameters of B_1	$[-]$
D_2	Function of C_2	$[-]$
E_2	Function of C_2	$[-]$
d_{20}	Calibration parameter of D_2	$[-]$
d_{21}	Calibration parameter of D_2	$[\ {}^{\circ}C^{-1}\ ]$
e_{20}, e_{21}, e_{22}	Calibration parameters of E_2	$[-]$
C_3	Function of ρ_c^{a-g}	$[\ \Omega \cdot m^2 \cdot kPa^{-1}\ ]$
C_4	Function of ρ_c^{a-g}	$[-]$
A_3	Function of C_3	$[\ \Omega \cdot m^2 \cdot kPa^{-1}\ ]$
B_3	Function of C_3	$[-]$
a_{30}	Calibration parameter of A_3	$[\ \Omega \cdot m^2 \cdot\ kPa^{-1}\ ]$
a_{31}	Calibration parameter of A_3	$[\ \Omega \cdot m^2 \cdot kPa^{-1} \cdot {}^{\circ}C^{-1}\ ]$

Parameter Symbol	Definition	Unit
a_{32}	Calibration parameter of A_3	$[\ \Omega \cdot m^2 \cdot kPa^{-1} \cdot {}^{\circ}C^{-2}\ ]$
b_{30}, b_{31}	Calibration parameters of B_3	$[\ -\ ]$
D_4, E_4	Functions of C_4	$[\ -\ ]$
d_{40}	Calibration parameter of D_4	$[\ -\ ]$
d_{41}	Calibration parameter of D_4	$[\ {}^{\circ}C^{-1}\ ]$
e_{40}, e_{41}, e_{42}	Calibration parameters of E_4	$[\ -\ ]$
C_5	Function of ρ_c^{c-g}	$[\ \Omega \cdot m^2 \cdot kPa^{-1}\ ]$
C_6	Function of ρ_c^{c-g}	$[\ -\ ]$
A_5	Function of C_5	$[\ \Omega \cdot m^2 \cdot kPa^{-1}\ ]$
B_5	Function of C_5	$[\ -\ ]$
a_{50}	Calibration parameter of A_5	$[\ \Omega \cdot m^2 \cdot kPa^{-1}\ ]$
a_{51}	Calibration parameter of A_5	$[\ \Omega \cdot m^2 \cdot kPa^{-1} \cdot {}^{\circ}C^{-1}\ ]$
a_{52}	Calibration parameter of A_5	$[\ \Omega \cdot m^2 \cdot kPa^{-1} \cdot {}^{\circ}C^{-2}\ ]$
b_{50}, b_{51}	Calibration parameters of B_5	$[\ -\ ]$
D_6, E_6	Functions of C_6	$[\ -\ ]$
d_{60}	Calibration parameter of D_6	$[\ -\ ]$
d_{61}	Calibration parameter of D_6	$[\ {}^{\circ}C^{-1}\ ]$
e_{60}, e_{61}, e_{62}	Calibration parameters of E_6	$[\ -\ ]$

Instead of being listed alphabetically, all the parameter symbols are presented in the order in which they appear in Chapter 3. Interrelated parameter symbols are also grouped together for ease of reference.

CHAPTER 1

INTRODUCTION

1.1 General Information

Aluminium is the third most abundant element in the Earth's crust, after oxygen and silicon. It is the most abundant metallic element (8%) in the Earth's crust as shown in Figure 1-1. It is usually found as a highly stable complex compound instead of in metallic form. Aluminium does not occur naturally in its pure elemental form and is predominantly found in bauxite ore [1].

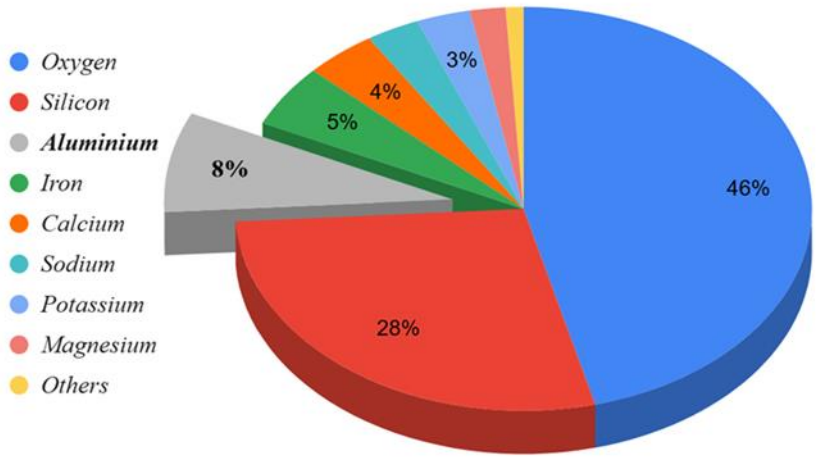

Figure 1-1 : Elemental composition of earth's crust [1]

The end uses of aluminium and its alloys are many. Aluminium's light weight, high strength and good corrosion resistance make it the metal of choice for all commercial and

industrial engineering sectors. Aluminium is also widely used in construction, the electrical and electronics industries, and packaging applications due to its corrosion resistance, high thermal and electrical conductivity, and infinite recyclability [2].

The automotive and transportation industry relies on a variety of aluminium alloys in the manufacture of various components because of their lightness but very strong when alloyed with other metals and durability, which reduce a vehicle's weight and, in turn, fuel consumption and greenhouse gas emissions [2]. In Figure 1-2, the bar graph shows the major global uses of aluminium in 2025.

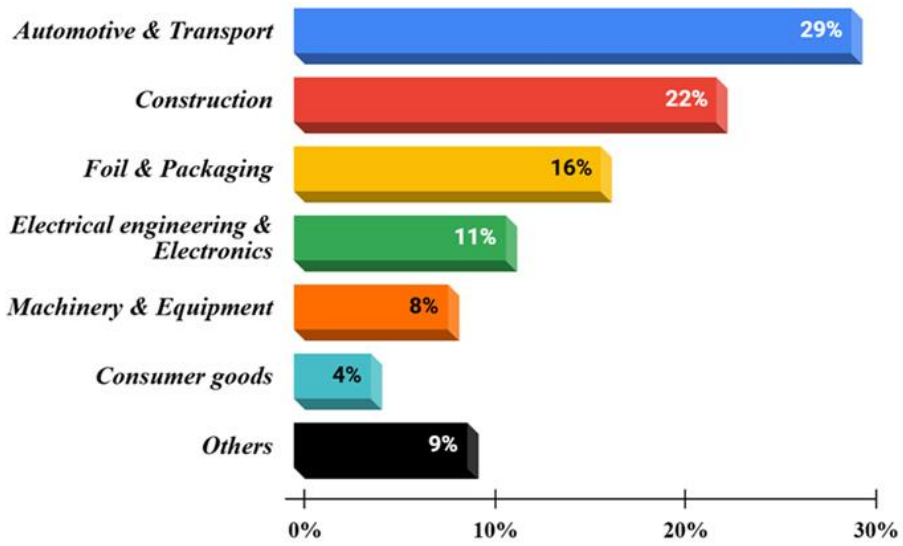

Figure 1-2 : Global usage of aluminium by application in 2025 [3]

The largest use was for automotive and transportation (29%), followed by construction (22%), foil and packaging (16%), electrical engineering and electronics (11%), machinery and equipment (8%), consumer goods (4%) and other applications (9%) [3].

Irrespective of the origin of the aluminium, its end use is growing specially in the last few decades. Now, it is also the second most widely used metal after iron. Due to infinitely recyclability, aluminium is one of the most widely used and recycled metals in the world.

1.2 Aluminium Production

Due to its strong affinity to oxygen, aluminium does not occur in nature in its pure elemental state and is only found in combined forms such as oxides and silicates. Bauxite is the most common mineral mainly under gibbsite, boehmite or diaspore forms. Aluminium cannot be produced by an aqueous electrolytic process because hydrogen is electrochemically much nobler than aluminium. To produce aluminium metal from such a stable compound requires complex technology and large amounts of energy [4].

Aluminium is obtained from two main sources: primary production from mineral ores and secondary production through recycling and remelting of aluminium scrap. It is labelled as 'primary' because it is made from its ore and natural minerals. Secondary aluminium gets its name from its source. It's 'secondary' because it is made from recycled aluminium scrap. This scrap can come from all sorts of aluminium products and profiles, such as aluminium turnings, aluminium sheets, aluminium shreds, aluminium radiators, cast aluminium, extrusions, painted sidings, aluminium dross *etc*. Generally, secondary aluminium has a higher tolerance for alloying elements, such as iron, magnesium, and silicon (which are commonly added in the recycling process). Secondary aluminium

cannot meet global demand because of economic growth, the increase of various extensive usages, and very specific high purity electronic usages. So, primary aluminium production still plays a major role [4].

1.3 Primary Aluminium Production

Commercial production of metallic aluminium became economically viable in 1889 with the electrolytic reduction of aluminium oxide dissolved in molten cryolite at approximately 975 °C, marking the birth of the modern industrial process. Alumina is well known to be largely insoluble in most solvents. However, sodium hexafluoro aluminate, (Na_3AlF_6) naturally occurring in Greenland as the mineral cryolite, was found to possess the special properties required for electrolytic aluminium production [5].

The first stage of aluminium production involves refining the mineral ore into aluminium oxide or alumina , which is carried out in an alumina refinery using the Bayer process, named after the Austrian chemist Karl Josef Bayer, who developed it in 1888. Because the mechanical properties of aluminium are strongly influenced by small amounts of alloying elements and impurities, it is important that smelter grade alumina (SGA) is of high quality. Accordingly, the smelting of high-purity aluminium requires high-purity alumina (Al_2O_3), and carbon (C).

The dominant mineral ore used for alumina production is bauxite, which is formed by the tropical weathering of aluminous rocks. Bauxite typically contains 40–60% of hydrous

alumina phases, mainly gibbsite, $Al(OH)_3$, boehmite, $AlO(OH)$, and diaspore, $AlO(OH)$, along with iron oxides, silica, and smaller amounts of other oxides. Although processes have been developed to extract alumina from clays, anorthosite, alunite, nepheline, leucite, and other minerals, these routes are generally more costly and energy-intensive than the processing of bauxite.

In the second stage, SGA (Al_2O_3) is converted into metallic aluminium (Al) in the process called as the Hall–Héroult process in an aluminium smelter. This electrolytic smelting takes place in an industrial aluminium reduction cell (also referred to as an aluminium electrolysis cell or reduction cell or pot), as shown in Figure 1-3.

Figure 1-3 : Industrial aluminium reduction cell in operation at LRF, Saint-Jean-de-Maurienne, France

To date, this remains the only industrially viable method for primary aluminium production since its invention. Thus, industrial-scale aluminium production involves two independent processes for the transformation of naturally occurring aluminium oxide ores into metallic aluminium [5].

In 2025, approximately 74 million tonnes of primary aluminium are produced globally. Figure 1-4 shows the evolution of primary aluminium production in the world for last 50 years [6].

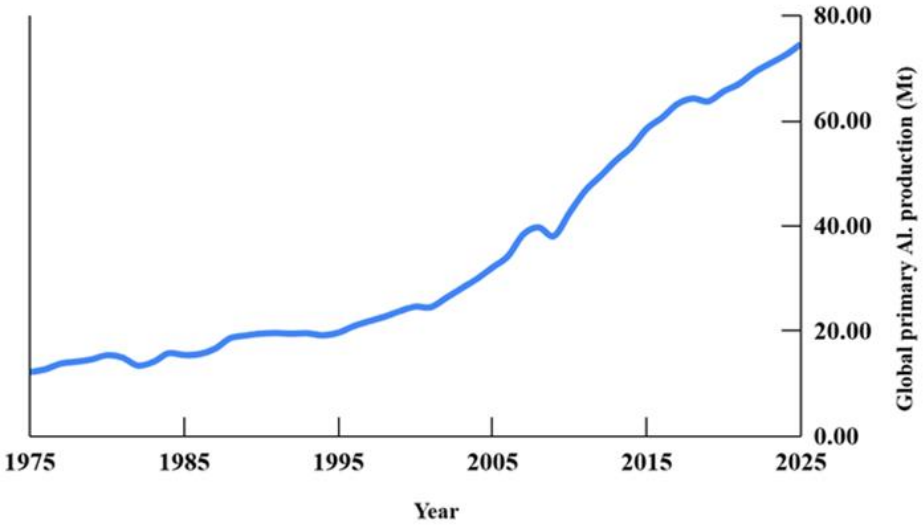

Figure 1-4 : Global primary aluminium production for the last 50 years [6]

It can be observed that the global aluminium production has tripled in the last 25 years and achieved a 25% increase in the last 10 years. Although the primary aluminium production process is energy intensive, the demand of the metal drives the growth in the production rapidly and in coming years it will continue to grow by 6.2% CAGR globally

[7]. Approximately 75% of all aluminium ever produced is now under active use, as per the estimates provided by the Aluminium Association.

It can also be seen in Figure 1-5 that in 2025, Asia contributes about the major share – 77% of global primary aluminium production followed by Europe (10%) and North America (6%). Country wise, China (59%) leads the primary aluminium production followed by India (6%), Russia (5%) and Canada (4%) as shown in Figure 1-6.

Figure 1-5 : Primary aluminium production by continent [6]

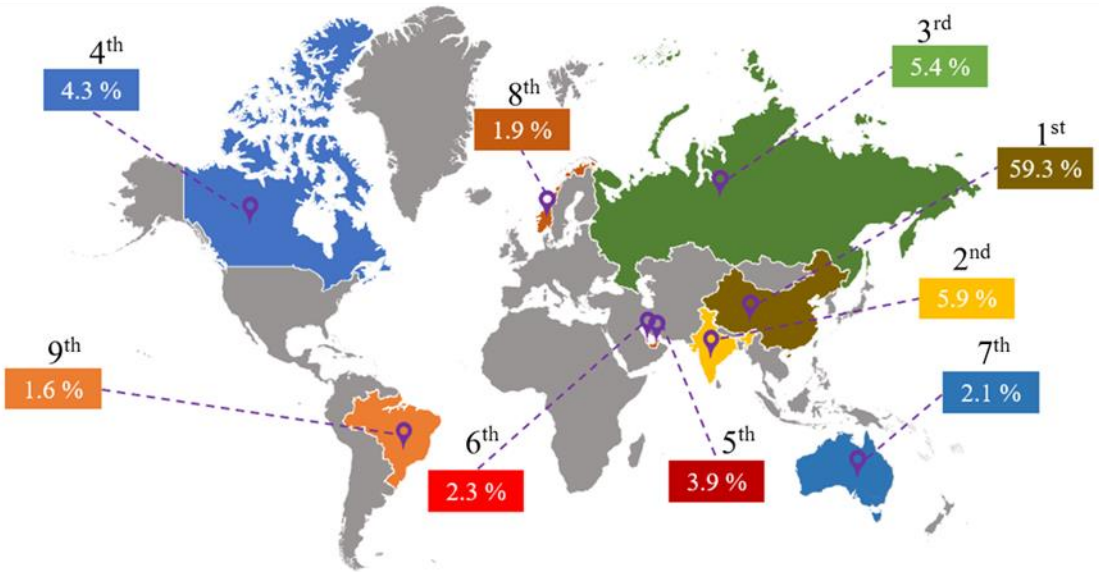

Figure 1-6 : Primary aluminium producing countries in 2025 (>1Mt) [6]

Alternative Processes for Aluminium Production

Alternative processes for primary aluminium productions are carbothermic reduction of alumina and aluminous ores, and aluminium chloride electrolysis. The carbothermic reduction process is industrially not viable due to various factors, including energy costs, environmental considerations, and the desired purity of the aluminium product. Alcoa's chloride cells have produced aluminium at less than 9.5 kWh/kg Al, and well above the 13000 kg Al/day. However, their industrial scale pilot plant is no longer in operation, mainly due to problems involved in producing and handling pure, water-free aluminium chloride required for electrolysis and the presence of polychlorinated hydrocarbons which caused unacceptable pollution problems [8].

Norsk Hydro is working simultaneously on HalZero project and carbon capture & storage project. HalZero is based on converting alumina to aluminium chloride prior to electrolysis and chlorine and carbon are kept in a closed loop, thus eliminating emission of CO_2 and emitting O_2 instead. If successful, HalZero technology will fully decarbonise the smelting of aluminium by eliminating emissions from both electrolysis and anode baking [9].

Since 2018, in the effort to decarbonise the production process, Alcoa & Rio Tinto jointly working on a potential alternative process using inert anode technology called as ELYSIS. In mid 2024, Rio Tinto has decided to build 10 demonstration cells at 100 kA in Arvida site in the Saguenay-Lac-Saint-Jean region of Quebec. In November 2025, ELYSIS proudly announced the successful commissioning of its inert anode cell designed for 450 kA, installed at Rio Tinto's aluminium smelter in Alma, Quebec, highlighting a key step in the transition to large-scale, low-carbon aluminium production. In short, if they succeed to industrialize the joint effort, ELYSIS technology will make it possible to replace greenhouse gas (GHG) emissions with oxygen, reduce the intensity of capital investments, improve health and safety at work and reduce operating costs, while increasing the productivity of aluminium smelters [10].

On the other hand, RUSAL is developing an inert anode technology. Currently, the Krasnoyarsk aluminium smelter operates a pilot section of cells with inert anodes of a new generation, which allows reducing the carbon footprint to a record level – less than 0.01 tonnes in CO_2 equivalent per ton of aluminium (both direct and indirect emissions).

To test the technology, RUSAL has started its industrial production of inert anodes. At present, the technology is in the process of being tested and improved in aluminium production at industrial amperage [11].

1.4 The Hall-Héroult Process

The Hall-Héroult process (named after its inventors) is the only method for the industrial aluminium production till now, although a lot of attempts are being made in the past and recently to replace the process fundamental to decarbonise the process and to make more environmental-friendly. The present method for industrial production of aluminium was discovered nearly simultaneously and completely independently in 1886 by Paul-Louis-Toussaint Héroult in France and Charles Martin Hall in the United States of America. Surprisingly, the electrolysis of cryolite-alumina melts was patented by both, which differed only in detail. These patents coincided with developments in the generation of electric power, which made commercial processing technically viable. The process also received an added boost at about the same time by the development of the Bayer process for extracting alumina from bauxite [8].

The melting point of alumina is close to 2070 °C, which is in general too high for commercial production. To produce aluminium more efficiently, *i.e.* at a lower operating temperature, Hall and Héroult found cryolite (Na_3AlF_6) as a chemical compound that acted as a solvent for alumina. In the Hall-Héroult process, the alumina is dissolved in the molten cryolite (having a melting point of 1010 °C), which reduces the temperature

to below 1000 °C. However, by increasing the fluoride contents, it is possible to operate the process in the 950 to 965 °C range industrially.

In the electrolytic cell, the alumina is dissolved in a bath, which is typically composed of cryolite (Na_3AlF_6), and the anode is made of pure carbon (C). One or several carbon anodes are dipped into the electrolyte, and oxygen from alumina is discharged electrolytically into the anodes as an intermediate product. However, the oxygen immediately reacts with the carbon anode and thus gradually consumes it by the formation of different gaseous carbon products. The aluminium is formed at the metal/electrolyte interface, which acts as a cathode [5]. This is the fundamental concept of aluminium production using electricity is to reduce alumina (Al_2O_3) to aluminium (Al).

During the electrolysis process, the aluminium ions are reduced to aluminium metal and collected at the bottom of the cell. The oxygen is discharged at the carbon anode, where it reacts with carbon to form gaseous carbon oxides. This electrowinning production of pure aluminium occurs with emission of various cell gases like CO_2, CO, SO_2, HF, CF_4, C_2F_6, $NaAlF_4$ *etc.* This process produces almost 99.9% pure aluminium. The main electrochemical reaction occurring at around 960 °C in the cell is represented by the equations with the aluminium being deposited at the bottom of the cell [5][8].

$$2\ Al_2O_3\ (diss) + 3C\ (s) \rightarrow 4\ Al\ (l) + 3\ CO_2(g) \qquad \textbf{(1-1)}$$

$$Al_2O_3\ (diss) + 3C\ (s) \rightarrow 2\ Al\ (l) + 3\ CO(g) \qquad \textbf{(1-2)}$$

Both reactions occur parallelly in the cell with Equation (1-1) being dominant. However, some of the metal is dissolved in the electrolyte and transported so that it can be re-oxidised by the CO_2 evolved at the anode according to the following reaction:

$$2Al\ (diss) + 3\ CO_2\ (g) \rightarrow\ Al_2O_3(diss) + 3\ CO(g) \qquad \textbf{(1-3)}$$

This reaction is known as recombination reaction. Not only does this reaction led to a decrease in the metal production (current efficiency), but it also accounts for much of the carbon monoxide in the anode gas and leads to an increased overall carbon consumption per unit metal produced. This is also called as "Back reaction".

Theoretically, the amount of aluminium produced in an electrolysis cell depends on the potline operating current intensity and follows Faraday's laws of electrolysis. The theoretical amount of aluminium (kg) produced in a cell is given by [8]:

$$\text{Faraday's Theoretical Production } = Z \cdot I \cdot t \qquad \textbf{(1-4)}$$

where, I (A) is the current intensity passed through the cell, t (s) is the time and Z (kg/C) is the electrochemical equivalent (ECE) which is the theoretical mass of aluminium deposited per coulomb of charge passed and is given by the following equation.

$$Z = \frac{M}{z\,F} = 9.320 \times 10^{-8} \qquad \textbf{(1-5)}$$

where, $M = 0.02698$ kg/mol is the molar mass of aluminium, $z = 3$ is the valency or number of electrons involved in the electrode reaction and $F = 96485.33$ C/mol is the Faraday's constant. Substituting the values of Z from Equation (1-5) into Equation (1-4), Faraday's theoretical production (kg) becomes:

$$\text{Faraday's Theoretical Production} = 9.320 \times 10^{-8} \cdot I \cdot t \qquad \textbf{(1-6)}$$

But practically, the cell produces lesser metal than the Faraday's theoretical production. There are some losses of metal due to various reasons including the back reaction. Hence, the amount of aluminium produced in the cell per day depends on its fractional current efficiency (CE or η_c) and is given by

$$\begin{gathered}\text{Electrolysis Cell Production} \\ = (\text{Faraday's Theoretical Production}) \cdot (\eta_c)\end{gathered} \qquad \textbf{(1-7)}$$

Substituting the values of Faraday's theoretical production from Equation (1-6) into Equation (1-7), we get the electrolysis cell production (kg) as:

$$\text{Electrolysis Cell Production} = 9.320 \times 10^{-8} \cdot I \cdot t \cdot \eta_c \qquad \textbf{(1-8)}$$

Hence, electrolysis cell production depends on the potline current intensity and the fractional current efficiency of the operating reduction cell.

Aluminium reduction cells are classified based on the anode type into Söderberg and prebake. The Söderberg technology (named after the Swedish-Norwegian engineer Carl Wilhelm Söderberg) uses a single continuous anode that gets baked *in situ* from the added anode paste, whereas the prebake technology employs multiple anodes in each cell, which are pre-baked in a separate furnace, as illustrated in Figure 1-7 [8]. There are two types of Söderberg cells: Vertical Stud Söderberg (VSS) cell and Horizontal Stud Söderberg (HSS) cell.

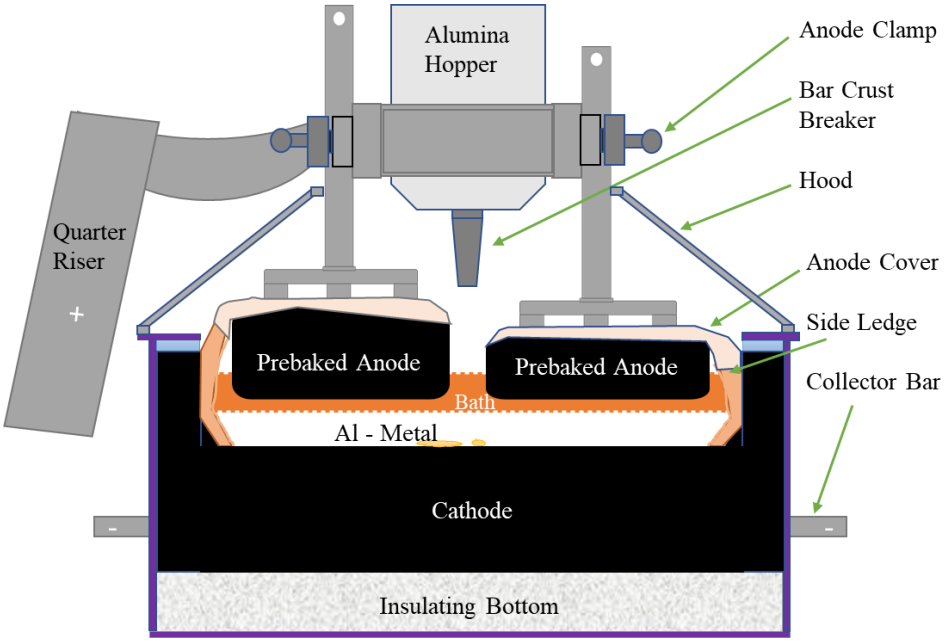

Figure 1-7 : Schematic diagram of a prebake reduction cell

Figure 1-8 and Figure 1-9 show the general structure of a VSS and an HSS reduction cell, respectively. VSS cells are more common than HSS cells, as they are less labor-intensive and cause fewer operational disturbances. Compared with prebake technology, Söderberg cells are less efficient, have higher production costs, are more difficult to automate, and pose the greatest environmental and health challenges. Health studies from the mid-1970s demonstrated a clear link between exposure to Söderberg tar fumes and the incidence of various types of cancer, prompting companies to implement replacement programs. As a result, today only a few Söderberg smelters remain, mainly in Russia, with significant modifications to their gas collection systems [12][13].

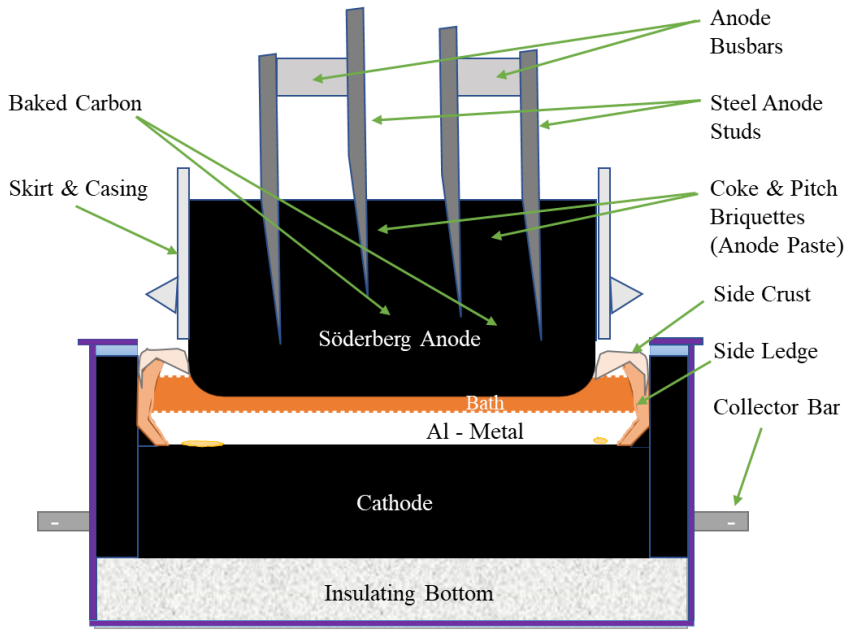

Figure 1-8 : Schematic diagram of a vertical stud Söderberg (VSS) cell

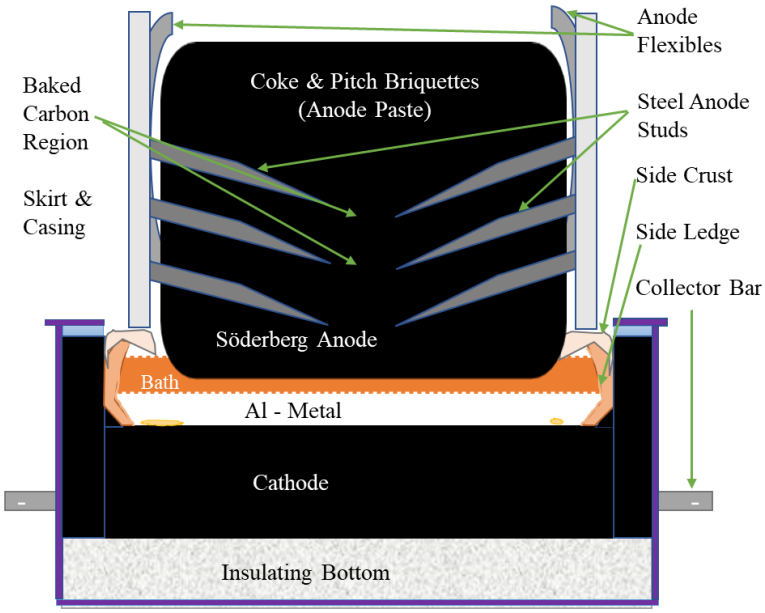

Figure 1-9 : Schematic diagram of a horizontal stud Söderberg (HSS) cell

1.4.1 Modern Aluminium Reduction Cells

The first commercial aluminium reduction cells carried about 600 A [5]. Over the last 140 years, the scale has increased to the extent that SY600 and NEUI600 reduction cells already have operated at 600 kA as per the literature by 2015 [14][15]. SY660 reduction cells have operated at 660 kA [16]. Northeastern University Engineering & Research Institute (NEUI) completed the engineering design of an 800 kA potline in 2017 [17]. A continuing series of modifications have been incorporated in the cell designs, and the appearance of the cells has changed dramatically. However, these changes have been made to incorporate technological and design advances and have not involved any change in the fundamental production process. Although the original concept of the Hall-Héroult

process has not changed, improvements have been made in a continuing effort to lower production costs and the harmful effects on environment in both equipment and materials for today's industrial production. Investors prefer aluminium smelters with higher amperage reduction cell technology because of its significant effect on decreasing investment per produced tonne of aluminium.

The aluminium reduction cells are the nerve centres of the smelter plant. Approximately, 250 to 450 reduction cells are placed and connected in series, which is called potline or potrooms. The process requires direct current (DC), which ranges from 300 to 600 kA, depending on the cell technology used [15]. Figure 1-10 shows the state-of-the-art AP60 potroom of Arvida Aluminium Smelter at the Jonquière Complex, Saguenay, Quebec, Canada.

A modern aluminium reduction cell with prebaked anodes consists of a strong rectangular steel shell lined with thermally insulating refractory materials to maintain the required thermal balance. Inside the shell, prebaked carbon cathode blocks equipped with embedded steel and partial copper collector bars form the current-carrying base on which the molten aluminium rests during electrolysis. Carbon sidewalls, supported by layers of refractory insulation, help control heat flow and maintain a stable side-ledge profile. The entire cell is enclosed by a hooding system connected to a gas exhaust and scrubbing network that captures and treats fluoride- and sulphur-bearing fumes, ensuring efficient operation, long lining life, and compliance with modern environmental standards.

Figure 1-10 : The state-of-the-art AP60 potroom of Arvida Aluminium Smelter

The general schematic structure of the modern aluminium reduction cell is given in Figure 1-11. From the side risers, direct electric current passes through the anode assemblies, electrolyte bath, molten aluminium and cathode. Finally, the current is directed out of the cell through the collector bars to the busbar network which takes the current to the side risers of the next reduction cell [26].

In the following subsection, the major components of a modern aluminium reduction cell— the anode assembly, the cathode assembly, the superstructure, the electrolyte bath, and smelter grade alumina are presented and discussed with emphasis on their features and functional roles in achieving stable and efficient cell operation. In the end, the production and the power consumption of modern aluminium reduction cells are discussed.

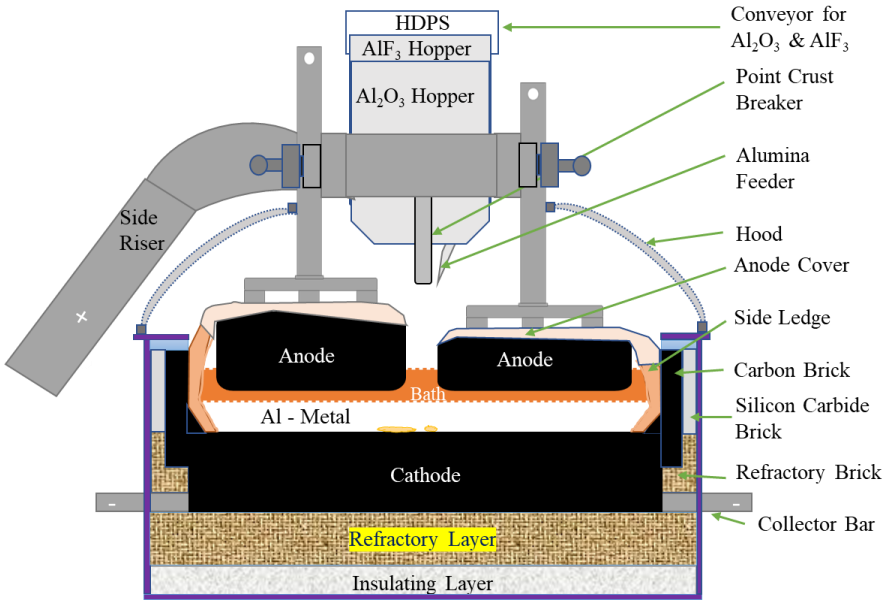

Figure 1-11 : Schematic diagram of a modern aluminium reduction cell

The Anode Assembly

The anodes are considered as one of the raw materials for the Hall-Héroult cells thus consumable in the electrolysis process. Prebaked anodes are used for modern electrolysis cells. Prebaked anodes are made from a mixture of petroleum coke aggregate and coal tar pitch binder, compacted and moulded into blocks and baked in a separate anode baking furnace at approximately 1200 °C for several days. A bimetallic joint connects the aluminium rod with the yoke having several iron studs. These studs are then casted into the grooves on top of the anode block to support the anode mechanically and conduct the electric current to the anode when it is used in reduction cells [8]. Figure 1-12 shows an anode assembly having two anode blocks. Anode assembly with one anode block is also common industrially. Anode slots are typical feature of modern aluminium reduction cells. They help to mitigate the thermal shock providing the structural integrity to the

carbon block. They also efficiently evacuate the underneath bubbles formed during the electrolysis helping to lower the cell voltage which saves energy [18].

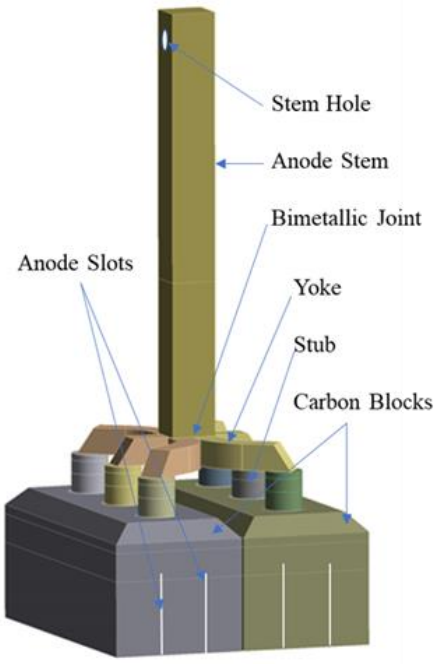

Figure 1-12 : An anode assembly

Prebaked anodes have the advantage that they give better quality product and significantly reduce anode carbon consumption as compared to Söderberg anodes. Compared with Söderberg anodes, prebaked anodes enable substantially lower greenhouse gas emissions in primary aluminium production due to reduced anode consumption, improved energy efficiency, and lower perfluorocarbon emissions associated with fewer anode effects. In modern reduction cells, anode assemblies are changed in regular intervals as they get consumed in the electrolysis process.

The Cathode Assembly

The cathode is the most expensive part of an aluminium reduction cell. The cathode assembly is located at the bottom of the reduction cell. It is bottom-lined with carbon cathode blocks (anthracite or semi/fully graphitised or semi/ fully graphitic) on top of the insulating and refractory layer and side-lined with carbon and silicon carbide bricks in a shallow steel shell/tank (of 1.0–1.2 m deep). Figure 1-13 shows a quarter of a cathode assembly. The cathode blocks are sealed together by the ramming paste. The cathode assembly is placed on the cradles. The collector bars (made up of steel or steel with partial copper are already casted into the grooves of the cathode blocks) are joined with the cathode busbar system to carry the DC.

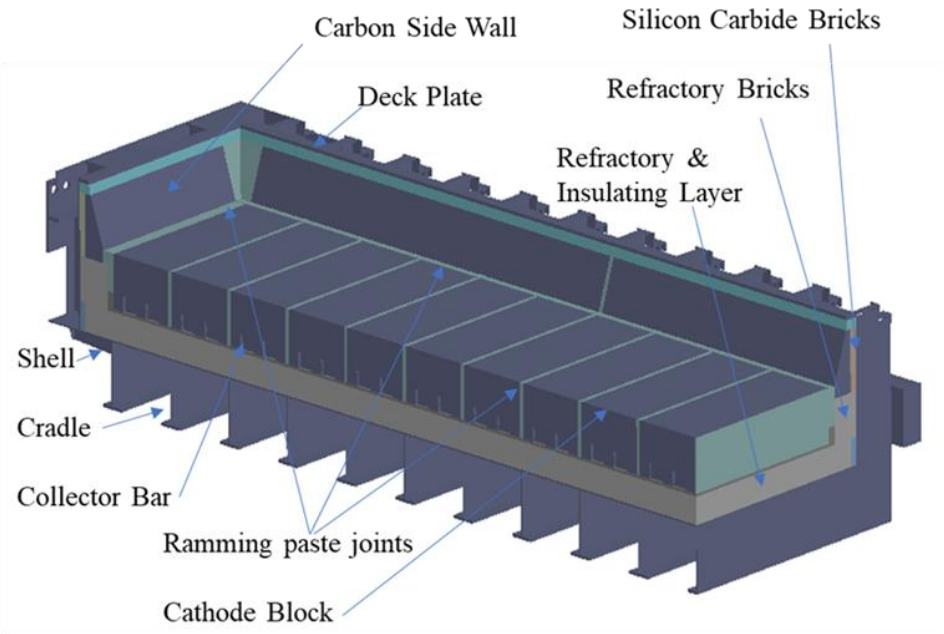

Figure 1-13 : A quarter of a cathode assembly

Graphitised and graphitic cathode blocks and partial copper collector bars are salient features of the modern reduction cells. They have higher electrical conductivity as compared to the anthracitic cathode block which helps to save energy [26][27].

It has become usual in the industry to describe the whole container of molten aluminium and electrolyte as the cathode, although the electrolytic cathode in Hall-Héroult cells is scientifically the top surface of the molten metal pool. The bottom carbon lining carries the electric current from the molten metal, on which aluminium is deposited, and therefore, this serves as a cathode in the electrolytic process [19].

The Superstructure

A typical feature of the modern aluminium reduction cells is its complex superstructure design. It facilitates the raw material storage, their transportation for the process requirements, and sophisticated gas collection for further treatment. It is mainly a huge steel structure of similar length of the cathode of the respective reduction cell. It is positioned on the cathode assembly with electrical isolation. It is connected to the side risers to pass direct current and to the duct that collects and sends fumes to the Gas Treatment Centre/Fume Treatment Plant (GTC/FTP) as well [20].

It has an aluminium busbar where all the anodes are hanged, and it carries the DC electricity for the process. It contains several hoppers for alumina, aluminium fluoride and crushed bath, several crust breakers and (integrated) feeders. The raw materials like alumina and aluminium fluoride are replenished in their respective hoppers by means of

hyper dense phase system (HDPS) or dense phase conveying system (DPCS) are mounted and attached to the superstructure, whereas crushed bath is loaded into the hopper by means of an over head crane or a special vehicle [8].

The superstructure provides the place to install several hoods (or side covers). So, the top side of the cell is closed by a hooding system to prevent the cell waste gases to escape and facilitate the gas collection. In-built duct system of the superstructure collects the cell gases and sends to the GTC/FTP for further treatment where fluoride and sulphur are recovered efficiently from the waste gases. The scrubber mixes the waste gases with alumina to adsorb *i.e.*, remove the gaseous and particulate fluoride components before the waste gas is exhausted to the atmosphere. This process of removing fluoride components is called dry scrubbing, whereas the other scrubbing process in which the cell gas is treated with water to remove sulphur components is called wet scrubbing [8].

The Electrolyte Bath

The electrolyte bath industrially called as bath (which mainly contains cryolite) is used because of its unique and unmatched capacity as a solvent for alumina. The alumina is dissolved in the bath, which is typically composed of cryolite (Na_3AlF_6), with a small percentage of other additives to enhance its properties. The composition of the electrolyte can be expressed as cryolite ratio (CR) or bath ratio (BR) or excess AlF_3% (widely used currently). The bath composition is an important factor of the cell operation. Most of the changes in bath composition have aimed at better cell operation . Functions of the electrolyte bath can be summarised as [8]:

1. Solvent for alumina (dissolved alumina into ions).
2. Physically separate the electrodes (between anode and cathode).
3. Provide an electrical path between electrodes and generation of heat.

In addition to cryolite as the main component, the bath in modern reduction cells typically contains aluminium fluoride (AlF_3), calcium fluoride (CaF_2) and the operating alumina content (Al_2O_3). In some cases, lithium fluoride, magnesium fluoride and potassium fluoride are added to the bath composition. Table 1-1 shows the industrial bath composition for modern reduction cells. High AlF_3 content in the electrolyte bath is the typical feature in the modern reduction cells [21].

Table 1-1 : Composition of the electrolyte bath [21]

Compound	Formula	Weight %	Comments
Cryolite	Na_3AlF_6	80	
Aluminium fluoride	AlF_3	10 - 12	
Calcium fluoride	CaF_2	5 - 6	
Alumina	Al_2O_3	2 – 3.5	
Lithium fluoride *	LiF	1 - 2	**In case of presence of* LiF, MgF_2, KF the AlF_3 *usually kept around 6-7%*
Magnesium fluoride *	MgF_2	2 - 3	
Potassium fluoride *	KF	1 - 2	

Modern cells contain around 6 to 8 tonnes of liquid electrolyte bath. The bath temperature during normal cell operation is typically in the range from 950 to 965 °C. The bath height in the normal operating cells is usually kept close to 18 to 20 cm. Its composition and temperature are carefully controlled to maintain optimal solubility, conductivity, and ledge profiles (side and bottom). The bath is not consumed as such during electrolysis, but some losses occur, mainly by vaporisation as a species of $NaAlF_4$ gases and penetration into the cathode lining. Cell start-up needs a lot of baths initially, even during early life period a lot of baths are added. Once the cell is started and is operated normally it becomes net producer of the bath [8][21].

Smelter Grade Alumina

In the aluminium electrolysis process, the smelter grade alumina—a free-flowing granular white material (as shown in Figure 1-14) is the primary raw material for metal production. Modern cell superstructures are equipped with 4 to 7 pneumatic point feeders associated with their hoppers to store the alumina. The secondary alumina from GTC is transported to these hoppers in the superstructure by HDPS. Then the point feeders are used to feed small dumps of 1-2 kg of alumina with a particular feeding interval. Secondary alumina which is enriched with fluoride is generally fed to most of the pots unless a plant has a high purity potline where smelter grade alumina is preferred to reduce metallic impurities coming from pot gases flowing in the gas treatment systems. Main functions of alumina are [8]:

1. Primary raw material for Al production.

2. Thermal insulator on the top of the anodes and crust.

3. Capture the gaseous fluoride emissions from the cells.

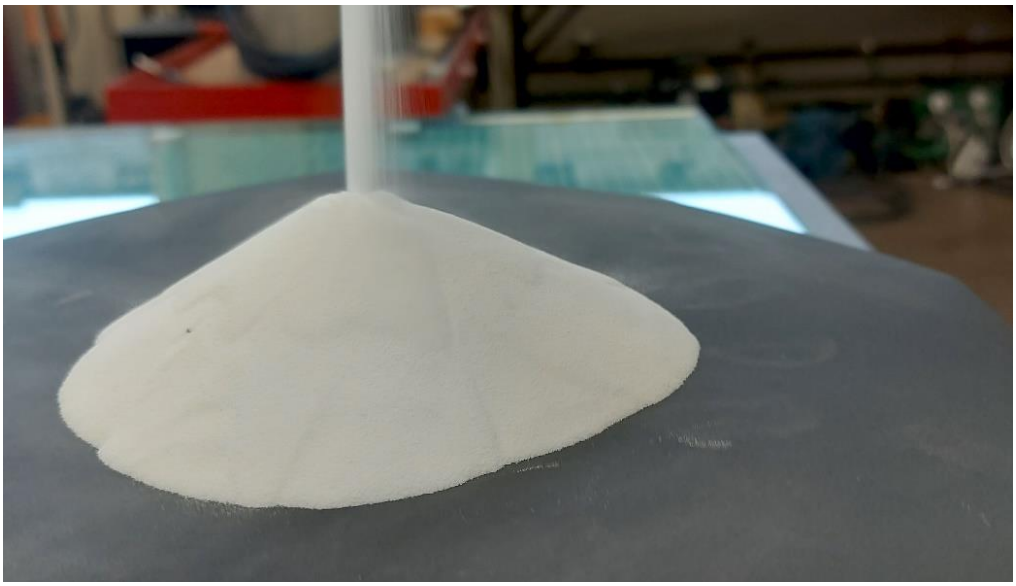

Figure 1-14 : Smelter grade alumina (SGA)

In prebake technology, the anode covering material (ACM) consists of crushed bath and alumina, protects anodes from air oxidation. Alumina on the crust also adsorbs HF, an important pollutant. Therefore, the quality of alumina added to the electrolyte and the quantity of alumina in ACM are of great importance for cell operation . The specifications imposed by a smelter includes chemical purity, bulk and real/pycnometric densities, BET (Brunauer-Emmett-Teller) surface area, loss on ignition (LoI), particle size distribution (PSD), alpha alumina ($\alpha - Al_2O_3$) and attrition index. The chemical purity is one of the specifications of great importance to the quality of the aluminium and the performance of the cell [8].

Production and Power Consumption of an Aluminium Reduction Cell

The molten aluminium produced is deposited directly on the cathode making a metal pool. The real amount of aluminium produced in an aluminium reduction cell depends on the potline operating current, I_p (kA) and fractional current efficiency (η_c) [8]. From the Equation (1-8), the real amount of aluminium (kg) produced in a cell per day is given by:

$$\text{Daily Cell Production} = 8.053 \cdot I_p \cdot \eta_c \qquad \textbf{(1-9)}$$

The fractional current efficiency of modern reduction cells stays around 0.935 to 0.950. Hence, a modern reduction cell operating at 400 kA with 0.945 current efficiency produces 3044 kg Al/day.

The power consumption of modern aluminium reduction cells is primarily determined by the cell voltage (V_{cell}) and operating current (I_p). If $V_{cell-cell}$ (V) is the cell-to-cell voltage (voltage drop measured for one complete reduction cell which includes the cell voltage and external busbar drops), then the power consumption (kW) can be calculated as follows:

$$\text{Cell Power Consumption} = V_{cell-cell} \cdot I_p \qquad \textbf{(1-10)}$$

The cell-to-cell voltage remains around 3.900 to 4.200 V for modern reduction cells. Hence, a modern reduction cell operating at 400 kA with 4.150 V as cell-to-cell voltage

needs 1660 kW or 1.66 MW of power. Therefore, operating a reduction cell is a highly power-consuming and energy-intensive process.

1.5 Statement of the Problem

The start-up of a prebake reduction cell is a lengthy procedure in which it goes through different phases before it gets operated normally for the efficient production of aluminium. The cathodes are often preheated in the start-up particularly in the preheating phase before pouring liquid electrolyte bath onto it. In case of dry start-up, the liquid electrolyte bath is generated in the cell from the crushed solid electrolyte bath (or solid cryolite) during the preheating phase. Currently, reduction cells are preheated electrically by means of passing direct electric current by using the resistive granular blends.

In the electrical preheating of the aluminium reduction cell, a layer of granular coke and/or graphite blend (referred to as resistive bed or lying-bed) is placed on the cathode by using the special template mould. All the anodes are placed on top of the lying-bed. Then anodes are connected to the anode beam of the cell using flexibles and the cell is covered to insulate thermally for the preheating. After the energisation of the cell, during the preheating phase, the anodic current distribution and the cathode surface temperature at prefixed places on the cathode are monitored at a certain regular interval [22].

Often, these data show an important non-uniformity along the cathode surface. It is observed that the cathode surface temperature in the central zone is much higher than the temperature in the peripheral zone (as shown in Figure 1-15) resulting in a higher

percentage of unbaked ramming paste at the end of the preheating phase. New cells with low cathode surface temperatures at the ends are usually unstable and more difficult to operate just after the start-up than more uniformly preheated cells [23].

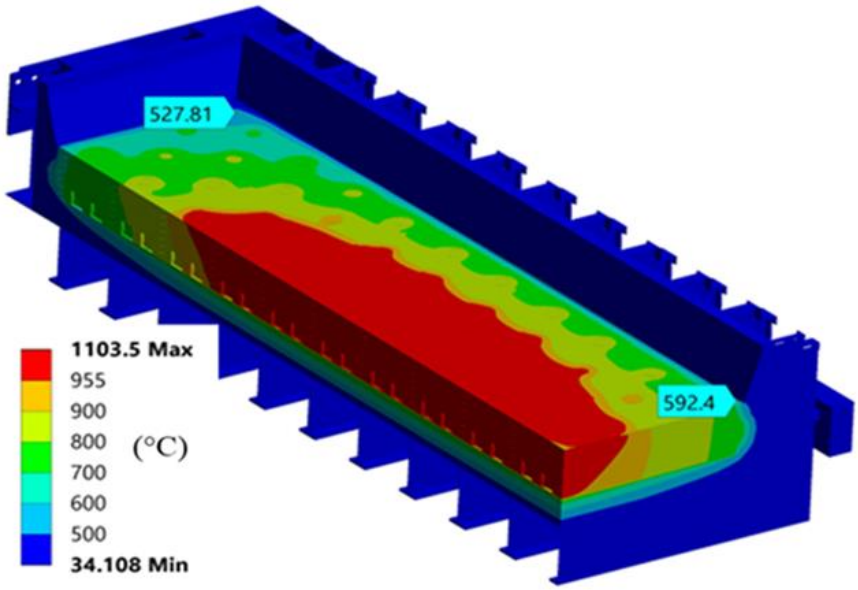

Figure 1-15 : Cathode temperature distribution after preheating

Similar irregularity is also observed for anodic current distribution. Typically, anodes, placed at four corners draw lower currents as compared to the anodes in the middle of the cell [22]. These irregular situations/observed events in the preheated cathodes lead to some challenges in newly started cells which will be discussed in the following sub-section.

Specific Challenges Encountered in Newly Started Reduction Cells

Some of the problems encountered in newly started reduction cells are listed below [22]:

1. Frozen bath on the peripheral cathode surface due to lower cathode surface temperature.

2. Higher instability in newly started cells in early life operational period.

3. Hard and thick deposition of sludge/muck especially on the cathode corners for a long period of time. It gets prominent in case of low-energy-operating cells.

4. Premature cathode failure which is the worst-case scenario.

Importance of the Cathode Preheating

To reduce the cost of primary aluminium production it is necessary to continuously consider improvements in cathode design, lining technique and cell operation as well as introducing new or improved lining materials. The contribution of several factors to cathode life is arguable and differs from plant to plant. According to Hale a likely scenario is shown in Figure 1-16 [24]. It is widely accepted that start-up and early operation have a strong influence on the performance and life of the Hall-Héroult cells. The cathode itself contributes about 50% to cathode life while operational procedures and cell start-up contribute the other 50%. In tandem, preheating and start-up contributes 25% towards cathode life.

The cathode is the most expensive part of the industrial electrolysis cells. For a 400 kA modern cell the cathode replacement costs approximately 600,000 to 750,000 CAD depending on the technology, the quality of materials used and the location of the smelter [25][26]. Compared to other potential improvements a smelter can make in operation; improved cathode life ranks high for reducing production costs. A significant savings is possible with extended cathode life.

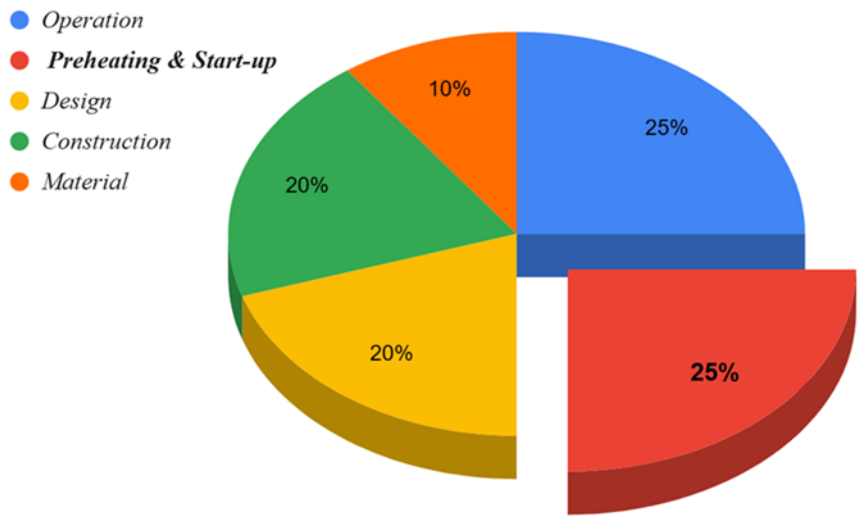

Figure 1-16 : Cathode life dependency [27]

Maximum cathode life cannot be expected from a well-designed cathode built with excellent workmanship if it becomes subject to sloppy operation and maintenance. Neither will a poorly constructed and built cathode achieve optimum life even if preheating, start-up, and operation are the best that can be given [27]. In that respect, it is better to view each contribution as a link in a chain, *i.e.* when one link fails the whole cathode fails (Figure 1-17).

Last but not the least are the savings in spent pot linings (SPL) disposal costs. SPL contains high levels of cyanides, fluorides, sodium, and reactive compounds (*e.g.*, metallic sodium, aluminium carbides, refractory bricks and insulation contaminated mainly with fluoride). It emits toxic gases if exposed to moisture. Hence, increase in cell cathode life can reduce the spent pot lining disposal cost. This will minimise the impact on environment [27].

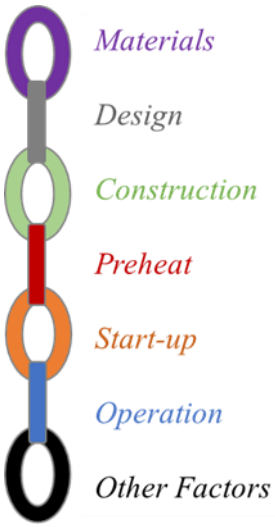

Figure 1-17 : Factors affecting cathode life [27]

The preheating phase has a significant impact on the early cell operation and cell life since the cathode goes through significant thermal, electrical, mechanical and chemical changes during this phase. It must therefore be carried out meticulously to minimise the impact of these changes on the start-up as well as on the life of the electrolysis cell. Hence, a preheating which minimises the impacts of these changes on the cathode life is crucial for the smelter's productivity.

1.6 Objectives

The main objective of this project is to optimise the lying-bed (used in the aluminium reduction cells for electrical preheating) to enhance the cathode preheating process to improve the cell performance. More specifically, the results of this project should make it possible to have:

1. Better understanding of the physical and electrical behaviour of the granular coke and graphite blends with respect to the pressure and temperature.

2. Better understanding of the impact of a specific lying-bed (related to pattern, coke/graphite ratio) on the evolution of the thermo-electrical behaviour of the cell during preheating phase.

3. Reduction of excessive stress in the cathode block (only qualitative evaluation by reducing the thermal gradient) while ensuring better baking of the ramming pastes which will give proper preheating of the whole cathode/lining.

4. The operational conditions to obtain the better preheating of the cathode.

As a long-term objective, the results of this project will lead to an improvement in cathode performance including an increase in cell lifespan and therefore, to a reduction in cathode costs as well as a reduction in harmful environmental effects due to lesser SPL.

The positive impacts of this project with AAI are not only limited to the costs savings for the aluminium industry but also in relation to the United Nations Sustainable Development Goals (SDGs). A well-preheated healthy cathode facilitates prevention of premature cathode failure in early life operation and enhances the longevity of the cathode in the operating cell, which gives smelters to reduce production cost (SDG 8). This also reduces the waste production (SDG 12) and carbon footprint (SDG 13) for the smelter by reducing the SPL per tonne of Al. produced, which is hazardous to the environment.

1.7 Methodology

Achieving the objectives of this project requires a methodology as follows:

1. Characterisation of the physical properties of the granular blends
2. Characterisation of the electrical properties of the granular blends
3. Identification of the key performance indicators for the cathode preheating
4. Adaptation of the thermo-electrical model to simulate the preheating phase
5. Determination of the better conditions for the preheating

1.7.1 Characterisation of the Physical Properties of the Granular Blends

The physical properties of the granular blends are determined experimentally to understand the behaviour of the lying-bed granular materials with or without the subject to pressures. Before conducting the tests to characterise the mixture, their bulk densities and granulometry of coke and graphite are determined separately to clearly specify the nature of material used by the industry for electrical resistive preheating.

The lying-bed material is coarse, irregular, granular and cohesionless in nature. To determine the ability of the granular materials to form a stable cone under its own weight, we need to find their angle of repose. The angle of repose is the steepest angle at which a pile of the material remains stable without collapsing. To get more information about the granular material under the normal load (along with the angle of repose which is useful for our project), direct shear test is carried out with the direct shear test equipment. To determine the compressibility of the granular material under the load, compaction test is performed.

Direct shear test gives us the information like shear strength and the angle of internal friction of the granular material. For cohesionless granular material, the angle of repose is approximately the same as the angle of internal friction. Compaction test gives us the information like axial strain and diametral strain for various loads. The above-mentioned physical properties are useful to optimise the true shape of the pucks in the lying-bed used

for the electrical resistive preheating. The angle of repose is used to determine the intermediate shape of the puck in the lying-bed during the cell preparation phase before the anode placement, whereas the axial and diametral strains of the granular material are used to determine the exact final puck shape after the installation of anodes on it. It should be noted that this final puck shape is not the actual shape through which the current will pass and generate heat by Joule's heating effect.

1.7.2 Characterisation of the Electrical Properties of the Granular Blends

The electrical properties of the granular blends are determined experimentally to understand the behaviour of the lying-bed material when they are subject to certain pressure and temperature simultaneously.

The electrical properties of the granular material like electrical resistivity and specific electrical contact resistivities are determined experimentally for the various granular blends. To do so, an experimental setup is developed in the CURAL's GRIPS laboratory. Both the electrical properties are determined as a function of temperature and pressure for the respective granular blends.

1.7.3 Identification of the Key Performance Indicators

To evaluate the cathode preheating performance, the key performance indicators for the cathode preheating are identified in agreement with our industrial partner — AAI. These

indicators are based on thermal, electrical and chemical considerations, each carrying a specific weight according to their importance to the industry needs.

1.7.4 Adaptation of the Thermo-electrical Model

The thermo-electrical (TE) ¼ cell preheating model is adapted to be able to consider various configuration of lying-bed as well as the physical and electrical properties obtained from the experimental study. The transient and strongly coupled non-linear model is developed using the ANSYS^{TM} platform. The model is developed and calibrated using available thermal, electrical and mechanical data obtained from *in situ* measurements from the AP4X aluminium reduction cells during its preheating phase. It is noteworthy to mention that the model can predict phase change of bath and baking of the ramming paste.

1.7.5 Determination of the Better Conditions for Preheating

First, the puck shape geometry is modified considering the previously obtained physical properties. Using the experimental determined electrical properties into the TE model, the preheating process can be simulated more precisely which facilitates giving the best possible conditions for the cathode preheating. Then, the better conditions for the best cathode preheating are identified by evaluating the key performance indicators.

1.8 Scope of the Thesis

This thesis examines the performance of aluminium reduction cells with a focus on lying-bed behaviour during cathode preheating for an optimisation purpose. **Chapter 1** introduces the background, objectives and methodology of the study, highlighting the challenges in newly started modern reduction cells. **Chapter 2** provides a comprehensive literature review covering modern aluminium reduction cells start-up and operation including parameters and performance indicators, and previous research associated with cathode preheating.

Chapter 3 presents the experimental work undertaken to characterise the granular blends used in the lying-bed and evaluate their physical and electrical properties relevant to reduction cell preheating. **Chapter 4** integrates experimental and modelling insights to propose optimal configurations and operating parameters for lying-bed optimisation. **Chapter 5** details the simulation methodology, including mathematical and numerical models developed to analyse lying-bed performance by key performance indicators under various operating conditions.

Chapter 6 concludes the thesis by summarising the key findings and provides recommendations for industrial applications and future research. In the end, the appendices contain supporting data and supplementary information related to this thesis; however, certain materials are not disclosed due to confidentiality constraints.

CHAPTER 2

LITERATURE REVIEW

2.1 General Information

The literature review required for this project is divided into some specific sections dedicated to the complete reduction cell start-up process with more focus on the preheating phase. Subsequently, parameters and key performance indicators for the modern aluminium reduction cells in start-up and operational phases are also discussed briefly. Furthermore, the physical and electrical properties of the granular blends (a mixture of coke and graphite with a certain ratio) used as a lying-bed for the electrical preheating are looked upon, which is of first importance in this project.

2.2 Reduction Cell Start-up Activities

To operate an aluminium reduction cell and produce aluminium efficiently, one must start the cell by an effective method. Starting up an aluminium reduction cell with a cathode at room temperature to a normal operating cell is a long and delicate procedure. To make a reduction cell operational, the cell needs to be prepared, preheated and started. Then a newly started cell goes through a normalisation period of a few weeks (mainly depending on the cathode quality and reduction cell technology) to produce efficiently [27].

The term start-up is normally used to describe the addition of molten electrolyte bath to the reduction cell and simultaneous current cut-in, *i.e.*, the period where the electrolytic production of aluminium is started. In a broader view, it involves all the phases that a cold cell (a newly lined/relined cathode) goes through to become a normal operating cell to be able to produce efficiently. Hence, we can collectively call them cell start-up activities. Thus, the start-up activities of an aluminium reduction cell is a lengthy procedure. It can be mainly divided into five phases as follows [27]:

1. Preparation.
2. Preheating.
3. Bath-up (Bath addition or generation).
4. Metal-up (Metal addition).
5. Early life operation (Cell normalisation).

It starts with the cell preparation phase then followed by preheating, bath-up and metal-up. The early life operation phase is also included in the complete cell start-up activities as in this phase the reduction cell is normalised *i.e.,* the cell parameters are gradually brought to the normal operating parameters (to become a normal operating cell). The complete start-up activities take around 3 weeks to 3 months depending on cathode quality and cell technology [28]. Our focus is on cell preheating will be described clearly in the next section under the subsection of current industry practice of cathode preheating.

Figure 2-1 illustrates reduction cell start-up activities with its timeline and typical industrial nomenclature.

Preheating, start-up and early life operation are important phases of cell life. Until now, there is no agreement among the smelters about optimal parameters and best work practices of preheat, start-up and early operation of the cells. However, most people agree on the abolition of radical methods of start-up, such as bath or metal addition without cell preheat, because of evidence of cathode damage, early failures and shorter cathode life [27].

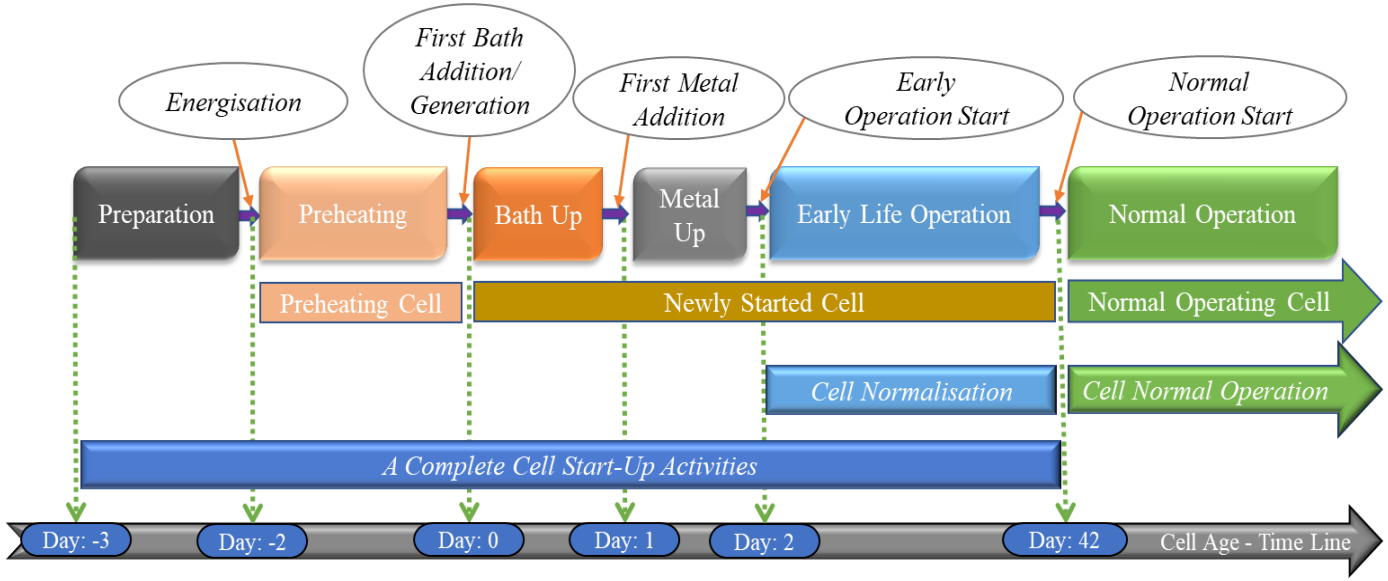

Figure 2-1 : Reduction cell start-up activities from a newly lined cathode to a normal operating cell

2.2.1 Preparation

After fabrication of a newly lined or relined reduction cell at the dedicated lining facility, the cell is transported to the potroom and installed in its designated location. The superstructure is then mounted, and all raw material handling systems and electrical connections are restored. Subsequently, the reduction cell is prepared for the preheating phase by blowing away the dusts on the cathode surface. A layer of a coke–graphite blend, referred to as resistive bed (or lying-bed), is placed over the cathode surface. The anodes are positioned on top of it and electrically connected to the anode beam using flexible conductors, as illustrated in Figure 2-2.

Figure 2-2 : A prepared reduction cell ready for energisation

Thermal insulating wool is placed in the central channel to insulate whereas soda ash (Na_2CO_3) is added in the side channel. Depending on the cell technology and operational practice, shunts are installed to initially bypass a portion of the electrical current. The cell is then covered with a crushed bath and closed with the side-hoods to provide thermal insulation [28].

2.2.2 Preheating

After the completion of cell preparation, the reduction cell is ready to be preheated. That is to heat the lining to the temperature of the service and to prepare the cell for pouring the molten bath while minimising thermal shock/stress. Currently, the aluminium industry prefers the electrical resistance preheating due to economic reason [29].

In case of electrical resistance preheating, the electric current is passed through the anode and cathode via the granular resistive bed layer. The electric current through this resistive bed layer (lying-bed) generates a high amount of heat due to Joule's heating effect and the temperature of both electrodes goes up gradually in the aluminium reduction cell during the preheating phase. The major heating source is the resistive bed layer between the anode and cathode (apart from the heating of electrodes due to their internal resistances). The heat generated from this layer transfers to the cathode and the anodes as well. Depending on the method and current intensity of the cell technology, the preheating lasts from 40 to 96 h. During preheating, the baking of the ramming paste takes place, the

cathode becomes monolithic and the volatiles from mortars, and vermiculite are released [29][30].

If shunts are used to bypass some of the DC initially, they are removed with a sequence after a period in line with the cell voltage decrease and the total current is passed through the cathode eventually for the preheating. The duct damper is kept closed during the preheating to retain the heat. Anode current distribution and cathode surface temperature at prefixed places are monitored frequently. Ideally, the surface temperature of the cathode should be close to the temperature of the bath (950 to 960 °C) that is poured into the cell and there should be no local overheating (above 1000 °C). The main issue of preheating is to avoid overheating or freezing of the cathode, which has a detrimental effect on it [29].

2.2.3 Bath-up / Bath Addition or Generation

When the required cathode surface temperature is obtained/reached and sufficient temperature exposure takes place, the anodes are tightened with the beam and the bath (tapped in advance from other operating reduction cells) is poured into it [27]. It is made sure that the poured liquid bath is free from the metal. This is done to allow the porous cathode surface to be sealed initially by cryolite bath rather than the metal. While pouring bath into the cell cavity at the tap end, the anode beam is lifted very slowly and very cautiously to increase the cell voltage. The reason being very cautious and slow is to avoid the open circuit while lifting the anodes out of the bath.

In the case of a dry start-up, a small amount of solid cryolite is added to the central channel frequently until it melts into the liquid bath for a bath generation. Otherwise, the liquid bath is poured into the cell (usually around 12 to 16 tonnes), and the cell voltage of around 8 to 9 V is maintained to generate the bath. To accelerate the bath generation a strong anode effect is initiated and maintained in the reduction cell for a period. After bath pouring, a very small amount of alumina (very low feed-rate) is added, because technically the electrolysis process has started. A significant amount of soda ash (Na_2CO_3) is added during the bath up phase. Anode current distribution is measured in regular intervals to make sure the anodes are fixed with the anode beam and not slipped from their positions which can lead to anode failures. The cell voltage is slowly decreased to 6 to 6.5 V over a period called as soaking period of around 16 to 32 h (depending on cathode quality, cell technology and work practice) [27] [29].

2.2.4 Metal-up / Metal Addition

After the soaking period (16 to 32 h) around 12 to 14 tonnes of molten metal (previously tapped from the other operating reduction cells) are poured into the cell while lifting the anode beam slowly by maintaining the same cell voltage. The soaking period allows [27]:

1. The more effective and efficient dissolution of anode cover material, alumina, *etc.* giving a clean cathode surface.

2. The sealing of cracks/gaps and open porosity in the lining to prevent future infiltration.

Anode current distribution is measured in regular interval to ensure the position of anode with respect to the anode beam and the abnormality in them. Then, the cell voltage is gradually reduced over a period from 6 to 5 V as the reduction cell gets stable after the metal pouring [29].

2.2.5 Early Life Operation / Normalization

After the metal pouring, in early life operation, all the cell parameters are gradually tried to bring back to the range of a normal operating cell after which the cell produces aluminium efficiently for the whole service life only if operated with proper thermal, mass and magnetic equilibria simultaneously. The cell early life operation (also called as cell normalisation process) lasts up to a few weeks depending on the cell technology and cathode quality [27][30].

In this phase, the cell is covered properly to avoid anode oxidation and maintain thermal balance. Cell parameters (like cell voltage, liquid heights, bath temperature, bath composition, instability, feed rate *etc.*) are slowly brought to the range of a normal operating cell from the range of a newly started cell over a period. For example, the voltage is slowly brought to a normal operating cell voltage of 4 to 4.2 V. The details regarding the cell parameters is elaborated in the subsection of *Parameters of a Newly Started Cell*. Duration of this phase depends on the quality and type of cathode blocks used in the cathode construction. The range of early life operation can vary from 21 days up to 90 days [29].

2.3 Preheating Phase

In this section, we focus on the types of cathode preheating, current industry practices, their disadvantages, and the parameters and performance indicators of electrical resistance preheating.

2.3.1 Different Methods of Cathode Preheating

There are several ways to preheat a cathode prior to start the reduction cell and the methods may vary with the type and size of the cells. For similar types and cell sizes, the preheating procedure may also differ from company to company and even various plants of the same company. The most important preheating methods are listed as follows [26][27][29]:

1. Preheating during anode bake-out (Söderberg cells only).
2. Liquid metal preheating (cold start).
3. Liquid bath preheating (cold start).
4. Thermal preheating (with oil- or gas-fired burners).
5. Electrical resistance preheating (with coke and/or graphite as the lying-bed).

Anode bake-out is only applicable for Söderberg cells, whereas other methods are applicable for prebake cells. Liquid metal and liquid bath (cold starts) are very harmful to cathode life as the liquid metal or bath is poured directly to cold cathode at room

temperature. These methods are not recommended for the modern reduction cell cathodes for the start-up. It can only be done for restart-up of cells after some potline eventualities like potline shutdown or shutdown of many reduction cells. With liquid bath preheating relatively new hot anodes are installed before the bath addition to reduce the risk of anode problems. Resistive preheating and thermal preheating (or flame preheating) are the two remaining best options for modern reduction cells. Currently, aluminium industry prefers electrical resistance preheating as it is less labour and capital intensive (although thermal preheating gives slightly superior results than the electrical resistance preheating). All other methods are interesting from a historical point of view only [29].

2.3.2 Current Industrial Practice of Cathode Preheating

It is necessary to preheat a newly lined/relined reduction cell. Currently, the two main methods of preheating are electrical resistance preheating and thermal preheating. Most of the smelters deploy the resistive bed method of preheating due to mainly economic reasons.

First, the lined/relined cell is prepared by vacuuming the dusts from the cathode surface by an industrial vacuum cleaner and then lying on the granular coke/graphite blend (Figure 2-3) by means of a special template mould followed by the installation of anodes on it and then connecting the anodes to the busbar with flexible conductors to pass the electric current. Particularly, in the preparation phase, a special template mould as

illustrated in Figure 2-4, (partially hidden due to confidentiality,) is used to lay the granular blend on the cathode surface.

First, the template mould is placed on the cathode exactly over the shadows of the anodes to be placed. Then the granular blend is poured and filled onto it. The template mould is lifted slowly to build the pucks on which anodes are placed. A set of 4 pucks in the lying-bed is illustrated in Figure 2-3.

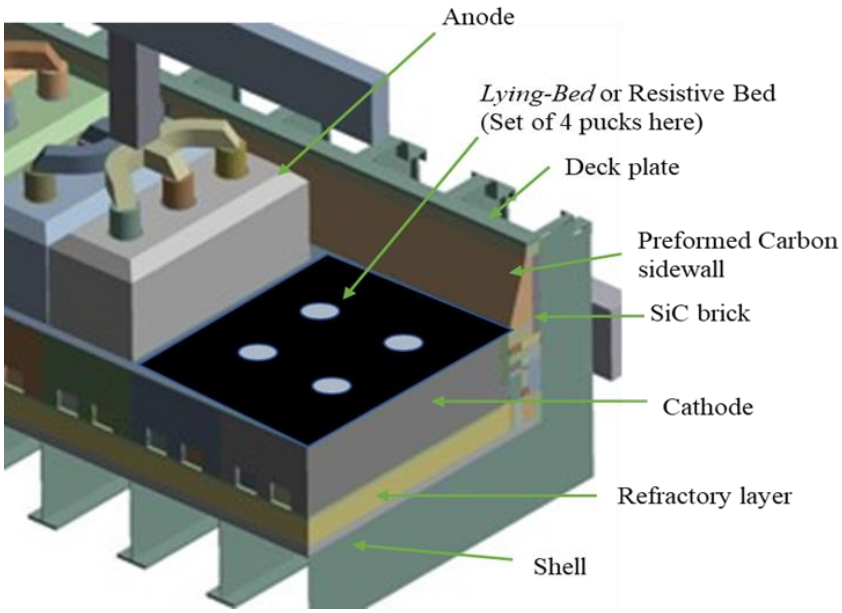

Figure 2-3 : An electrical preheating arrangement with lying-bed

To retain the heat energy, the cell is covered to insulate thermally by insulating blanket in the central channel, by crushed cryolite bath (Na_3AlF_6) on top of the anodes, and by soda ash (Na_2CO_3) in the side channels. The channels in between the anodes are also covered using thermal insulation wools before covering the anode by crushed cryolite bath as shown in Figure 2-5.

Figure 2-4 : A typical template mould used in the industry

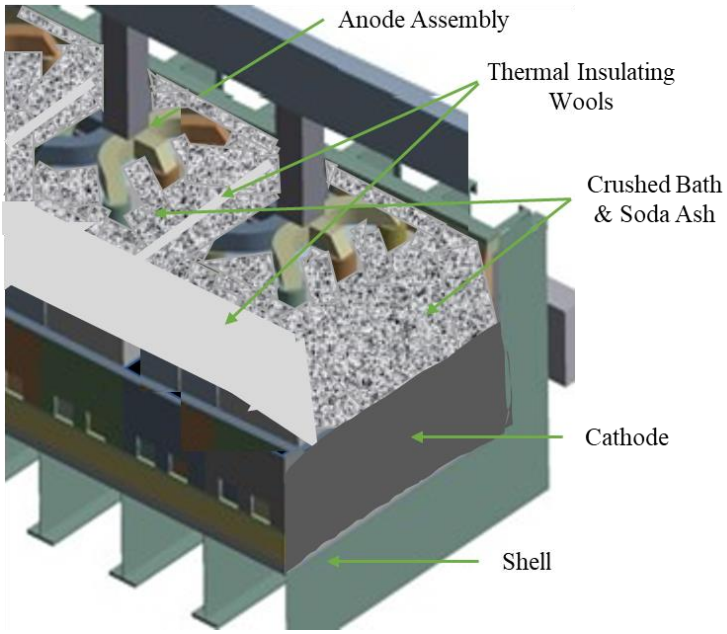

Figure 2-5 : A typical electrical cell preheating arrangement

Then the cell is energised by passing the full current load of 400 kA without any shunts. The electric current through the set of pucks in the lying-bed generates enormous heat due to Joule's effect of heating and the temperature of both electrodes goes up gradually in the aluminium electrolysis cell during this phase. The preheating phase lasts 48 h. The anode current distribution and cathode surface temperature are measured in every 4 hours to monitor the preheating. When the average cathode surface temperature reaches 850 ℃, the tapped bath is poured into the cathode.

In case of dry start-up, the heating effect of the electrical current melts the crushed bath loaded earlier. Crushed bath in small amounts is added frequently in the central channel of the cell gradually to melt and produce electrolyte bath. To accelerate the bath production anode effect is brought and hold for a period and /or tapped bath is added.

2.3.3 Disadvantages of the Electrical Resistance Preheating

Electrical resistance and gas-fired preheating are two common methods used to raise the temperature of the cathode lining in aluminium reduction cells before start-up, each with distinct advantages and limitations. Electrical resistance preheating relies on passing current through resistive material or the lying-bed to generate heat. While it provides a relatively simple and controllable heating method, it suffers from high energy consumption, uneven heating, and slow heating rates. In contrast, gas-fired preheating uses burners to directly supply thermal energy to the cell cathode, providing faster heating rates and more uniform temperature distribution. Gas preheating allows more flexibility

in controlling the heat input spatially across the cell cathode. However, it introduces emissions of CO and CO_2, requires complex burner installation, and necessitates continuous monitoring to avoid hot spots or lining damage. While electrical resistance preheating is electrically intensive and relatively slow, gas-fired preheating offers speed and uniformity but at the cost of fuel consumption, safety considerations, and environmental concerns [27].

Although aluminium industries, currently, preheat their electrolysis cells by electrical resistance preheating due to economic reasons, there are certainly some shortcomings of this procedure (Figure 2-6). The main disadvantages are listed as follows [31]:

1. Rapid and localised increase of cathode surface temperature.

2. Non-uniform temperature distribution on the cathode surface and through the cathode.

3. High thermal gradients during preheating.

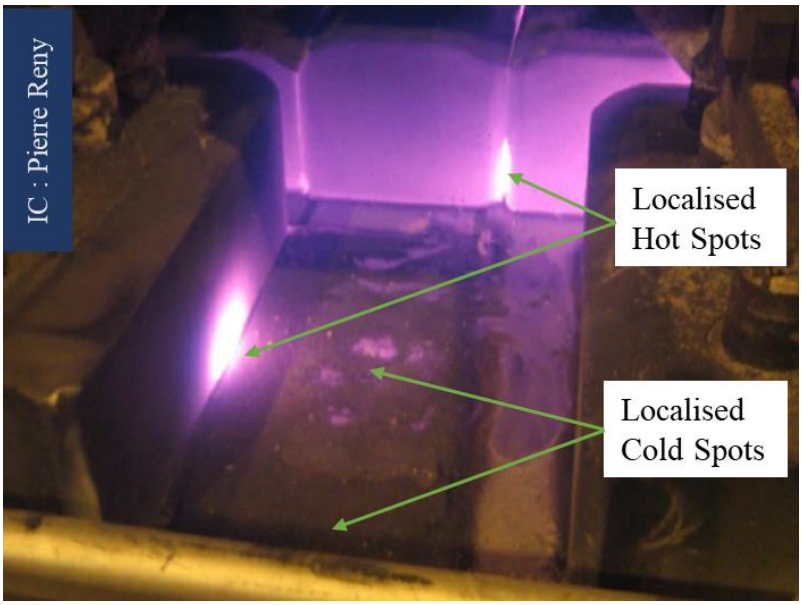

Figure 2-6 : Localised hot spots and cold spots on the cathode

2.3.4 Parameters of the Electrical Resistance Preheating

The parameters which control the electrical resistance preheating may be summarised as: lying-bed configuration, amperage of reduction cell, duration of preheating and covering of the preheating cell [27] [28].

The lying-bed can vary in layouts, compositions and heights. In its layout, it varies by cell technology and work practices—either fully or partially covering the anode shadows. In the latter case, it may be rectangular-, square-, line-, or circular-shaped. In its composition, it varies by the granular material composition—ratio of granular coke and graphite used in the lying-bed. Lying-beds of similar layout and composition with

different heights are also used. Figure 2-7 illustrates various typical layouts used in the aluminium industries for electrical resistance preheating.

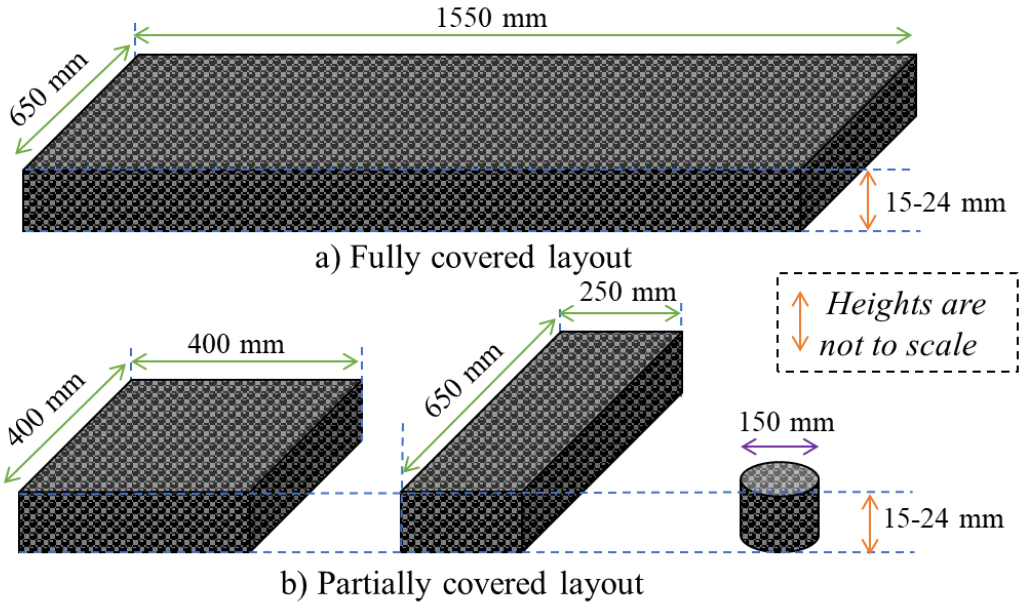

Figure 2-7 : Typical lying-bed layouts used in industries

Cathodes are preheated by passing a full or partial direct current. Shunts are used to bypass some of the current. This current bypassing is done to avoid the electrical shock to the cathode at the energisation. Shunts are taken away from the system after some time and full current is passed to preheat the cell.

Sometimes, the duration and cover thickness of the preheating is also changed to have a desired cathode temperature distribution. It is not uncommon that cells are preheated for longer periods to have the desired cathode temperature with no crushed bath covering on top of the anodes.

2.3.5 Performance Indicators of Cathode Preheating

It is important to evaluate the quality of cathode preheating in terms of some performance indicators. The performance indicators and the list of criteria proposed by Kvande to evaluate the cathode preheating are given in Table 2-1 [33].

Table 2-1 : Performance indicators of cathode preheating [33]

No.	Performance Indicator (PI)	Ideal result
1	Final average cathode surface temperature	Close to 970 to 1000 $°C$
2	Final cathode surface temperature distribution	*RSD less than 10%
3	Anodic current distribution	*RSD 10 - 15%
4	Cathodic current distribution	*RSD 10 - 15%
5	Cathode heat-up rate	Between 5 - 50 $°C/h$, Typical value: 20 $°C/h$
6	Vertical thermal gradients	Sub-cathodic temperature at start-up more than 700 $°C$

*RSD – Relative standard deviation is given by

$$\text{RSD} = \frac{\text{Standard Deviation}}{\text{Mean}} \cdot 100 \qquad \textbf{(2-1)}$$

In practice, the preheating phase is monitored by measuring the cathode surface temperature at certain prefixed points and anode current values of all the anodes. The heat-up rate is calculated from the measured cathode surface temperature with respect to the time of preheating. When the average final cathode surface temperature reaches to a desired value of approximately 800 to 850 °C, the molten bath is poured into the cathode. Measurement of cathodic current distribution is very rare, and it is directly linked with the cathode surface temperature distribution and anode current distribution. Vertical thermal gradients are of less importance with graphitic and graphitised cathode blocks as they conduct heat very well [26].

An increase in cathode life, resulting in higher tonnes of aluminium produced per kilogram of cathode material, can serve as a meaningful performance indicator of preheating quality (which includes the influence of operational practices and philosophy). However, this indicator reflects long-term performance and typically becomes tangible only after 6–7 years of cell operation. To evaluate the effectiveness of cathode preheating within a shorter time frame, the early operational stability of a newly started cell is a more appropriate and practical indicator. Improved operational stability is characterised by reduced anode effect duration (AED) and anode effect voltage or complete elimination of the anode effect (AE) in bath-up phase, and lower operating voltage in newly started cells. These indicators can be directly attributed to effective cathode preheating [30] [34][35].

2.4 Lying-bed: Its Properties and Characterisation

Calcined petroleum coke was used as the lying-bed for the reduction cell preheating earlier for both amorphous and anthracite types of cathode blocks. In these cases, the preheating time was shorter, resulting in a very fast temperature increase. To achieve a smoother temperature increase with lower temperature gradients in the lining, it is necessary to replace the coke with graphite for these cathode blocks. The graphite resistive bed has the extra advantage that its electrical and thermal conductivities will change in a predictable manner as a function of temperature [27].

Currently, smelters are mainly using (semi-/fully-) graphitic or graphitised cathode blocks. If graphite resistive bed is used for these cathode blocks, the heating rate will be reduced substantially. This is due to the lower electrical resistivity of both graphitic/graphitised cathode and the graphite as a resistive bed. Therefore, a mixture of calcined petroleum coke and graphite is used as a lying-bed for the electrical preheating of modern reduction cell cathodes [31].

The anodes are placed on the pucks to preheat the cathode by passing DC. The weight of the anodes exerts a mechanical pressure on the granular blends. It is also observed that during preheating, the cathode plane bends slightly which brings the change of pressure on the granular blends [22]. The DC passed through the pucks raises its temperature gradually due to Joule's heating effect and the heat get transferred to both anodes and

cathode surfaces. Thus, pucks in the lying-bed stay under the pressure and temperature simultaneously.

First, the granular materials are flowable. The flowability nature of the granular blends which mainly depends on the particle shape, the particle size distribution and the surface roughness. In the literature, we can find the flowability properties of the granular materials like sand, clay, soil, gravel, *etc.*, mainly in geomechanics. The exact flowability properties of the granular blends coke and graphite need to be determined to describe these physical phenomena accurately.

Second, the granular material gets compressed with the application of load on it. The effect of the loads on these granular blends needs to be studied also.

Lastly, the electrical resistivity of the granular blend changes with respect to the temperature rise during the preheating phase and the pressure exerted on them. In the literature several studies are being carried out on the electrical resistivity of the granular coke and graphite separately only considering the temperature effect on it.

Krogerus *et al*. [36], Eidem *et al*. [37], Surup *et al*. [38], Miroshnichenko *et al*. [39] have studied the electrical resistivity/conductivity of the granular coke of varying particle size distribution with the function of temperature only, used for the various furnaces. The results show that the electrical resistivity has a negative temperature coefficient and varies with the types of the granular coke and its particle size distribution.

Electrical resistivity of synthetic granular graphite is studied by Paraskevoulakos *et al*. [40] considering the effect of temperature and porosity. The results show that electrical resistivity has a negative temperature coefficient and porosity plays a role to amplify it.

The physical and electrical properties of the lying-bed blend undergo several changes during cell preheating due to changes in temperature and pressure. Their transient nature and lack of knowledge regarding the mixture properties make it more difficult to optimise the lying-bed using the conventional trial and error method [41]. So, it is important to determine the physical and electrical properties of the granular coke and graphite mixture as a function of pressure and temperature.

2.5 Newly Started Reduction Cells

As illustrated in Figure 2-1, the cell, after the bath-up until it finishes its early life operation, is called as a newly started reduction cell. Thus, a newly started cell goes through a bath-up and metal addition followed by the long early life period to become a normal operating reduction cell [27].

2.5.1 Parameters

During the cell start-up activities, all the cell parameters (*e.g.*, cell voltage, liquid heights, bath temperature, bath composition, instability, feed rate, *etc.*) are scattered in wide range as compared to that of a normal operating cell. To produce aluminium efficiently, all the

cell parameters are brought gradually to the range of a normal operating cell [29]. The parameters of a newly started cell mainly are given as follows:

1. Cell voltage and bath temperature
2. Al_2O_3 and AlF_3 feeding rate
3. Composition of the bath
4. Liquid level heights in the cell
5. Cell instability/noise level
6. Current efficiency and Al tapped

Here, all the parameters are briefly discussed and shown for the newly started cells running at 400 kA using semi-graphitic/graphitised cathode having four point-feeders of each 1 kg shot of alumina and having 6 weeks of early life operation period. Very similar trends are also observed for other newly started high-amperage reduction cells. The parameters presented here are very generic for 400-kA reduction cells (completely independent of any specific cell technology) and are in line with the existing literature [28][29][34].

Figure 2-8 shows the gradual decrease in cell voltage and bath temperature in the early life operation phase. Alumina (Al_2O_3) and aluminium fluoride (AlF_3) intake of the cell increases slowly as shown in Figure 2-9. The bath compositions (AlF_3 & CaF_2) are kept as shown in Figure 2-10. Along with the bath composition, simultaneous decrease in the bath inventory and increase in the metal inventory (Figure 2-11) is followed which helps to stabilize the newly started cell with lowering the cell instability (Figure 2-12).

In newly started reduction cells, due to the comparative higher bath temperature and lower excess $AlF_3\%$ in the bath, the reduction cell production remains in the moderate level giving a moderate current efficiency. Thus, the lesser metal is siphoned according to the production (Figure 2-13) to build the metal inventory as shown in Figure 2-11. The trend in the impurities (mainly Fe and Si) in the metal (see Figure 2-14) gradually decreases.

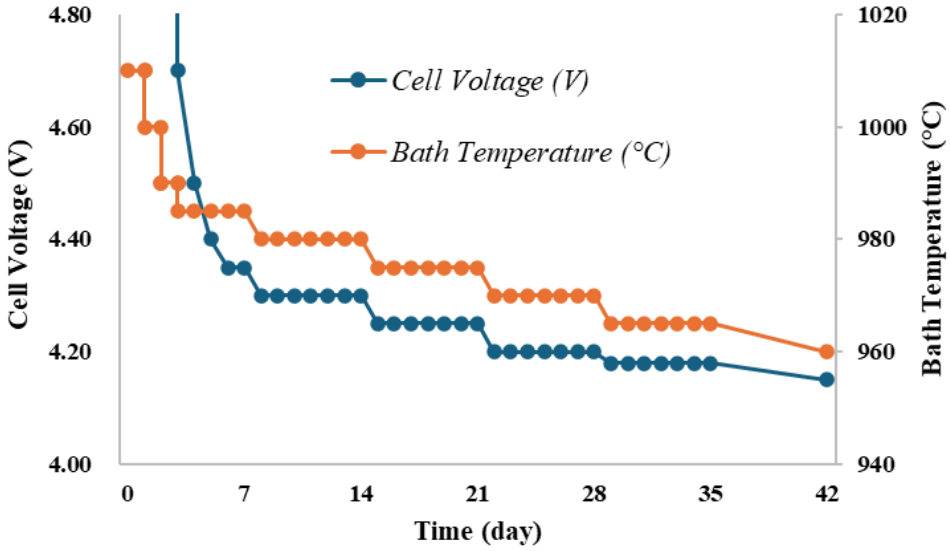

Figure 2-8 : Cell voltage and bath temperature in newly started cells

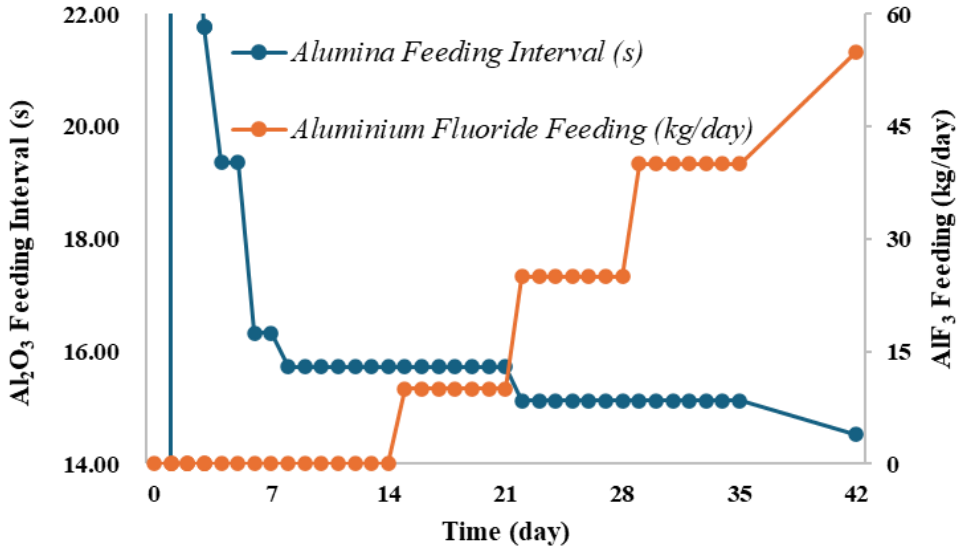

Figure 2-9 : Alumina and aluminium fluoride feeding in newly started cells

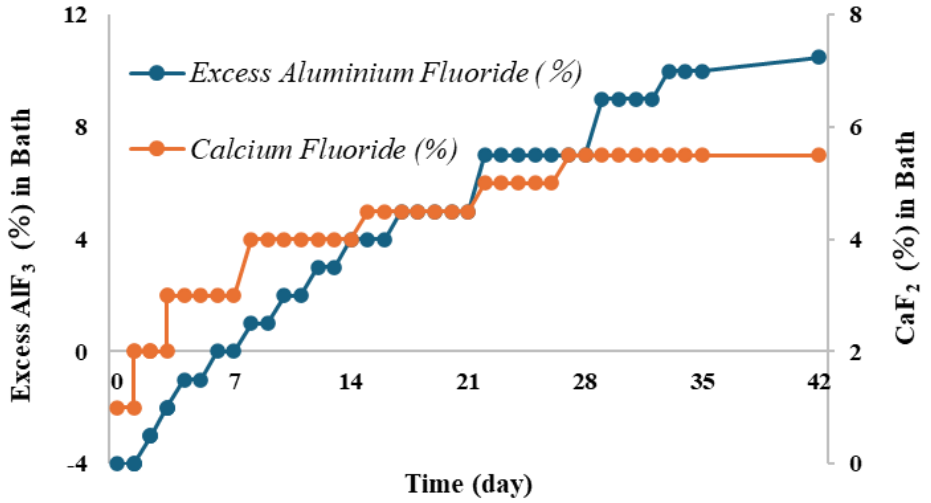

Figure 2-10 : Composition of the bath in newly started cells

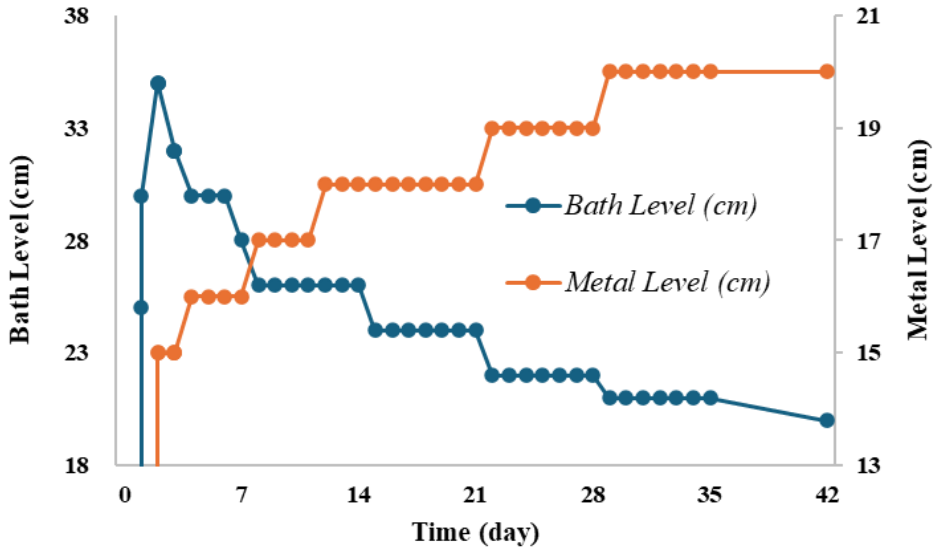

Figure 2-11 : Liquid level heights in newly started cells

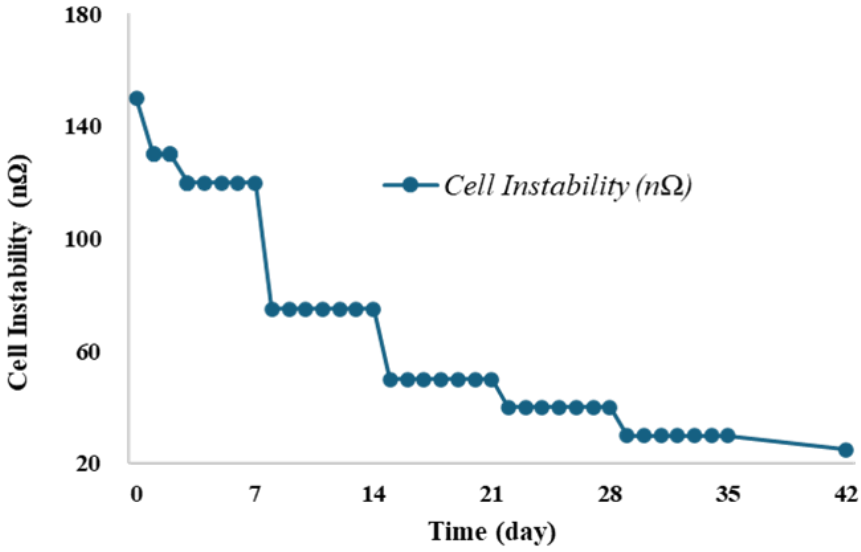

Figure 2-12 : Cell instability in newly started cells

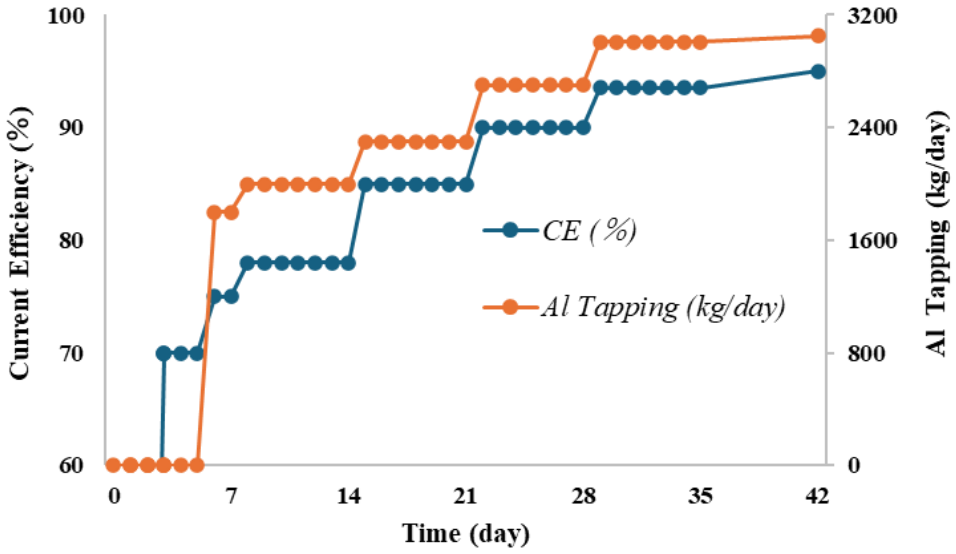

Figure 2-13 : Cell production in newly started cells

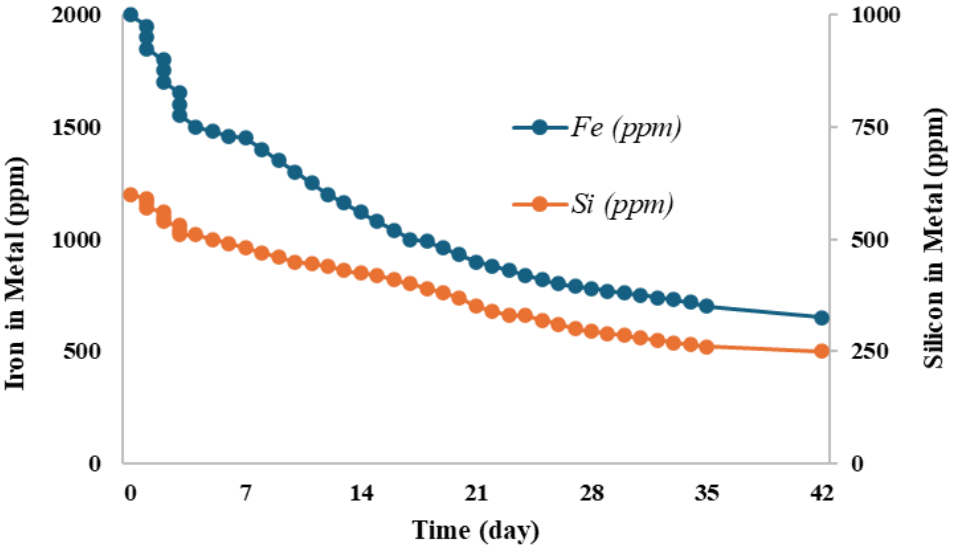

Figure 2-14 : Impurities in metal in newly started cells

2.5.2 Characteristics and Performance

There are several notable features of a newly started reduction cell that are abnormal when compared with the operating characteristics of a cell after it has been in use for more than three months. Most of these differences can be attributed to interactions associated with the newly formed cathode [5]. The features which differentiate a new cell from the conditioned ones are:

1. New cells during early life require the addition of a considerable amount of soda ash.

2. New cells during early life produce a limited amount of metal.

3. New cells during early life require bath addition whereas the older cells generate bath.

4. Side ledge formation.

During the early life of the cell, it is necessary to add a considerable amount of soda ash (Na_2CO_3) — sodium carbonate which is equivalent to adding sodium fluoride (NaF) to maintain the composition of the electrolyte bath. Over the first three weeks of early operation, nearly 1.5 tonnes of soda ash are required to make up for NaF and to maintain the composition of electrolyte bath. It is obvious that there are some other sources of loss of the sodium fluoride, and there are two fundamental theories associated with this. The first of these theories is based on the selective absorption of sodium fluoride by the cathode lining, while the second is based on the direct deposition of sodium on to the carbon. Analyses of laboratory test specimens as well as samples taken from spent

cathodes indicate that the carbon specimens become impregnated with sodium while the interconnecting pores are filled with a bath. The sodium absorption is much more intense during the initial period of electrolysis [5].

Another characteristic of the early life of a newly started reduction cell is the limited amount of metal production. Lack of precise inventory controls and detailed knowledge of the extent of the side ledge in a new cell make it difficult to assess this difference quantitatively. It would, however, be consistent with sodium deposition. While it is assumed that there is the uptake of electrolyte by the new cathode lining, the quantitative figures are masked by the difficulty in determining the amount of bath frozen on the sidewalls of the cell. The bath ratio during the first two months is sufficiently high for the electrolyte to wet the carbon. Sodium adsorption by the cathode carbon also aids its wetting by the bath. The intensely positive capillary pressures that result ensure that the penetration of the electrolyte through the open pores in the cathode lining is almost as fast as the sodium movement. Microscopic examination of cross-sections show that the greatest amount of bath uptake is through the pores of the carbon arising from the binder pitch, especially where there have been poor anthracite-pitch interactions [5].

A newly started cell needs a lot of baths at the initial early life operating period apart from the bath poured during bath up phase. This may be attributed to the formation of the side ledge, bath uptake by new cathode lining and selective adsorption of sodium fluoride as discussed earlier. Once the cell is started and is operated normally, it becomes net

producer of the bath although there exist some losses of the bath in the electrolysis process as mainly physical losses and vaporisation [5].

2.6 Study of the Cathode Preheating in Past Years

In this section, the previous works done related to aluminium reduction cell preheating over the past years are summarised below to assess the originality and the state of this project until now.

Modelling work by Asadi *et al.* [42] showed that the block stress level during a resistive bed preheating could be significantly reduced by modifying the heat distribution input to reduce the thermal gradients. If one could reduce the thermal gradient during preheating, the stress build-up in the block would also be lower.

Dupuis *et al.* [43][44] developed a transient thermo-electric model calibrated by comparing the predictions with the measured temperature evolution curves. According to Dupuis, during the preheat phase, the thermal gradients can be minimised by using different coke bed patterns thus the stress on the cathode linings is also minimised.

Richard *et al.* [45] presented a thermo-chemo-mechanical slice model which predicts the impact of the preheating on the stress distribution in the cathode block and the baking level of the ramming paste. The results showed that some ramming paste is still not baked properly even after 24 h of preheating.

According to Rye [35], a well-prepared lying-bed can give a uniform temperature distribution in the pot, but accurate leveling of the lying-bed and close follow-up during preheating phase are required to achieve this goal.

Ali *et al.* [46][47] studied the duration, the energy consumption of the preheating and the performance evaluation of the coke bed preheating method for the Egyptalum.

Based on the cathode preheating best practices by Kvande, Zangiacomi *et al.* [23] studied the cathode surface temperature distribution and the thermal gradients for a better understanding of the preheating phenomena.

Marceau *et al.* [48] modelled a thermo-electro-chemo-mechanical behaviour of the quarter-cell model during its preheating phase. The contact conditions show that sliding and separation occur mainly for the cathodes at the extremities of the cell, and it is most significant for the last cathode block.

Arkhipov *et al.* [49] have studied the different configurations of graphite lying-bed and validated the model predictions during the start-up phase of EMAL potline 3.

Recently, Reny *et al.* [32] have published their work on the modification of the lying-bed pattern to improve the cathode surface temperature distribution to minimise the energy consumption during the preheating phase for the Karmøy technology pilot plant in Norway.

More recently, Huang [30] has published his work regarding the preheating optimisation in 500 kA cells. In this work, the particle size range of the granular coke is reduced from 2-6 mm to 2-4 mm by mechanical crushing and strict sieving to have uniform anode current distribution and lining temperature distribution. In addition, the focus is to have an air-tight anode covering and improved shunt removal procedure. Following these steps, he stabilised the newly started cells earlier, which is a sign of a good cathode preheating.

More recently Borim *et al.* [50] have published their work. They shun away from the dry start-up method to conventional start-up with some modifications. The modifications include the lying-bed with granular graphite instead of granular coke-graphite mixture, variation in the diameter and the thickness of the lying-bed in different positions and improvement in insulation to restrict heat loss during preheating. All these measures are taken to obtain better results for preheating which is demonstrated by the stability of the newly started cells.

2.7 Normal Operating Reduction Cells

Normal operation of aluminium reduction cells involves maintaining a stable electrochemical environment in which alumina is continuously dissolved in the molten cryolite bath and electrolytically reduced to aluminium at the cathode.

During normal operation, the cell runs at a very stable high current and a controlled cell voltage, ensuring efficient energy use. Feeding of the essential raw materials, siphoning of produced molten aluminium and maintenance of the reduction cell is mainly carried

out in certain intervals. Various measurements and samplings are done to ensure and correct the normal cell operating parameters. The molten electrolyte bath composition, its temperature, superheat, and alumina concentration are kept within narrow limits to avoid anode effects and ensure rapid alumina dissolution. The cell voltage is monitored continuously concerning alumina concentration and it is maintained at the desired cell voltage by adjusting the anode beam movements and the alumina feed rate in the cell [51][52].

The metal pad remains stable and well distributed, supported by advanced magnetic compensations and proper anode to cathode distance (ACD). Balance between heat generation and heat loss ensures a stable side ledge profile, which protects the cell lining. Under these conditions, the cell achieves optimum current efficiency and energy consumption, minimal disturbances, and a long cathode life [51].

2.7.1 Operational Activities

In normal operating aluminium reduction cells, routine operational activities are essential for maintaining a stable and efficient electrolysis process. In reduction cell operational activities, the major routine events carried out in regular intervals are as follows [53]:

1. Al_2O_3 and AlF_3 feeding.
2. Anode change and covering.
3. Molten metal siphoning

4. Beam raising
5. Measurement and sampling

Alumina (Al_2O_3) and aluminium fluoride (AlF_3) feeding ensures that the bath composition remains within the desired range, preventing concentration imbalances and anode effects. In modern reduction cells, the 'point breaker/feeders' supply alumina and aluminium fluoride at controlled intervals to maintain concentration stability in the electrolyte bath.

Anode change and covering are performed to replace consumed prebaked anodes and maintain proper anode to cathode distance (ACD), ensuring consistent current distribution and minimising energy losses. Prebaked anodes are regularly replaced in a pattern (typically in 20 to 24 days), in modern reduction cells by means of a very sophisticated equipment called as Pot Tending Machine or Assembly (PTM/PTA) as shown in Figure 2-15. Then, the newly replaced anodes are covered within 2 to 4 hours after the anode change to protect them from air oxidation.

Molten metal siphoning is carried out periodically to remove liquid aluminium from the reduction cells, maintaining an optimal metal pad thickness and preventing overflow or short-circuiting. Molten metal is siphoned out to a crucible by means of a vehicle or PTA and then sent for casting.

Beam raising also called as rack raising, the adjustment of the superstructure anode-beam to compensate the anode consumption which ensures further anode consumption and

movement of the anode beam, is done without disturbing the anode to cathode distance (ACD). It is carried out by means of a special pneumatic equipment called as Anode Beam Raising Frame (ABRF).

Figure 2-15 : Anode change operation in a prebake reduction cell

Measurements of liquid (bath/metal) heights, electrolyte bath temperature and anode current distribution are done in a regular interval. Sampling of electrolyte bath and metal are done to investigate the bath composition and metal quality respectively which provide critical feedback for process control, allowing operators to adjust feeding, voltage, and the current to sustain optimal cell performance. Together, these activities are integral to the smooth, safe, and efficient operation of high-amperage prebake aluminium reduction cells.

2.7.2 Parameters

A normal operating aluminium reduction cell is characterised by a well-controlled set of process parameters that ensure stable electrolysis and high efficiency. The operating current is maintained at a fixed level—typically 350–600 kA in modern reduction cells—while the cell voltage remains steady in the range of 4.15–3.90 V, reflecting balanced ohmic and electrochemical conditions [54].

Bath chemistry is tightly controlled, with the excess AlF_3 content typically 10–12%, and with a controlled stable cell voltage which gives a stable operating bath temperature. The bath superheat (ΔT) is maintained between 8–12 °C to ensure proper alumina dissolution and stable side ledge formation. Alumina concentration in the electrolyte bath is held within 2–3%, avoiding both sludge formation and anode effects [55][56].

The anode to cathode distance (ACD) is kept at an optimum distance and stable to minimise energy consumption while preventing metal pad instabilities. The metal pad remains smooth and well distributed due to proper magnetic compensation and uniform anode setting in modern aluminium reduction cells [57].

All the above discussed conditions lead to a desirable superheat window which gives a healthy side ledge profile, and gas release is controlled through efficient point feeding and cell gas exhaust system. Under these optimised conditions, the cell achieves minimal disturbances, high metal production, low energy consumption and prolonged cell life. Table 2-2 shows typical generic parameters for a normal operating modern reduction cell.

The modern reduction cell is equipped with four alumina feeders and one aluminium fluoride feeder, each configured to deliver 1 kg shots of alumina and aluminium fluoride, respectively.

Table 2-2 : Typical parameters of a normal operating cell [52, 56]

Parameter	Value	Unit	Comment
Cell Amperage	400	kA	*Very stable DC*
Cell Voltage	4.15 ± 0.10	V	*Lower is preferable*
Al_2O_3 Feeding Interval	14.5 ± 5.0	s	*Depends on feeding strategies*
AlF_3 Feeding Interval	25 ± 1	min	*Function of cathode quality, age and cell conditions*
Bath Temperature	960 ± 5	$°C$	
Excess AlF_3	10.5 ± 1	%	
CaF_2	5.5 ± 0.2	%	
Bath superheat (ΔT)	8 ± 4	$°C$	*It is maintained by Cell Voltage and Excess AlF_3*
Anode Cover Thickness	10 ± 1	cm	
Metal Level	20 ± 1	cm	
Bath Level	20 ± 1	cm	
Cell Instability	45 ± 10	$n\Omega$	
Cathode Voltage Drop	280 ± 40	mV	*Function of cathode quality, age and cell conditions*
Anode Current Distribution	-	mV	*Uniformity is desired. Value depends on the probe length*

2.7.3 Performance Indicators

Performance indicators of normal operating aluminium reduction cells provide a quantitative measure of the cell's efficiency, stability, and overall health. Performance indicators include specific energy consumption (SEC), typically 13.0–14.0 kWh/kg Al, indicating energy efficiency (EE) and current efficiency (CE) which corresponds to the metal production. CE ($-or\ \%$) generally represents the fraction of the current contributing to aluminium production. Metal purity shows the quality of metal produced [53].

Consumption of raw materials in the reduction cells, like alumina, aluminium fluoride and anode carbon are also evaluated by the performance indicators. Cathode age or life is a critical performance indicator which reflects the durability of the lining and effectiveness of thermal management. Anode effect frequency (AEF), anode effect duration (AED) and HF emission are other performance indicators, showing proper alumina feeding and process stability. Collectively, these indicators allow smelters to monitor their operational efficiency, optimise raw material and energy consumption, and maintain stable, long-term aluminium production. All of them are listed in the Table 2-3. In the next subsections, we will discuss about some of the important performance indicators in detail [53][56].

Table 2-3 : Typical performance indicators of a normal operating cell [54, 57, 58]

Performance Indicator	Value	Unit	Comment
Specific Energy Consumption (SEC)	13.30 ± 0.10	$kWh/kg\ Al$	*Depends on CE*
Current Efficiency (CE)	94.50 ± 0.25	%	
Metal Production	3052 ± 50	kg/day	*Depends on CE*
Metal purity	$>$ 99.800	%	*Al purity*
Al_2O_3 Consumption	1950 ± 50	$kg/t\ Al$	
AlF_3 Consumption	18 ± 2	$kg/t\ Al$	
Gross Carbon Consumption (GCC)	530 ± 10	$kg/t\ Al$	
Net Carbon Consumption (NCC)	410 ± 10	$k/t\ Al$	
Cathode Life	2000 ± 50	day	
Anode Effect Frequency (AEF)	$<$ 0.1	$AE/day/cell$	
Anode Effect Duration (AED)	$<$ 3	s	
HF Emission	$<$ 0.2	$kg/t\ Al$	

Specific Energy Consumption

By their very nature, all electrochemical processes are energy intensive since it is necessary to have an energy input to bring about a reaction that is normally unfavourable. Specific energy consumption (SEC) is the most important performance indicator for a normal operating reduction cell as it accounts for both the cell fractional current efficiency and cell to cell voltage. Simply, SEC is the amount of energy consumed to produce 1 kg of Al and is expressed in kWh/kg Al as follows [8]:

$$\text{Specific Energy Consumption, SEC} = \frac{2.980 \cdot V_{cell-cell}}{\eta_c(-)} \qquad \textbf{(2-2)}$$

From the above equation, the energy consumption can be reduced by minimising the cell-to-cell voltage having same/high current efficiency or increasing the current efficiency keeping same/less cell-to-cell voltage. The SEC for modern reduction cells is around 13.25 kWh/kg Al whereas the theoretical energy to produce aluminium at 960 ℃ is 6.65 kWh/kg Al [60]. Thus, the process energy efficiency (EE) is approximately 50%, stays low as a lot of energy is lost to the surroundings.

Current Efficiency

In every technical electrolysis process, there are losses which mean that the output will be less than the theoretical amount given by Faraday's laws of electrolysis. To account for these losses or to measure the electrochemical efficiency, the concept of current efficiency (CE) is introduced as the ratio between measured and theoretical production

for a specific period and is normally expressed in fraction or percentage . It is given by the following equation [8]:

$$\text{CE, } \eta_c = \frac{\text{Measured Production}}{\text{Faraday's Theoretical Production}} \quad \textbf{(2-3)}$$

According to Faraday's laws of electrolysis, 1 kA of DC current in 24 h produces 8.053 kg of aluminium. So, for industrial purpose calculation, it can be simplified as:

$$\text{CE, } \eta_c = \frac{\text{Metal Production in 24 h}}{(8.053) \cdot (I_p)} \quad \textbf{(2-4)}$$

The significance of the CE is how efficiently the electric current is used in the reduction cell for producing aluminium. In other words, the higher the CE, the higher the production of aluminium in the reduction cell. The current efficiency for modern reduction cells is around 0.935 to 0.950 (or 93.50 to 95.00%) [12].

Metal Purity

The quality of metal produced is evaluated by its purity values often expressed in percentage (%) or parts per million (ppm). The complete analysis of the metal purity is given in the Table 2-4. The main impurities analysed are iron, manganese along with silicon content. The purity of metal is mainly dependent on the quality of raw material used in the reduction cells like, alumina, anode, anode cover material, *etc.* and the

operational work practices as well. Aluminium of purity 99.90% is produced in high purity reduction lines for electronic usages with all the precautions with the raw materials, operational practices and FTP/GTC [51].

Table 2-4 : Typical composition of produced metal [61][62]

Element	Value in %	Value in ppm
Al	99.8400	998400
Fe	0.0500	500
Mn	0.0500	500
Si	0.0250	250
Ti	0.0040	40
P	0.0040	40
V	0.0080	80
Zn	0.0020	20
Ga	0.0060	60

Anode Consumption

Carbon anodes consumption represents a major production cost in the primary production of aluminium after the energy and alumina. Theoretically, the minimum limiting electrolytic consumption necessary to produce aluminium is 334 kg C/t Al. Accounting for a current efficiency of modern cells approximately 95%, electrolytic consumption increases to 352 kg C/t Al. The anode performance in modern smelters are measured by net carbon consumption (NCC) which is around 410 kg C/t Al. In addition, the carbon

consumption with spent butts is around 525 kg C/t Al which is known as gross carbon consumption (GCC). Figure 2-16 shows a typical carbon consumption in the modern aluminium reduction cells [63].

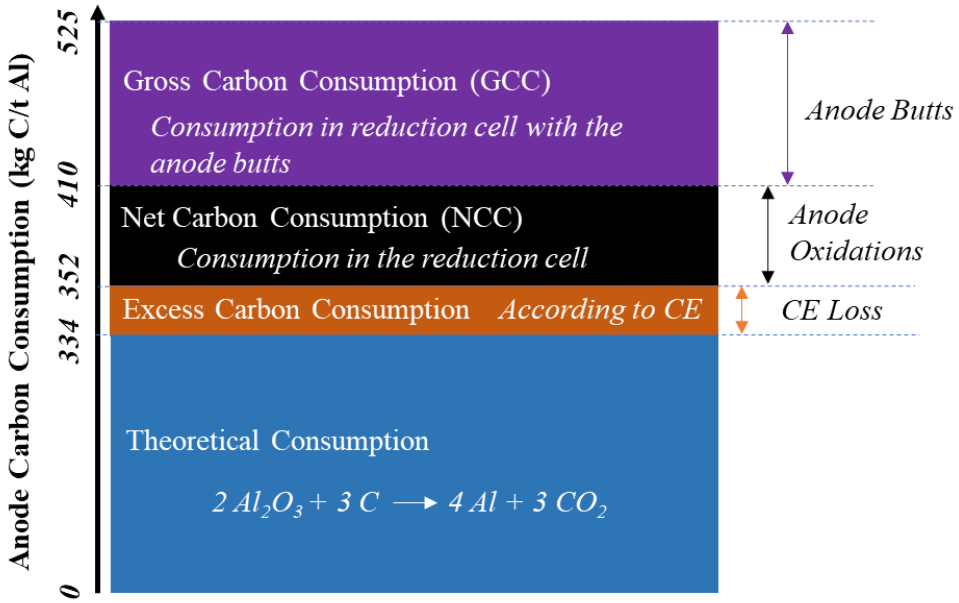

Figure 2-16 : A typical carbon consumption in the aluminium electrolysis [63]

The large difference is influenced by excess anode consumption by numerous factors as anode quality, operation related, and design related. The excess carbon consumption can be attributed to [63]:

1. Air oxidation/ O_2 oxidation (air-burn which is exothermic).
2. Carboxy attack/CO_2 oxidation (endothermic Boudouard reaction in the immersed anode pores and surface immediately above the electrolyte bath).
3. Selective oxidation (dusting & sloughing in the electrolyte bath).

Cathode Life

Cathode life is one of the most important performance indicators of an aluminium reduction cell, as it reflects the durability, stability, and overall effectiveness of cell operation throughout its campaign. It represents the length of time the cathode lining remains operational before failure, and is strongly influenced by thermal balance, current distribution, metal pad behaviour, and the quality of cathode materials. A long cathode age indicates stable operating conditions, low erosion rates, controlled sodium penetration, and effective start-up (which includes preheating), all of which contribute to improved energy efficiency and reduced operational cost.

Conversely, premature cathode failure disrupts production, increases relining frequency, and negatively affects overall smelter performance. Therefore, cathode life serves as a key measure of process robustness and a direct indicator of the success of operational practices and technological improvements in modern prebake cells [26].

Cathode life, commonly measured in days or tonnes of aluminium produced per cathode used, directly influences the economic sustainability and operational reliability of a smelter. A longer cathode age indicates effective thermal balance, stable electrolytic conditions, proper metal pad behaviour, minimal bottom erosion, and well-controlled side ledge profile, all of which contribute to reduced energy consumption and fewer cell disturbances.

Conversely, premature cathode failure—caused by factors such as carbon block erosion, metal penetration, sodium swelling, uneven current distribution, or inadequate preheating—leads to early cell shutdowns, increased relining frequency, and higher maintenance costs [27].

Because the cathode is one of the most expensive components of the reduction cell and dictates the length of each campaign, its service life serves as a key metric for evaluating the success of operational strategies, material selection, and technological upgrades within a smelter. In modern high-amperage prebake cells, achieving a cathode life of 2000 days or more is considered a strong indicator of good cell start-up, optimised cell performance and effective process control [26].

CHAPTER 3

CHARACTERISATION OF THE GRANULAR BLENDS FOR LYING-BEDS

The part of the work presented in this chapter is published in Light Metals 2026-Aluminium Reduction Technology and presented at the conference of TMS 2026 Annual Meeting & Exhibition, San Diego, California, USA. The paper was written in collaboration with Daniel Marceau[1], Duygu Kocaefe[1] and Antoine Godefroy[2]. It was also presented as a poster in the JER 2025, Trois-Rivières, Québec, Canada.

[1] University Research Centre on Aluminium (CURAL) - Aluminium Research Centre (REGAL) - University of Québec at Chicoutimi (UQAC), Chicoutimi, Québec, Canada

[2] Aluminerie Alouette Inc. (AAI), Sept-Îles, Québec, Canada

3.1 General Information

All experimental work in this study was carried out to characterise the properties and behaviour of granular materials–granular calcined petroleum coke and granular graphite as depicted in Figure 3-1, used in lying-bed during cathode preheating. Initially, bulk density and granulometry analyses were performed on the granular coke and graphite materials to establish their fundamental physical characteristics prior to blending. Using these characterised materials, different granular blends were prepared at a fixed mass ratio,

ensuring consistency across all subsequent tests. The physical behaviour of these blends was then investigated through direct shear tests to determine their shear strength parameters and compaction tests to assess their compressibility and packing behaviour under applied loads.

In addition, a dedicated electrical testing setup was designed and developed to measure the electrical properties of the granular blends under various conditions. These combined experimental efforts provide a comprehensive understanding of the physical, and electrical characteristics of the granular blends, forming the basis for subsequent optimisation and modelling work presented in later chapters.

(a) Granular Calcined Petroleum Coke

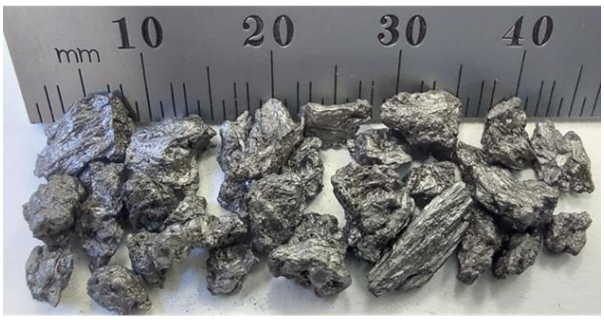

(b) Granular Graphite

Figure 3-1 : Granular calcined petroleum coke and granular graphite

3.2 Characterisation of Physical Properties

3.2.1 Bulk Density

The bulk densities of the granular coke and graphite were determined in the laboratory using a graduated tube to measure the occupied volume and a precision weighing machine to measure the mass. Random samples of each granular material were gently poured into the graduated tube without intentional compaction to ensure reproducible and representative packing conditions. The mass of the sample was recorded, and the corresponding bulk volume was obtained directly from the graduation marks on the tube (Figure 3-2). Bulk density was then calculated as the ratio of mass to bulk volume.

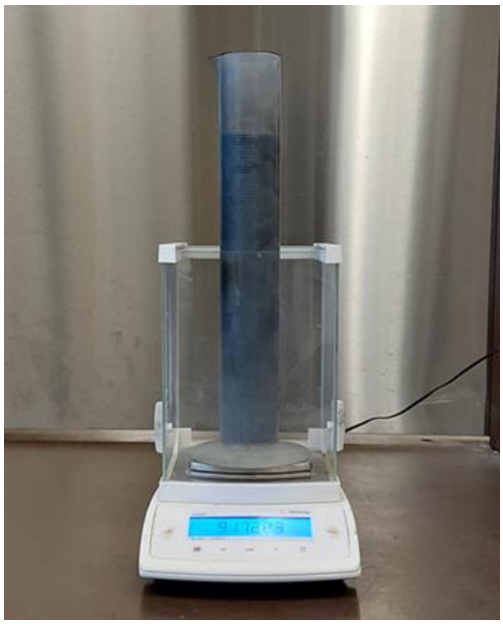

Figure 3-2 : Bulk density determination

To ensure reliability and repeatability of the measurements, the test was performed on randomly selected samples and repeated multiple times for each granular material. The reported bulk density values represent the average of the repeated measurements.

3.2.2 Granulometry

The granulometry of the granular coke and graphite was determined using a RO-TAP sieve shaker (as shown in Figure 3-3), which allows precise separation of particles according to size. Random samples of each granular material were collected to ensure representative analysis. The procedure involved placing a known mass of the sample on the top sieve of a nested set of standard sieves with decreasing mesh sizes. The sieves were then subjected to controlled vibration in the RO-TAP sieve shaker for a specified duration to facilitate particle separation. After sieving, the mass of material retained on each sieve was measured using a precision balance. The particle size distribution was calculated as the percentage of total sample mass retained on each sieve [64][65].

To ensure accuracy and repeatability, the granulometry tests were performed on multiple random samples, and the results were averaged to obtain the final particle size distribution for each granular material.

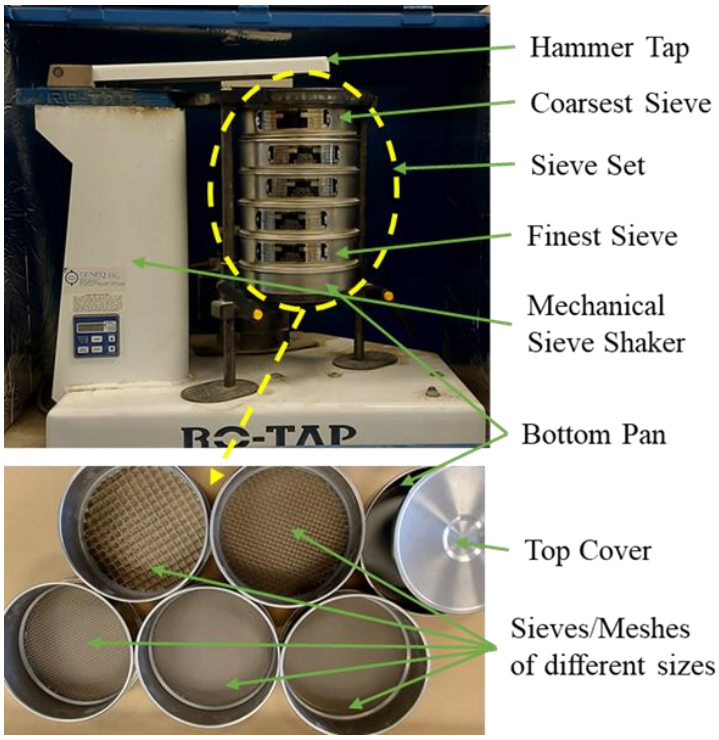

Figure 3-3 : RO-TAP sieve shaker in Geotechnical laboratory, DSA-UQAC

3.2.3 Direct Shear Test

Mohr-Coulomb's Theory

The Mohr–Coulomb theory is widely used to describe the shear strength and failure behaviour of granular materials. According to this theory, failure occurs when the shear stress acting on a plane within a material reaches a critical value that depends linearly on the normal stress acting on that plane. The Mohr–Coulomb failure criterion is expressed as [66]:

$$\tau = C_s + \sigma \tan \phi \qquad \textbf{(3-1)}$$

where, τ = shear stress at failure (Pa), C_s = cohesive strength of the granular material (Pa), σ = normal stress on the failure plane (Pa) and ϕ = angle of internal friction (°).

In the shear stress–normal stress plane, the Mohr–Coulomb criterion is represented by a straight line known as the Mohr-Coulomb failure envelope as represented in Figure 3-4. This envelope defines the limiting combination of shear and normal stresses at which failure occurs.

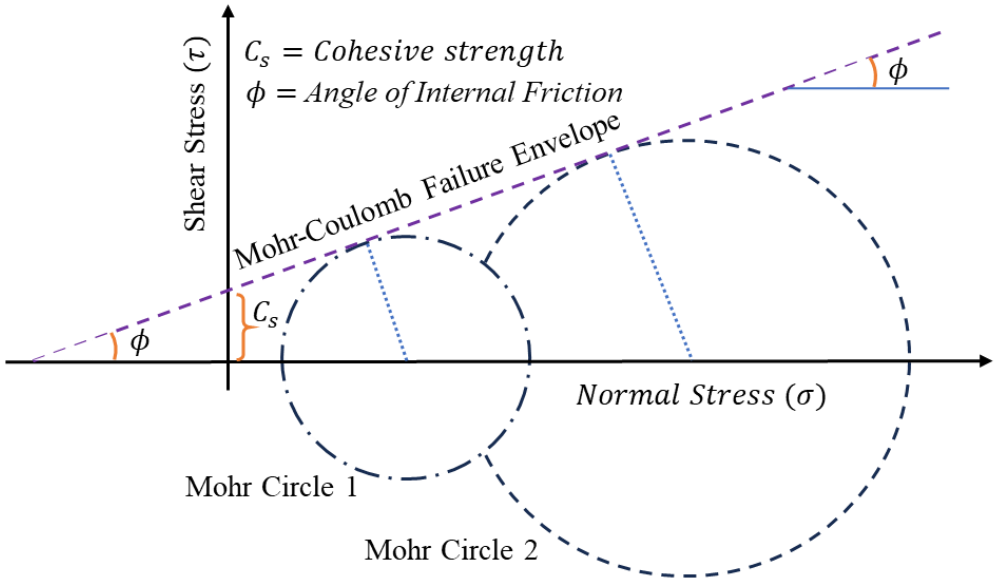

Figure 3-4 : Mohr-Coulomb failure envelope

Each state of stress in the material can be represented by a Mohr circle, constructed using the principal stresses. Failure is predicted when the Mohr circle becomes tangent to the Mohr–Coulomb failure envelope. The point of tangency represents the critical stress condition at failure.

The slope of the failure envelope is given by $\tan\phi$, and its intercept on the shear stress axis corresponds to the cohesive strength of the granular material (C_s). For cohesionless granular materials, such as dry sands, granular coke, or granular graphite, the cohesive strength is often negligible, and the Mohr-Coulomb failure criterion simplifies to:

$$\tau = \sigma \tan\phi \qquad \textbf{(3-2)}$$

The angle of internal friction (ϕ) is a fundamental material parameter that characterises the resistance to shear deformation arising from inter-particle friction, particle interlocking and surface roughness during shear. A higher value of ϕ indicates greater shear strength and stability of the granular material.

Physically, the angle of internal friction represents the inclination of the failure plane with respect to the principal stress direction at the point of failure. It is closely related to the material's packing density, particle shape, size distribution, and applied normal stress. In experimental practice, ϕ is commonly determined from direct shear tests or triaxial compression tests by plotting the measured shear stress at failure against the corresponding normal stress and fitting a linear failure envelope [67].

The shear strength of the granular blends was evaluated using a direct shear test apparatus as shown in Figure 3-5. In this method, a known mass of the granular material was placed in a shear box, which is designed to allow horizontal movement of the lower half relative to the upper half. A normal load was applied vertically to the sample to simulate the confining pressure, and the shear force was gradually applied by moving one half of the shear box while keeping the other half fixed as illustrated in Figure 3-6. The corresponding shear load at which the material fails or shears was measured using a load scale attached to the apparatus. Figure 3-6 depicts the schematic representation of the direct shear test.

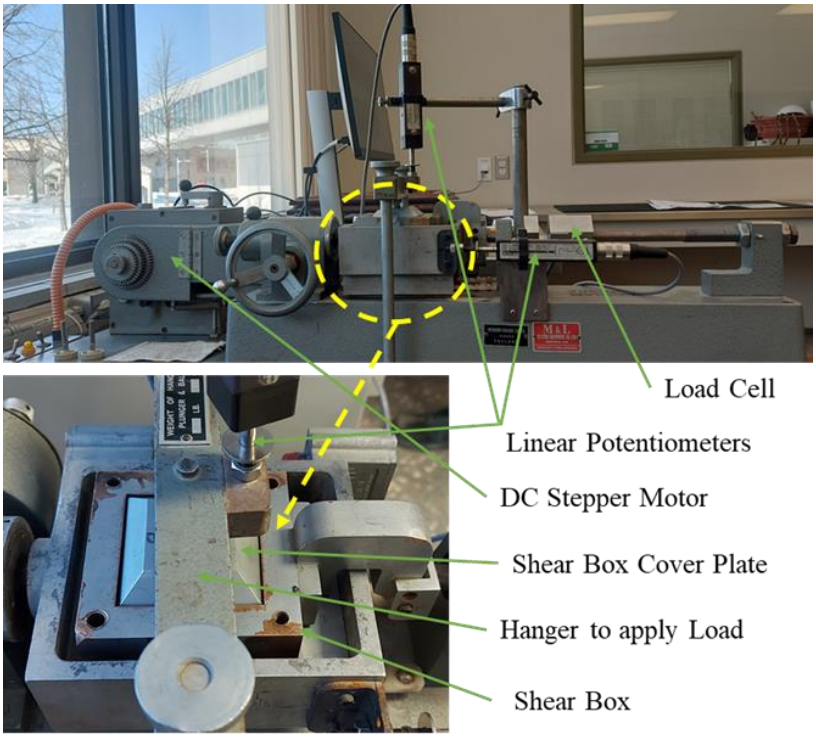

Figure 3-5 : Direct shear test apparatus in Geotechnical laboratory, DSA-UQAC

This procedure was repeated for various granular blends under different applied normal loads to determine their shear strength characteristics. The measured shear and normal stresses were then used to evaluate the material parameters such as the angle of internal friction (ϕ) which is the angle of repose (θ_r) for the cohesionless granular materials.

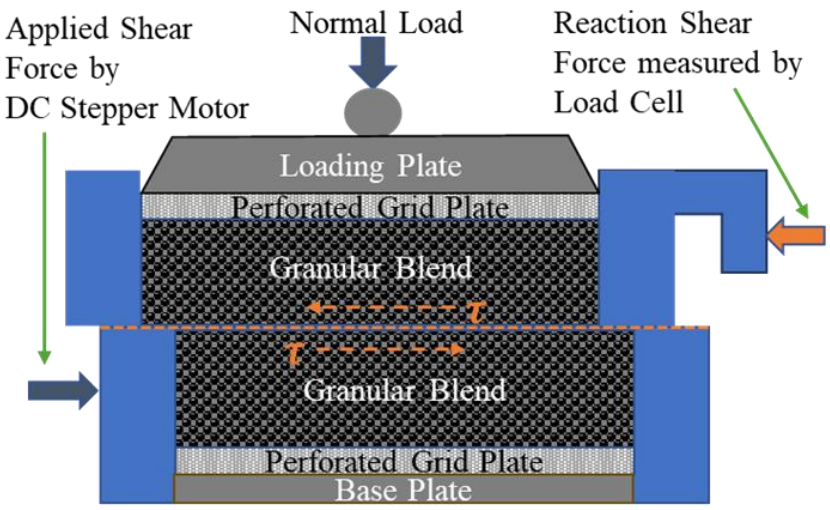

Figure 3-6 : Schematic representation of the direct shear test

3.2.4 Compaction Test

The compaction behavior of the granular blends was evaluated using various cylindrical moulds of known diameters and heights. The granular blend was poured into the mould which gave a known height as shown in Figure 3-7(a). Then the mould was carefully lifted vertically, allowing the material to flow naturally (due to flowability property of granular materials) and form a frustum-shaped (truncated cone) structure as illustrated in Figure 3-7(b). The initial height and top diameter of the truncated cone were recorded as

shown in Figure 3-7(c) and Figure 3-7(d) respectively. A known load was then applied to the material as shown in Figure 3-7(e), and after removal of the load, the height and top diameter were measured again as depicted in Figure 3-7(c) and Figure 3-7(d) respectively. This process was repeated in cycles with increasing applied loads for a single granular blend to study how the granular material gets compressed.

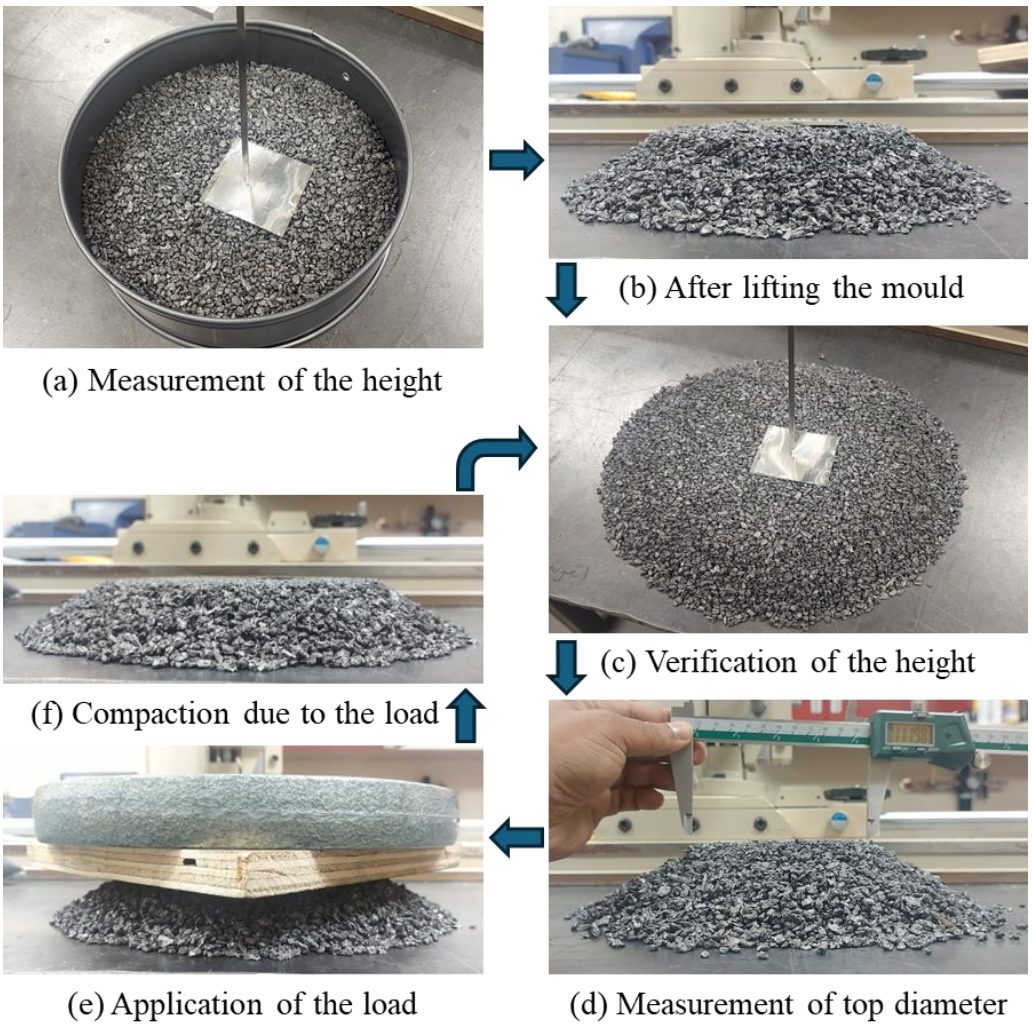

Figure 3-7 : Compaction test procedure

Figure 3-7 summarises the complete procedure of the compaction test. The test was performed for different granular blends using moulds of varying diameters and heights to evaluate the effect of loads and blend composition on compaction behavior. The changes in height and top diameter (top surface area) of the truncated cone after applying each load in increasing order were used to understand the compaction behavior of the granular blends.

3.3 Characterisation of Electrical Properties

3.3.1 Principles

Ohm's Law of Electrical Conduction

Ohm's law describes the fundamental relationship between the electric current flowing through a conductor and the applied potential difference across it. When a conductor is maintained at constant temperature and physical conditions, the current, I flowing through the material is directly proportional to the applied voltage, V. This relationship is expressed as:

$$V = RI \qquad \textbf{(3-3)}$$

where R is the electrical resistance (Ω) of the material. Ohm's law forms the basis for determining electrical resistance from experimentally measured current–voltage

characteristics as shown in Figure 3-8 and is valid provided the material exhibits linear, ohmic behavior.

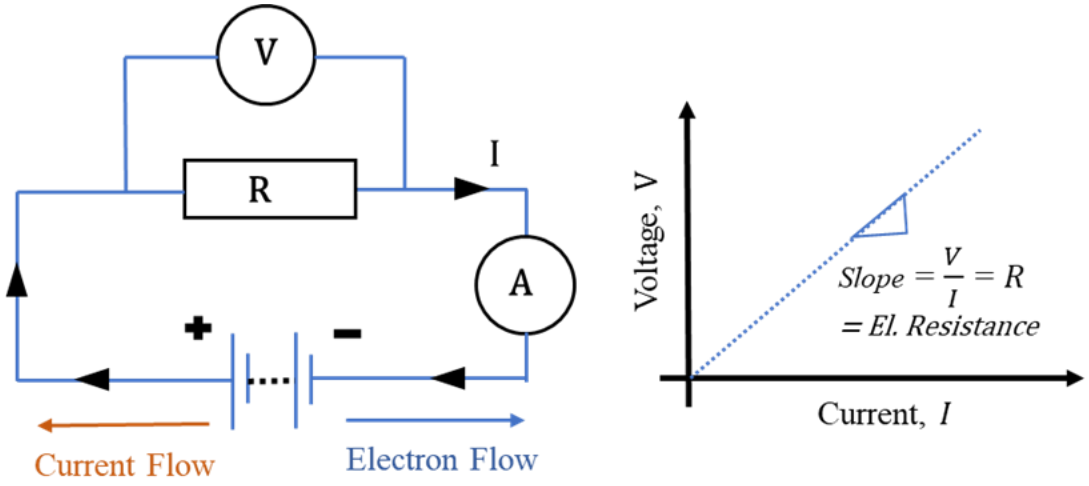

Figure 3-8 : Ohm's law representation

Electrical Resistivity of Materials

Electrical resistivity (or specific electrical resistance) is an intrinsic property of a material that describes its opposition to the flow of electric current. When an electric potential difference is applied across a material, the resulting current is governed by Ohm's law. The electrical resistance, R of a specimen depends on its geometry and material properties, and is defined as:

$$R = \rho \frac{L}{S} \qquad \textbf{(3-4)}$$

where ρ is the electrical resistivity (Ω·m), R is the measured electrical resistance (Ω), S is the cross-sectional area (m^2), and L is the length of the current path (m) as depicted in Figure 3-9.

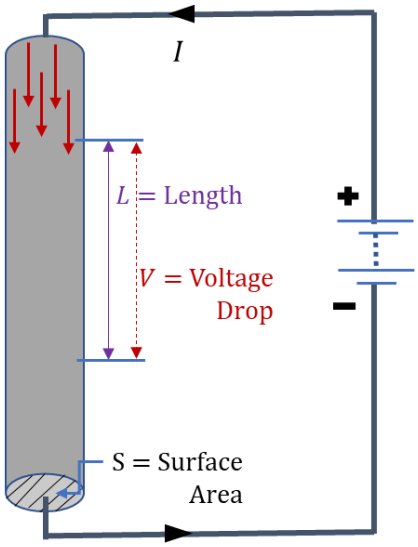

Figure 3-9 : Electrical resistivity measurement

Substituting the expression for resistance into Ohm's law yields:

$$V = \left(\rho \frac{L}{S}\right) I \qquad \textbf{(3-5)}$$

Rearranging the Equation (3-5) gives the expression for electrical resistivity:

$$\rho = \frac{V}{I} \frac{S}{L} \qquad \textbf{(3-6)}$$

Equation (3-6) forms the basis for the experimental determination of electrical resistivity from measured voltage and current values for a specimen of known dimensions.

Electrical resistivity is strongly influenced by temperature. Over a limited temperature range, this dependence can be approximated by a linear relationship [68]:

$$\rho_2 = \rho_1[\,1 + \alpha_T(T_2 - T_1)\,] \qquad (3\text{-}7)$$

where ρ_1 and ρ_2 are the electrical resistivities at corresponding temperatures, T_1 and T_2 respectively, and α_T ($°C^{-1}$) is the temperature coefficient of electrical resistivity.

Mechanical pressure also plays a significant role in determining electrical resistivity, particularly in porous and granular materials. The application of pressure improves particle-to-particle contact, reduces contact resistance, and decreases void spaces within the material. As a result, the effective electrical resistivity generally decreases with increasing pressure. In such systems, the overall resistivity is governed by both the intrinsic resistivity of the solid phase and the resistance at inter-particle contacts.

Therefore, the electrical resistivity of materials, especially granular and carbon-based systems, is a combined function of temperature, applied pressure, and material microstructure or composition. Understanding these dependencies is essential for

accurately characterising electrical behavior under conditions relevant to industrial electrochemical processes.

Specific Electrical Contact Resistivity

When electric current flows across the interface between two contacting conductive bodies (Figure 3-10), an additional resistance known as electrical contact resistance arises due to the imperfect nature of real contact surfaces. At the microscopic level, contact occurs only at discrete asperities, resulting in a reduced real contact area and constriction of current flow. The electrical contact resistance, R_c is defined as:

$$R_c = \frac{V_c}{I} \tag{3-8}$$

where V_c (V) is the voltage drop across the contact interface and I (A) is the electric current.

To normalise the contact resistance with respect to the contact area, the specific electrical contact resistivity ρ_c is introduced and defined as:

$$\rho_c = R_c S_c \tag{3-9}$$

where S_c (m^2) is the common contact surface area and ρ_c has units of $\Omega \cdot m^2$. This parameter enables comparison of interfacial electrical behavior independent of contact geometry.

The voltage drop across the contact interface is given by:

$$V_c = V_{up} - V_{down} \qquad \textbf{(3-10)}$$

where V_{up} and V_{down} are the voltage drops across the contact interface (by extrapolation).

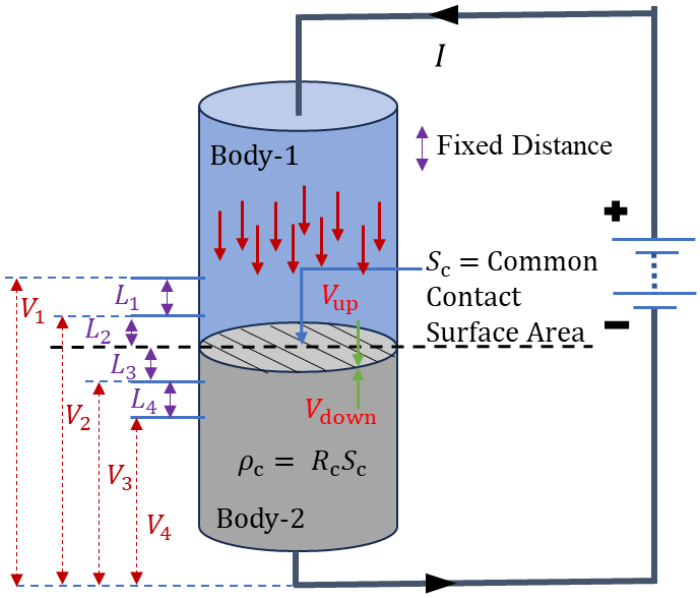

Figure 3-10 : Specific electrical contact resistivity measurement

Substituting this expression in Equation (3-8) we get,

$$R_c = \frac{V_{up} - V_{down}}{I} \quad \textbf{(3-11)}$$

Again, substituting the above expression in Equation (3-9) in we get,

$$\rho_c = \left(\frac{V_{up} - V_{down}}{I}\right) S_c \quad \textbf{(3-12)}$$

where V_{up} and V_{down} are given by the following expressions:

$$V_{up} = V_2 - \left(\frac{V_1 - V_2}{L_1}\right) L_2 \quad \textbf{(3-13)}$$

and

$$V_{down} = V_3 + \left(\frac{V_3 - V_4}{L_4}\right) L_3 \quad \textbf{(3-14)}$$

These above equations (Equation (3-12), Equation (3-13) and Equation (3-14)) form the basis for evaluating specific electrical contact resistivity from four-point voltage drop measurements as illustrated in Figure 3-10, providing a reliable characterisation of interfacial electrical behavior independent of bulk and lead resistances [69][70].

Temperature has a significant influence on specific electrical contact resistivity. An increase in temperature generally leads to higher resistivity due to enhanced electron–phonon scattering within the contacting materials. Additionally, temperature variations can alter surface films such as oxides or adsorbed species at the contact interface, further affecting contact resistance. At elevated temperatures, softening of contact asperities may occur, which can partially offset the increase in resistivity by increasing the real contact area.

Applied mechanical pressure plays a crucial role in determining specific electrical contact resistivity especially for the granular materials. Increasing contact pressure enlarges the real area of contact by deforming surface asperities and improving interfacial conformity. This reduces constriction resistance at the contact points and leads to a decrease in contact resistivity. In granular or particulate systems, pressure enhances the number and quality of inter-particle contacts, significantly lowering the overall electrical resistance of the contact network [71].

Therefore, electrical contact resistivity is a function of both temperature and pressure, as well as surface roughness, material hardness, and interfacial conditions. Understanding these dependencies is essential for accurately characterising electrical performance in systems where current transfer occurs across interfaces, such as granular beds and electrode assemblies.

3.3.2 Experimental Setup Development

A new experimental setup was developed in the GRIPS laboratory of CURAL-UQAC to measure the electrical properties of granular materials as shown in Figure 3-11. The setup consists of an alumina tube surrounded by a steel tube, in which the granular material is placed. Several perforations are made at known, fixed distances along the tube to allow measurement of electrical voltage drops. A DC current source is connected to electrodes at both ends of the tube to pass an electrical current through the granular material. To apply pressure on the sample, a class 3 lever system is installed, allowing controlled loading and monitored by a load cell on top of the tube. Electrical wires were installed to record voltage drops at different points along the tube and the current in the circuit continuously and simultaneously using a KEITHLEY^{TM} (2700 Series) data acquisition system and ExceLINX^{TM} software.

The schematic of the setup shows that the tube contains industrial-grade anode/cathode granular material. Electrodes at both ends allowed to pass the current through the sample, while two N-type thermocouples were installed for temperature monitoring. One thermocouple measured the contact surface temperature (T_{cs}), while the other is placed in the granular material to monitor its average granular temperature (T_g). This arrangement ensured simultaneous measurement of electrical properties under controlled pressure conditions. The schematic diagram of the developed electrical setup is illustrated in Figure 3-12.

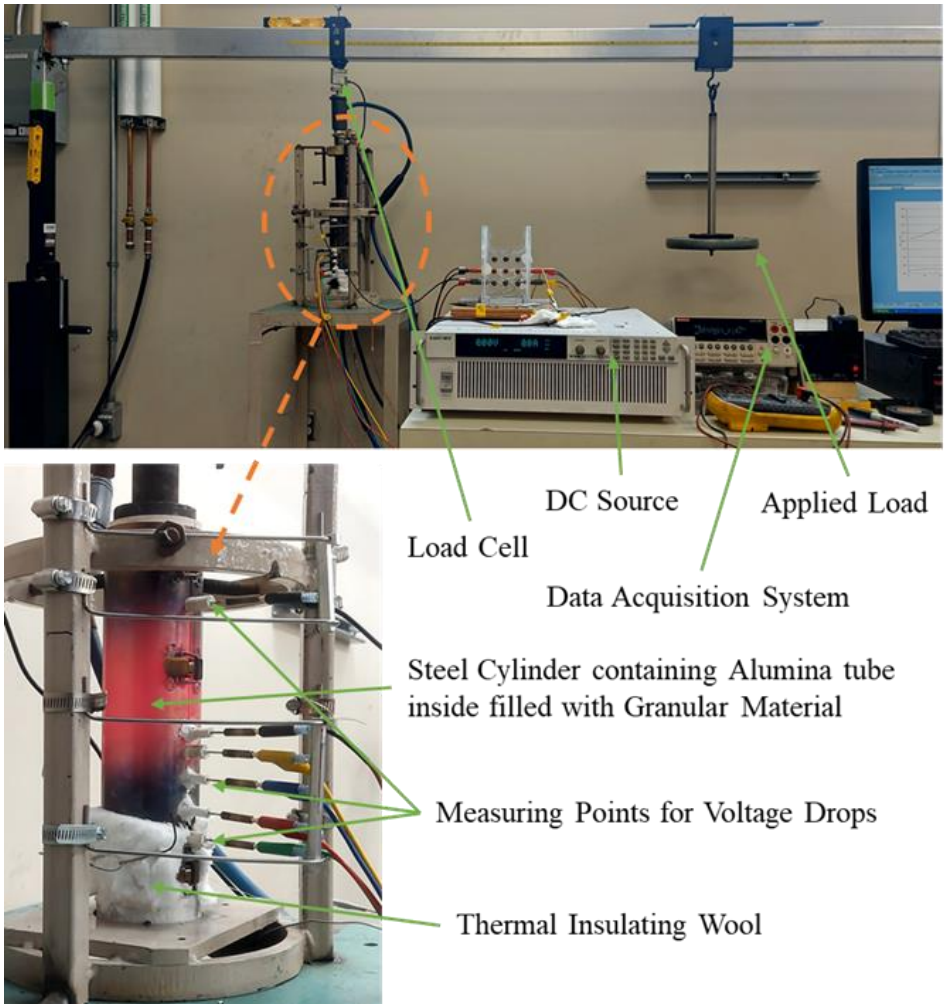

Figure 3-11 : Experimental setup in GRIPS laboratory, CURAL-UQAC

The electrical resistivity of the granular material is calculated form the granular voltage drop (V_g) and its associated length (L_g) as shown in Figure 3-12. The specific electrical contact resistance (SECR) between granular material and anode/cathode is computed from the four other voltage drops (V_1, V_2, V_3 *and* V_4) and fixed lengths (L_1, L_2, L_3 *and* L_4) associated with them by the extrapolation.

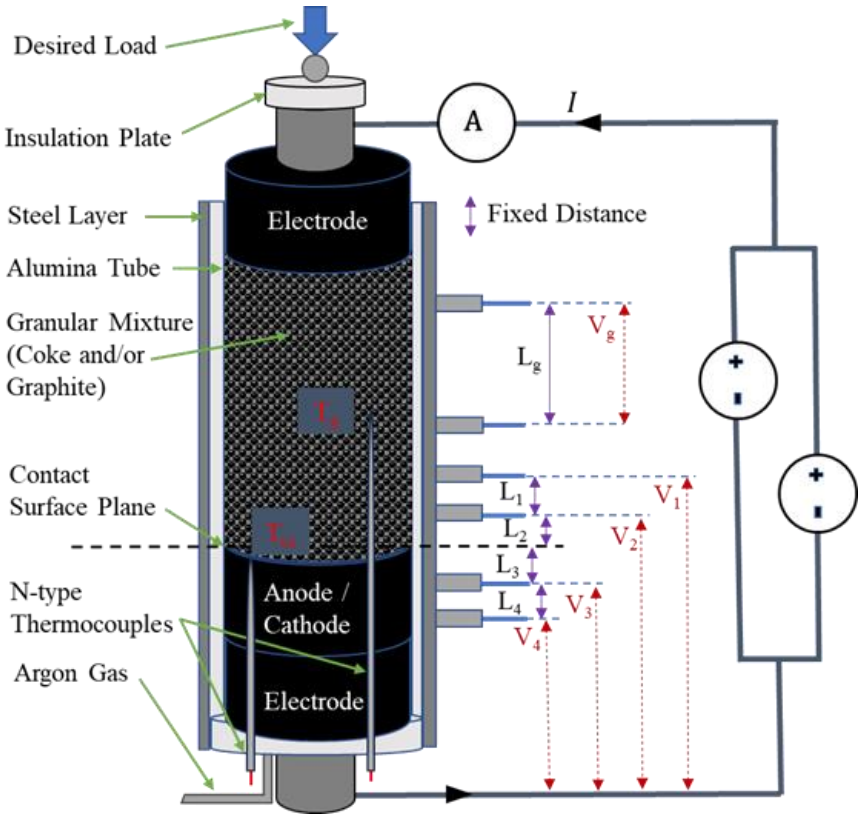

Figure 3-12 : Schematic diagram of the electrical experiment

3.3.3 Calibrations

Prior to the experiments, the load cell and the DC sources used in the setup were calibrated. These calibrations ensure that both the applied mechanical load and the electrical current are accurate and consistent throughout the experiments.

Load Cell Calibration

The load cell used in the class 3 lever system was calibrated by applying known standard loads and recording the corresponding readings to establish a reliable load–output relationship. The DC power supply (12.22 V) to the load cell is kept constant by adding

a voltage stabiliser, as its variations influence the load-output signal. The calibration curve for the load cell is given by Figure 3-13.

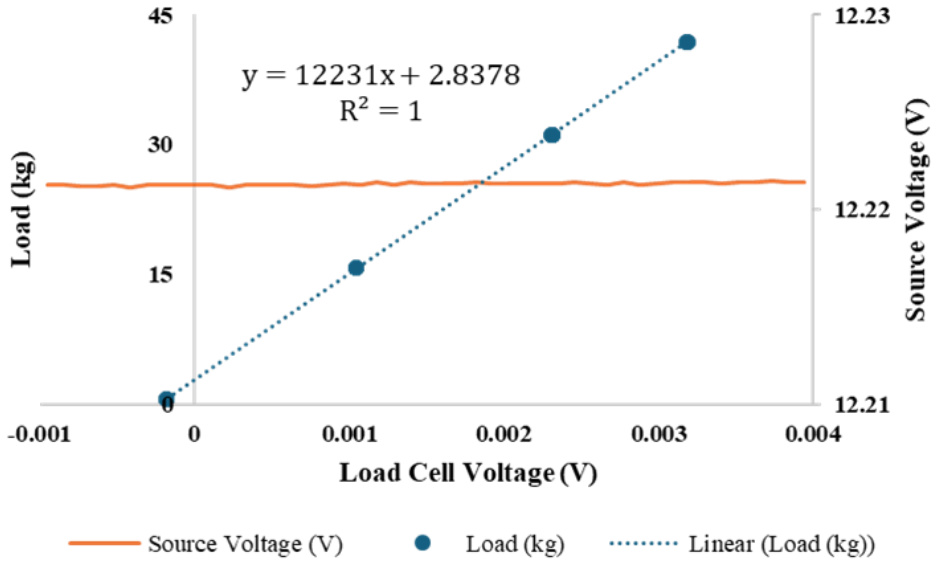

Figure 3-13 : Calibration curve for the load cell

DC Sources Calibration

The DC current sources were calibrated to verify that the applied current matched the set values. Two DC sources are used in all the experiments: DC source-1 (300 A and 20 V) and DC source-2 (500 A and 40 V) which is a parallel combination of 2 DC sources each of 250 A and 40 V. The calibration curves for the DC sources used in the experiments are given by the Figure 3-14 and Figure 3-15 respectively.

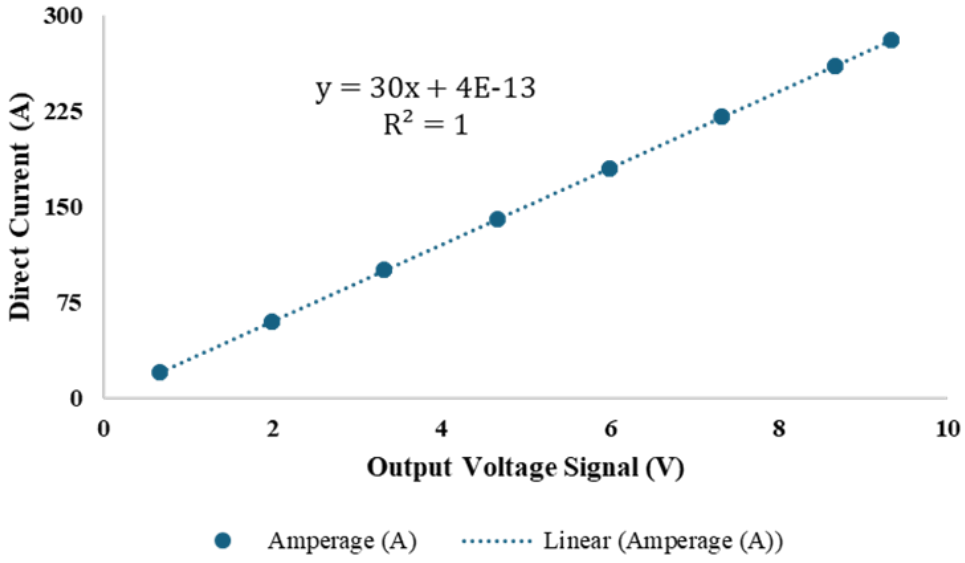

Figure 3-14 : Calibration curve for the DC source-1

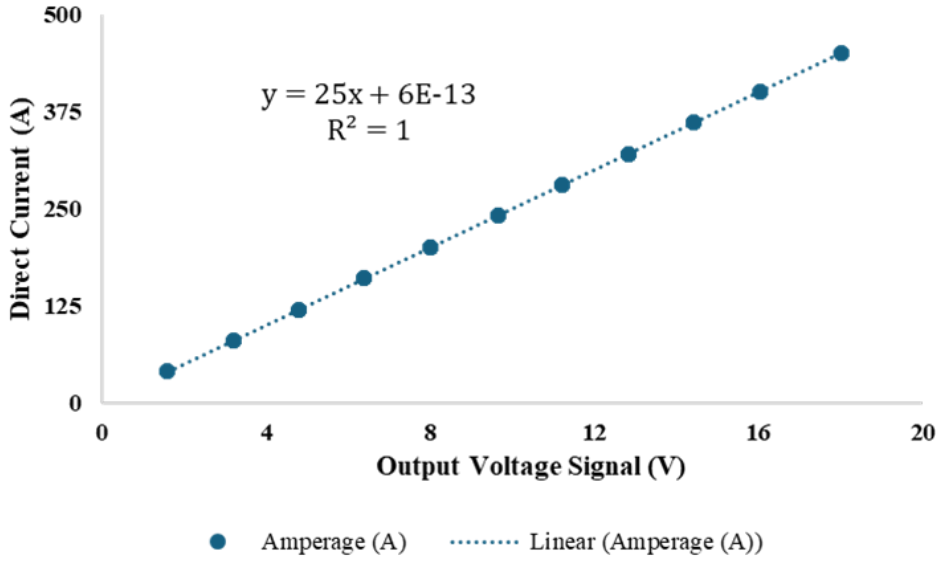

Figure 3-15 : Calibration curve for the DC source-2

3.3.4 Experimental Procedure

The granular material was carefully poured into the alumina-steel tube to ensure uniform filling without segregation or compaction bias. A known mechanical load was then applied to the sample using the class 3 lever system, and the system was allowed to stabilise for a period. A direct current (DC) was passed through the sample via electrodes positioned at both ends of the tube. Electrical voltage drops at various perforated positions along the tube, as well as the overall current, were measured simultaneously using the KEITHLEY™ data acquisition system and continuously recorded in ExceLINX™ software.

Temperatures were monitored during the experiment using two N-type thermocouples: one measuring the contact surface temperature and the other positioned within the granular material to record its average temperature. The temperature of the granular material was gradually increased by incrementally increasing the DC current in controlled steps. This stepwise heating continued until the average granular material temperature reached approximately 1000 °C. At each step, voltage drops, current, and temperatures were recorded to study the electrical and thermal response of the granular blend under controlled pressure and high-temperature conditions.

This test was performed for different granular blends (coke content: 0–100%) under various applied pressures up to 500 kPa, first using the anode (*APPENDIX 1 : Electrical Test Experiment Plan*). Later, the same experiments were repeated using the cathode. It

is noteworthy to mention that the pressure limit is chosen by considering the possibilities of the least total surface area of the pucks in the lying-bed under the maximum load of one anode covered with ACM.

3.4 Results Analysis and Discussion

3.4.1 Physical Properties

Bulk Density

The bulk densities of the granular coke and graphite were determined. The values were found to be 690 kg/m^3 and 822 kg/m^3 for coke and graphite respectively.

Particle Size Distribution

The mass retained on each sieve was recorded (as listed in Table 3-1) and used to calculate the cumulative percentage passing. These data were used to construct the particle size distribution (PSD) curve as given in Figure 3-16. Several granulometric parameters like fineness modulus, coefficient of uniformity and coefficient of curvature were computed from the PSD curve, which helps in understanding the physical properties of the granular materials.

Fineness Modulus

The fineness modulus (FM) represents the average particle size of the granular material. A higher FM indicates coarser particles. Here, the calculated fineness moduli for the granular coke and graphite are 2.90 and 2.60 respectively.

Table 3-1 : Retained granular mass according to particle size

Particle Size Range (mm)	Mass of Coke (%)	Mass of Graphite (%)
More than and Equal to 10	0.0	0.0
Between 5 to 10	10.7	0.0
Between 2.5 to 5	72.0	61.4
Between 1.25 to 2.5	16.9	37.7
Between 0.63 to 1.25	0.2	0.3
Less than 0.63 (dust in the pan)	0.1	0.6

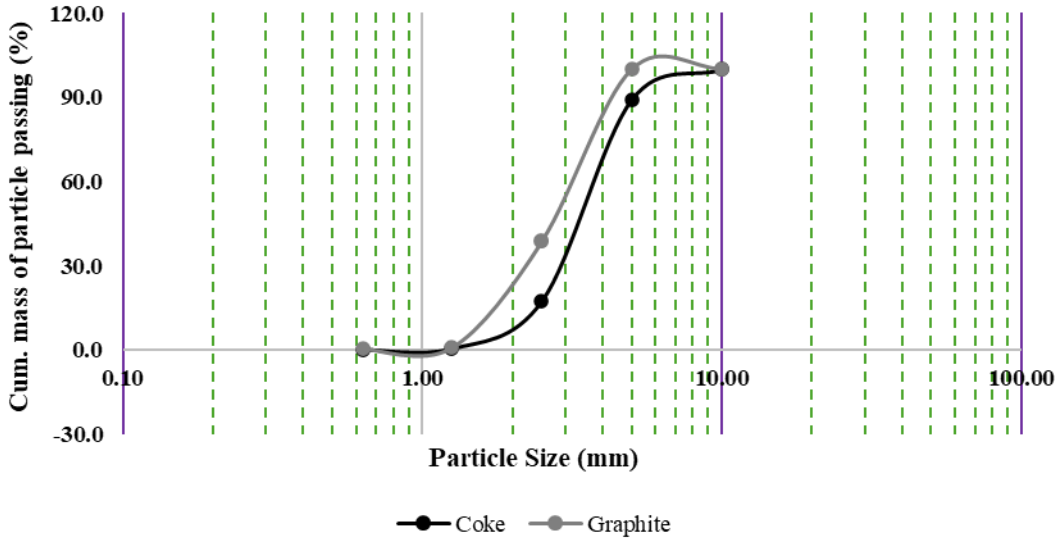

Figure 3-16 : Particle size distribution curves of granular coke and graphite

Coefficient of Uniformity

The coefficient of uniformity (C_u) was found to be 1.70 and 1.94 respectively for the granular coke and graphite. It provides a measure of the particle size spread. A higher C_u implies a more well-graded material, *i.e.*, a good mix of particle sizes in the material.

Although the difference is moderate; both materials are still relatively poorly graded (uniform) as $C_u < 3$.

Coefficient of Curvature

The coefficient of curvature (C_c), calculated , was 1.02 for the granular coke whereas 0.92 for the granular graphite. This value indicates the shape of the PSD curve and helps classify the gradation quality. Values between 1 and 3 typically suggest well-graded materials. Here, the difference is very subtle.

Considering both the coefficient of uniformity and coefficient of curvature together, we may conclude that both the granular coke and graphite materials are poorly graded (*i.e.* uniformly graded). The subtle difference coefficient of curvature indicates minor variation in the particle proportion, but overall grading is uniform. Together, with the bulk density these granulometric indices define the structural nature of the granular coke and graphite which are listed in Table 3-2 [72].

Table 3-2 : Physical properties of the granular coke and graphite

Physical properties	Coke	Graphite	Comparison
Bulk density (kg/m^3)	690	822	Coke is relatively lighter
Fineness Modulus (FM)	2.90	2.60	Coke is relatively coarser
Coefficient of uniformity (C_u)	1.70	1.94	Both are poorly/uniformly graded
Coefficient of curvature (C_c)	1.02	0.92	

Angle of Repose

As expected for the cohesionless granular materials, the shear strength was primarily governed by interparticle friction. The peak shear stress for each granular blend and different normal stresses was identified from shear stress-horizontal displacement graph as shown in Figure 3-17. These peak shear stress values corresponding to the normal stresses were plotted to develop the Mohr-Coulomb failure envelopes for different granular blends (of different mass ratio of granular coke and graphite) as illustrated in Figure 3-18.

For each granular blend, the angle of internal friction is calculated from the corresponding Mohr-Coulomb failure envelope, a key parameter indicating the material's resistance to sliding. The slope of the Mohr-Coulomb failure envelope gives the angle of internal friction. As they are cohesionless granular materials, the Mohr-Coulomb failure envelopes pass through the origin (Figure 3-18) and the angle of repose (θ_r) is approximately the same as the angle of internal friction (ϕ) [66].

In Figure 3-18, it can be seen that the slopes of the Mohr-Coulomb failure envelopes of the two granular blends (C30G70 and C70G30) are very close to each other. Hence, they are superposed on each other.

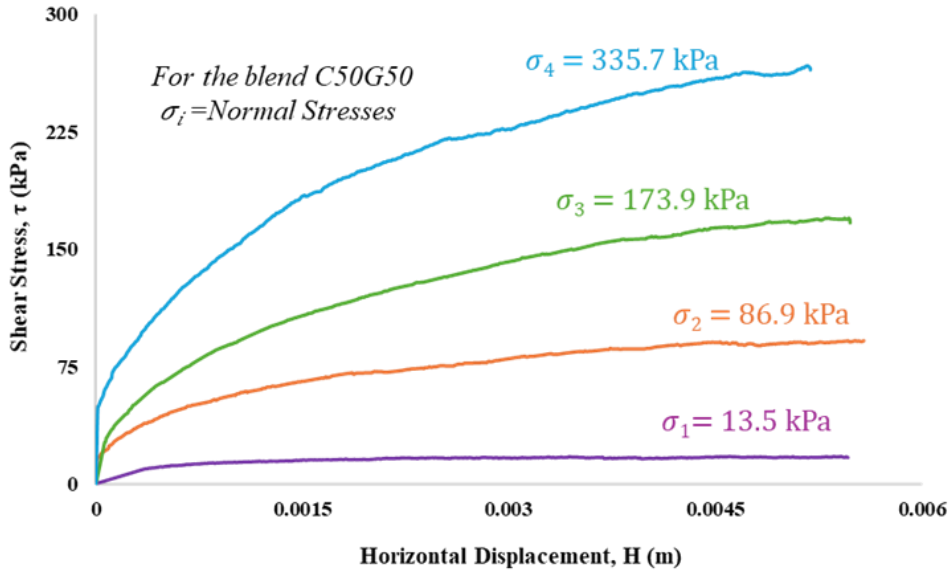

Figure 3-17 : Shear stress-horizontal displacement curves

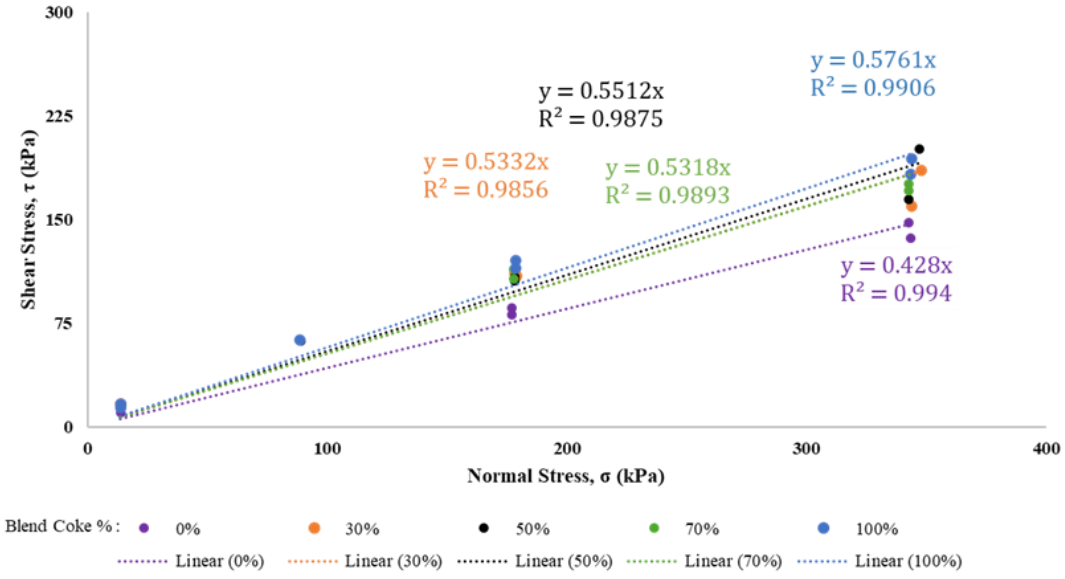

Figure 3-18 : Mohr-Coulomb failure envelopes for various granular blends

Table 3-3 shows all details concerning the angle of repose and angle of internal friction for various granular blends and plotted in Figure 3-19 to show the relationship with the blend coke content. It can be said that the angle of repose, θ_r (°) of the blend varies linearly with the fractional blend coke content.

The angle of repose is found to be the lowest for the 100% graphite material (G100) whereas it is highest for the 100% coke content (C100). The blends of coke and graphite show values which stay in between the above two extremes. Hence, the shape of the puck is different for different blends, and it is more truncated in case of G100 as compared to C100. These values will determine the shape of the puck before the application of the load.

Table 3-3 : Angle of internal friction and angle of repose

Granular Blend (by mass ratio)	**Acronym**	**Angle of Internal Friction, ϕ & Angle of Repose, θ_r (°)**
Coke 100%	C100	29.95
Coke 70% + Graphite 30%	C70G30	28.00
Coke 50% + Graphite 50%	C50G50	28.86
Coke 30% + Graphite 70%	C30G70	28.07
Graphite 100%	G100	23.17

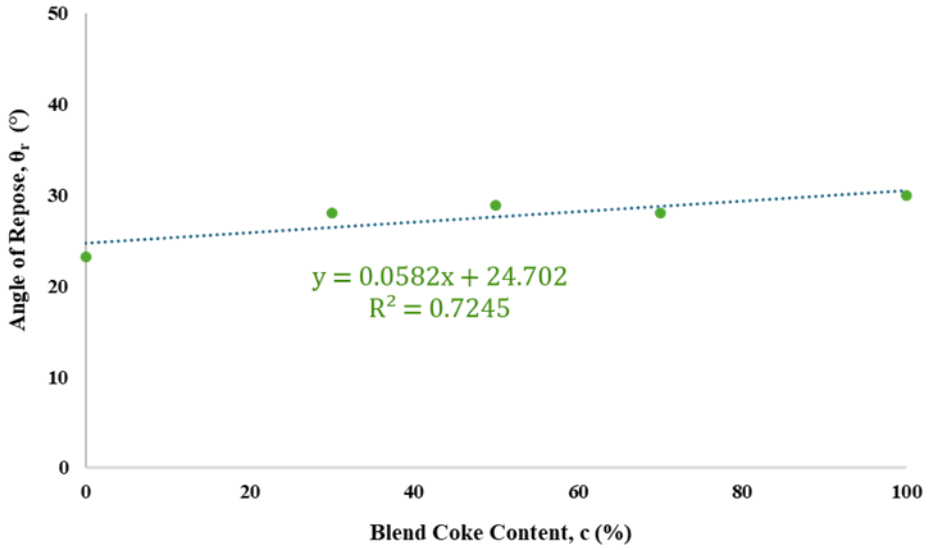

Figure 3-19 : Relationship between angle of repose and blend coke content

Axial Strain

For the compaction test of the granular materials which gives large deformations, the measurement of the axial change in height, $H(p)$ with the applied pressure allows for the calculation of the true axial strain (ε_a) using the following expression:

$$\varepsilon_a(p) = \ln\left(\frac{H(p)}{H_i}\right) \qquad \textbf{(3-15)}$$

where H_i and H are the measured sample heights before and after applying a given pressure (p) respectively.

Due to the large deformations (anticipated and observed) for such non-cohesive granular materials, the true axial strain is considered which is different from the axial strain within the elastic limit for small deformations.

The relationship between the true applied pressure (p - kPa) and the axial strain (ε_a - unitless) can be expressed using the Voce's law such that:

$$\varepsilon_a(c,r,p) = -\varepsilon_0(c,r)\left(1 - e^{-A(c,r)p}\right) \quad \textbf{(3-16)}$$

where, ε_0 $(-)$ and A (kPa^{-1}) are two parameters which are function of the blend coke content (c) and the sample shape ratio (r) defined as:

$$r = \frac{H_0}{D_0} \quad \textbf{(3-17)}$$

with H_0 and D_0, the initial height and diameter of the sample while constructing by the mould, respectively.

Considering the experimental data, the tendency of ε_0 and A is expressed as:

$$\varepsilon_0(c,r) = e_0\,(c) + \ e_1\,(c)r$$
$$A(c,r) = a_0(c)e^{a_1(c)r} \quad \textbf{(3-18)}$$

where, e_0 $(-)$, e_1 $(-)$, a_0 (kPa^{-1}) and a_1 $(-)$ are fine calibration parameters which are function of the blend coke content (c) only.

Equation (3-18) is solved using GRG (Generalized Reduced Gradient) nonlinear solver on the experimental data.

Originally used to express the stress-strain curve with hardening, Voce's law is also well suite to express the axial strain saturation with the applied pressure. From the axial deformation data, corresponding axial strains and pressures are calculated and plotted in Figure 3-20. The experimental data are obeying the strain hardening curve of Voce's law. This means the fast rise of axial strain for lower initial stresses and then saturates afterwards.

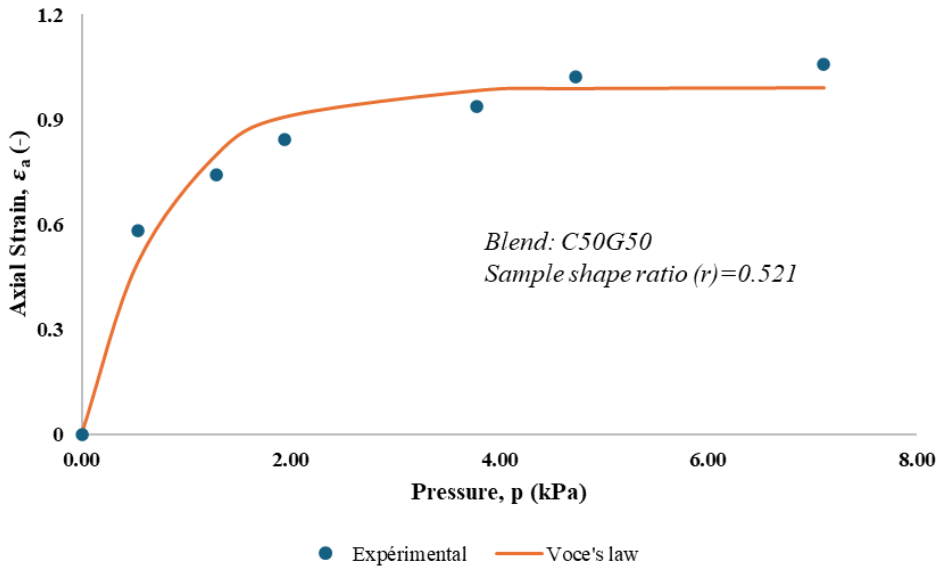

Figure 3-20 : Axial strain (Experiment vs Model)

Figure 3-21 shows the experimental data are represented by the model developed by the Voce's law for different sample shape ratios and blend coke contents. More specifically, results show that axial strain increases with the sample shape ratio, which gives more than 100 % for $r = 0.521$ and saturation occurs at lower pressure. Also, the results show that for similar sample shape ratio ($r = 0.155$, 0.138 and 0.137), the impact of the blend coke content remains very low. The obtained results exhibit a strong dependency on the sample shape ratio (r) which varies from 0.137 to 0.521 and a weak dependency to the coke content which vary from 0% to 100% [72].

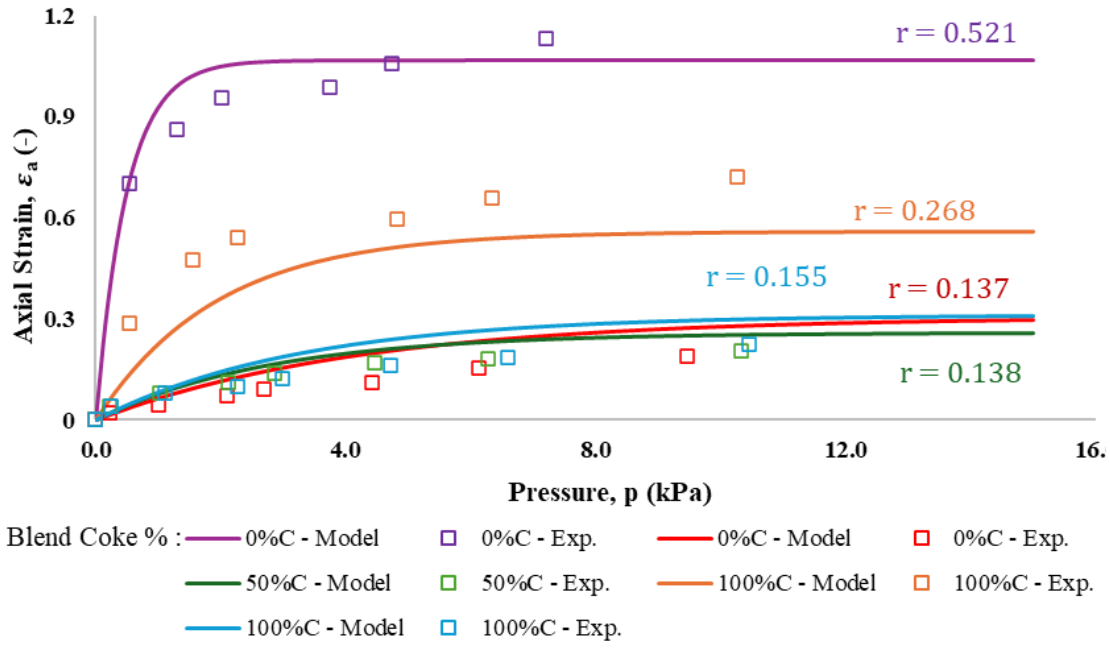

Figure 3-21 : Axial strain for various blends with different sample shape ratio (r)

Figure 3-22 and Figure 3-23 show the evolution of the parameters of $\varepsilon_0(c,r)$ and $A(c,r)$ with respect to sample shape ratio (r). Figure 3-24 and Figure 3-25 show the evolution of the fine calibration of the parameters of $\varepsilon_0(c,r)$ and $A(c,r)$.

$$e_0(c) = e_{00}^* + e_{01}^* c + e_{02}^* c^2$$

$$e_1(c) = e_{10}^* + e_{11}^* c + e_{12}^* c^2$$

$$a_0(c) = a_{00}^* + a_{01}^* c + a_{02}^* c^2 \quad \textbf{(3-19)}$$

$$a_1(c) = a_{10}^* + a_{11}^* c + a_{12}^* c^2$$

All the fine calibration parameters are unitless except a_{00}^* (kPa^{-1}), a_{01}^* (kPa^{-1}) and a_{02}^* (kPa^{-1}). They allow accurate representation of the impact of blend coke content. Thus, the experimental data are well represented by the model.

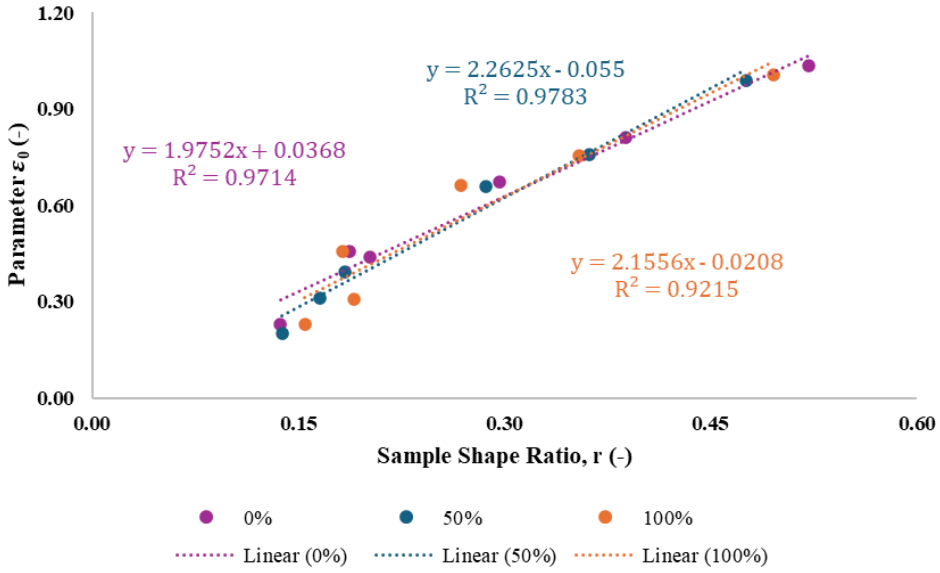

Figure 3-22 : Evolution of the parameter, ε_0 with sample shape ratio (r)

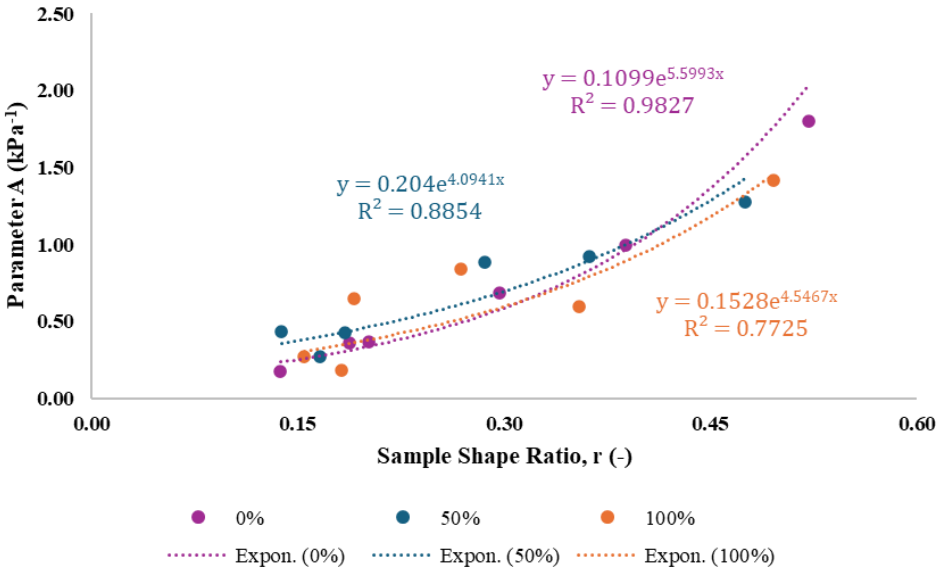

Figure 3-23 : Evolution of the parameter, A with sample shape ratio (r)

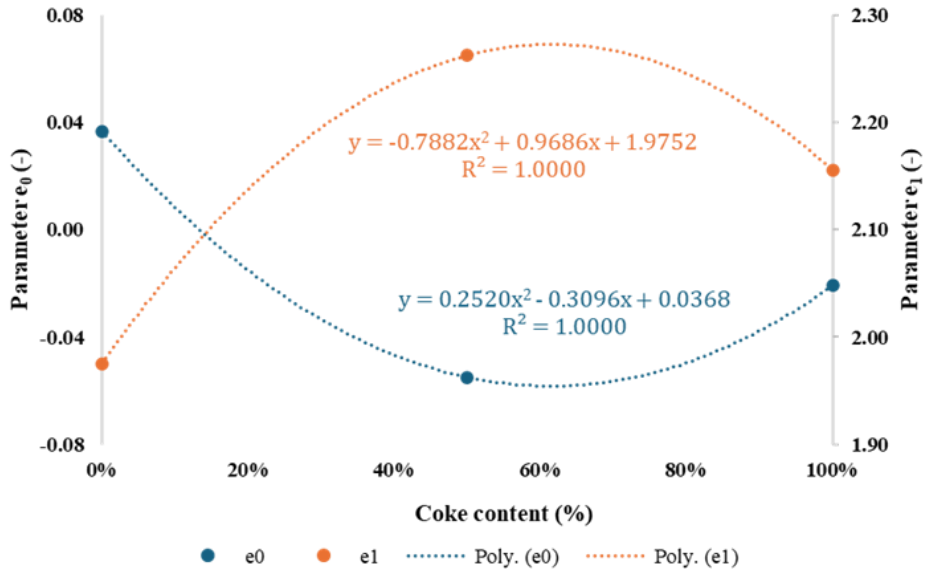

Figure 3-24 : Evolution of the parameters, e_0 and e_1 with blend coke content

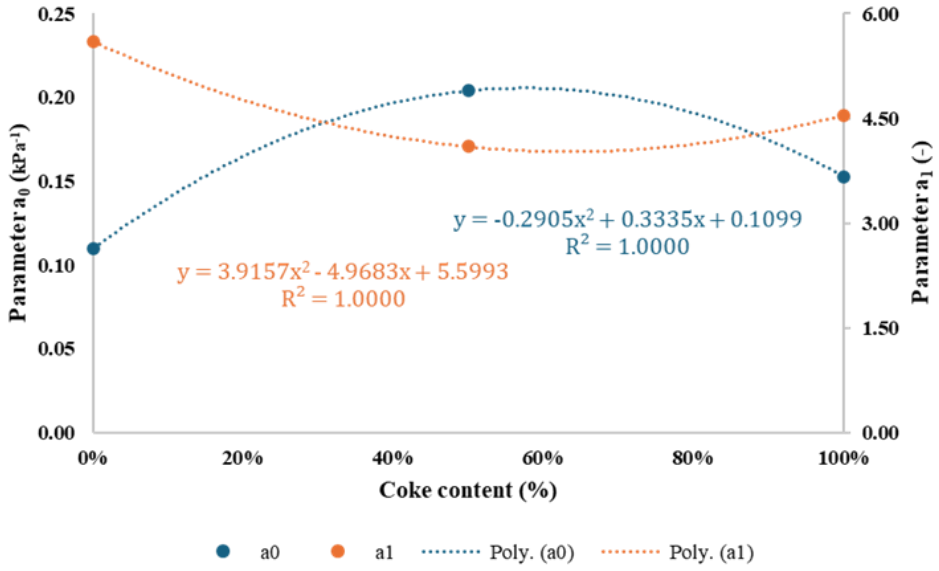

Figure 3-25 : Evolution of the parameters, a_0 and a_1 with blend coke content

Diametral Strain

Evolution of the true diametral strain (ε_d) with the pressure is a crucial information to determine the final diameter of the sample and can be calculated using the change in the diameter such that:

$$\varepsilon_d(p) = \ln\left(\frac{D(p)}{D_i}\right) \qquad \textbf{(3-20)}$$

where D_i and $D(p)$ are the measured sample diameters before and after applying a given pressure (p) respectively.

Due to the large deformations (anticipated and observed) for such non-cohesive granular materials, the true diametral strain is considered which is different from the diametral strain within the elastic limit for small deformations.

Strain Ratio

The strain ratio (β) can be calculated from the following expression:

$$\beta = -\frac{\varepsilon_d}{\varepsilon_a} \qquad \textbf{(3-21)}$$

where ε_d and ε_a are the calculated true diametral stain and axial strain respectively applying a given pressure (p). The negative sign is to compensate for the diametral

elongation against the axial contraction of the sample. The evolution of the strain ratio can be approximated using the following expression:

$$\beta(c,r) = b_0(c) + b_1(c)r \qquad \textbf{(3-22)}$$

where $b_0\ (-)$ and $b_1\ (-)$ are two parameters which are function of the blend coke content (c) and were determined using optimisation procedure on the experimental data.

Figure 3-26 shows the evolution of the strain ratio, $\beta(c,r)$ with respect to sample shape ratio (r). It shows the evolution of the strain ratio exhibits linear tendency with the sample shape ratio while the impact of the blend coke content decreases drastically for the sample shape ratio lower than 0.3. Figure 3-27 shows the evolution of the parameters of $b_0(c)$ and $b_1(c)$. These parameters allow accurate representation of the impact of blend coke content. Thus, the experimental data are well represented by the model as follows:

$$b_0(c) = b_{00}^* + b_{01}^* c + b_{02}^* c^2$$
$$b_1(c) = b_{10}^* + b_{11}^* c + b_{12}^* c^2 \qquad \textbf{(3-23)}$$

where all the fine calibration parameters are unitless.

Using these, for the axial strain and strain ratio, it is now possible to predict the final shape of the puck after the application of the anode weight for a given sample shape ratio.

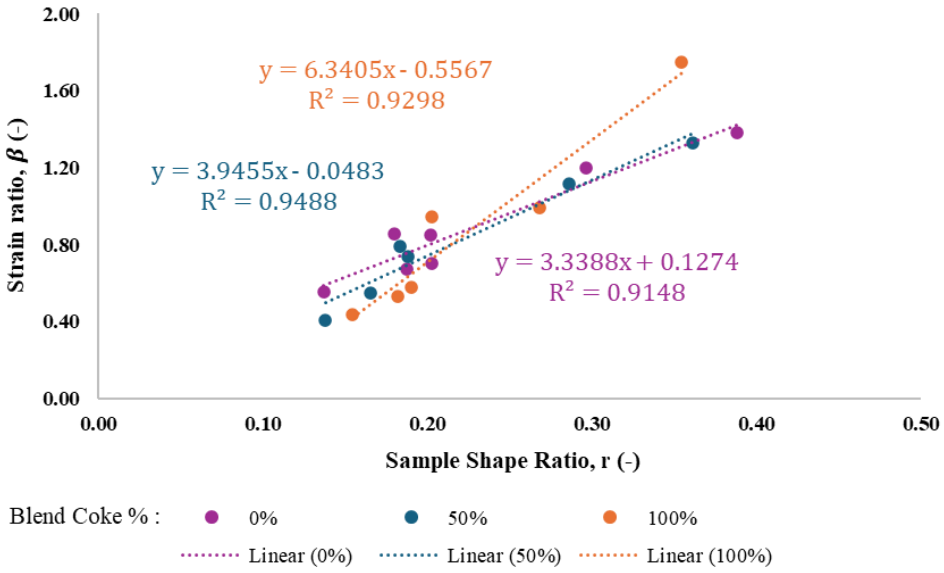

Figure 3-26 : Evolution of strain ratio with sample shape ratio (r)

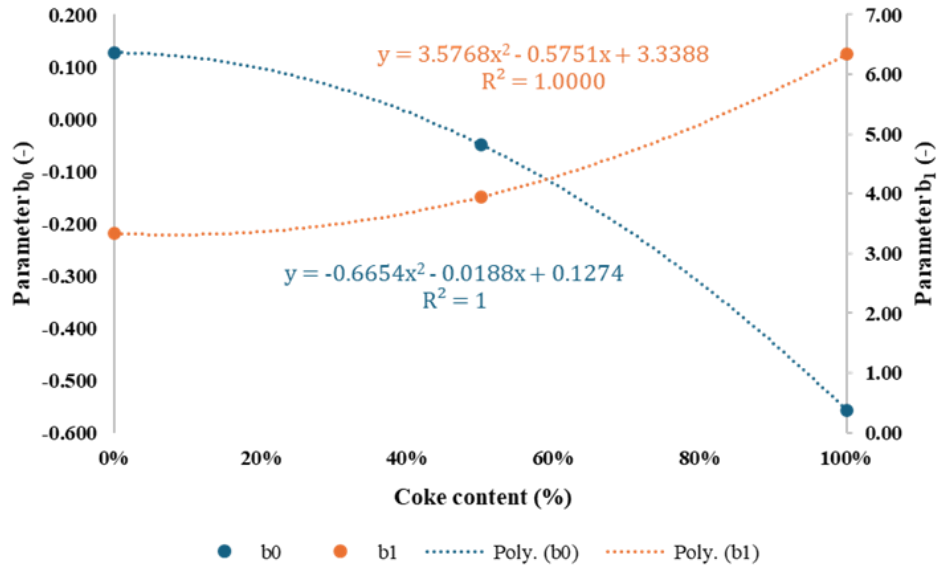

Figure 3-27 : Evolution of the parameters, b_0 and b_1 with blend coke content

Intermediate Diametral Ratio

The intermediate diametral ratio is given by:

$$\alpha = \frac{D_i}{D_0} \tag{3-24}$$

where D_i is the intermediate diameter obtained after removing the mould and before applying the pressure. The evolution of the intermediate diametral ratio (α) can be approximated using the following expression:

$$\alpha(c, r) = d_0(c) + d_1(c)r \tag{3-25}$$

where d_0 $(-)$ and d_1 $(-)$ are two parameters which are function of the blend coke content (c) and were determined using optimisation procedure on the experimental data.

Figure 3-28 shows the evolution of the intermediate diametral ratio, $\alpha(c, r)$ with respect to sample shape ratio (r). It shows the evolution exhibits linear tendency with the sample shape ratio. Figure 3-29 shows the evolution of the parameters of $d_0(c)$ and $d_1(c)$. These parameters allow accurate representation of the impact of blend coke content. It is important to note that as the coke and graphite have a similar particle size range, a change in particle size could lead to different results although these parameters are function of the blend coke content.

Thus, the experimental data are well represented by the model as follows:

$$d_0(c) = d_{00}^* + d_{01}^* c + d_{02}^* c^2$$
$$d_1(c) = d_{10}^* + d_{11}^* c + d_{12}^* c^2 \quad \textbf{(3-26)}$$

where all the fine calibration parameters are unitless.

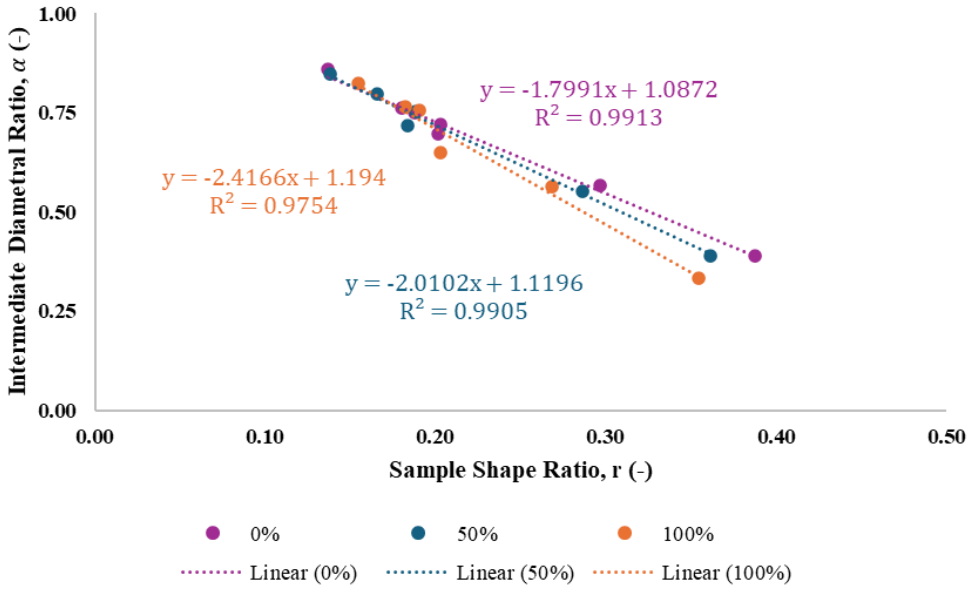

Figure 3-28 : Evolution of intermediate diametral ratio with sample shape ratio

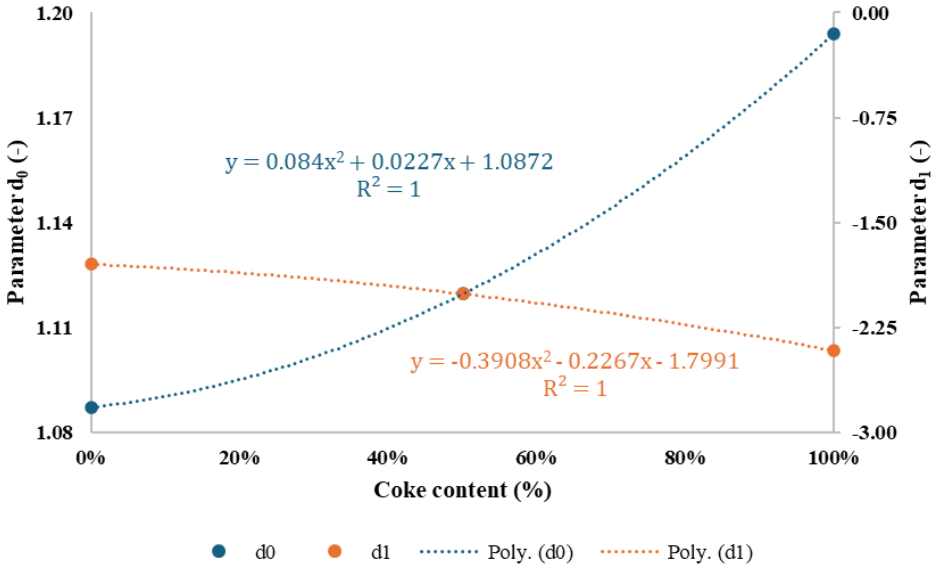

Figure 3-29 : Evolution of the parameters, d_0 and d_1 with blend coke content

3.4.2 Electrical Properties

Electrical Resistivity of the Granular Blends

The experimental granular electrical resistivity (ρ_g) values were plotted with the average granular temperature (T_g) for various pressures up to 500 kPa. It is observed that, for a given granular blend at constant pressure (except at 13.5 kPa as shown in Figure 3-30), the electrical resistivity decreases with increasing temperature. At lower temperatures, the decrease is more pronounced, whereas at higher temperatures it becomes more gradual. It is noteworthy to mention that the electrical resistivity decreases as the pressure increases for a constant temperature. With respect to temperature, it decreases as well for

a given pressure. The tendency remains the same for all the granular blends and can be observed in Figure 3-31, Figure 3-32 and Figure 3-33.

A small variation to the above-mentioned tendency is observed at the lower pressure of 13.5 kPa. This anomaly is observed for the granular blends at the lower pressure, although the values are extremely small. It is mentioned in the literature that for the 100% coke at lower pressure case (order of ~10 kPa), a little variation in the pressure brings changes into the electrical resistivity of the granular material. This is due to the possibility of thermal expansion of the granular sample which brings the change in contact surfaces among the granular particles. Thus, at low pressure, electrical resistivity is strongly related to the applied mechanical pressure. Therefore, a small pressure variation can have a significant impact on electrical resistivity of the granular materials [73].

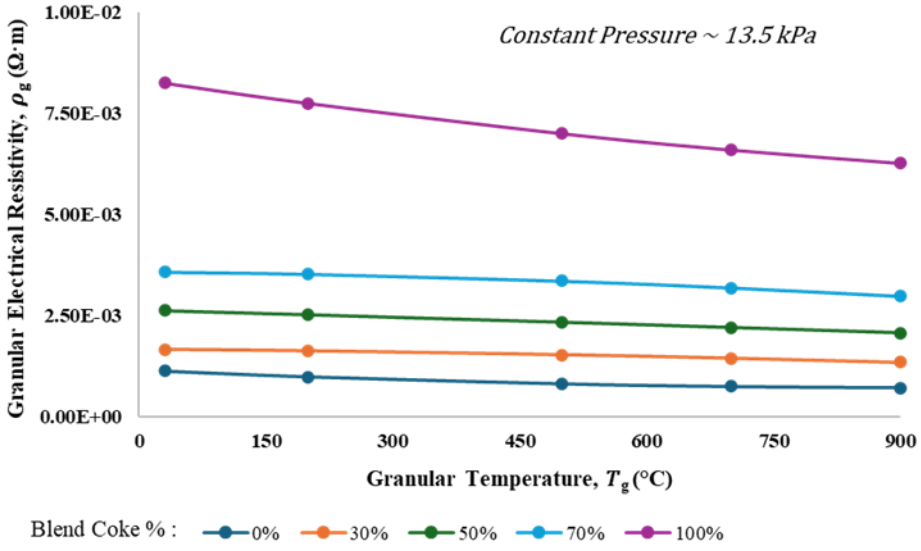

Figure 3-30 : Granular electrical resistivity at 13.5 kPa

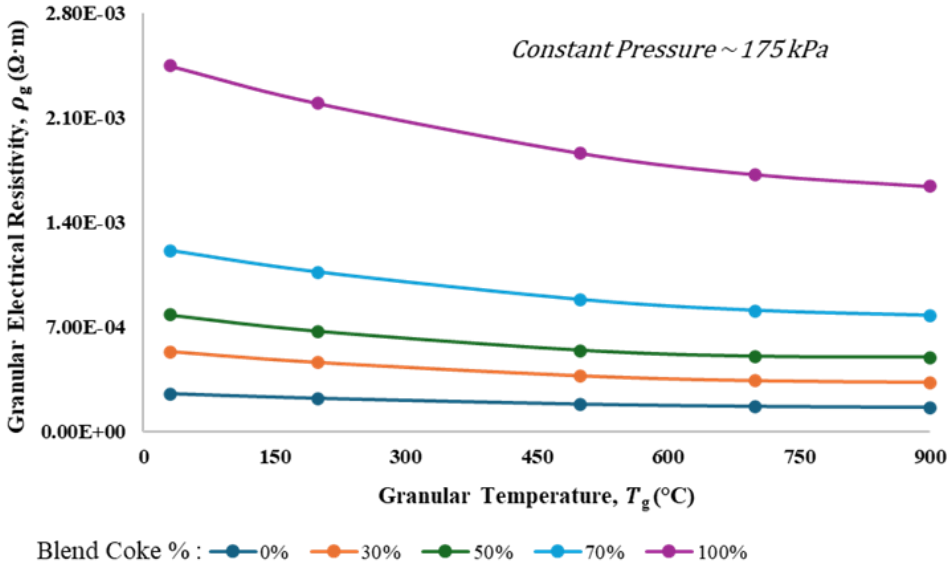

Figure 3-31 : Granular electrical resistivity at 175 kPa

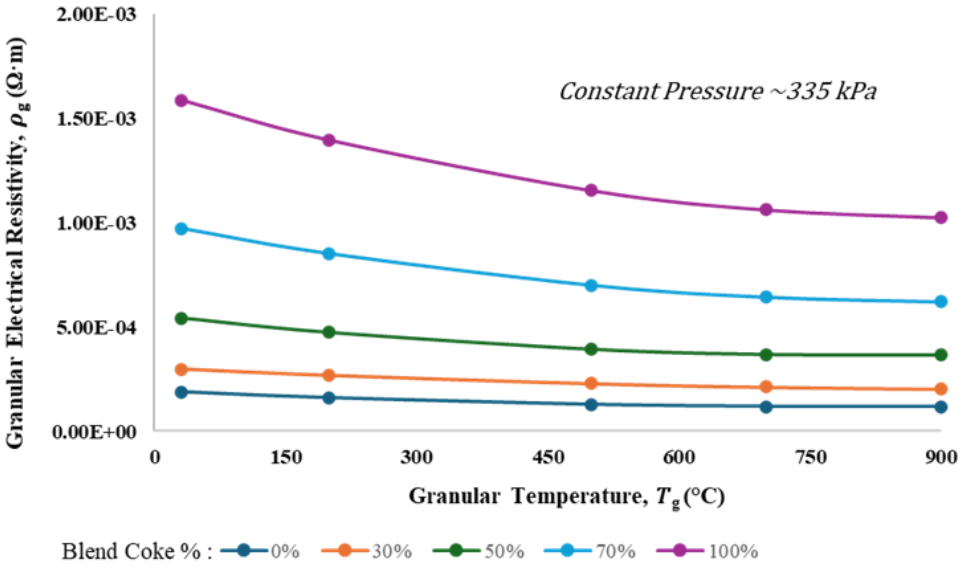

Figure 3-32 : Granular electrical resistivity at 335 kPa

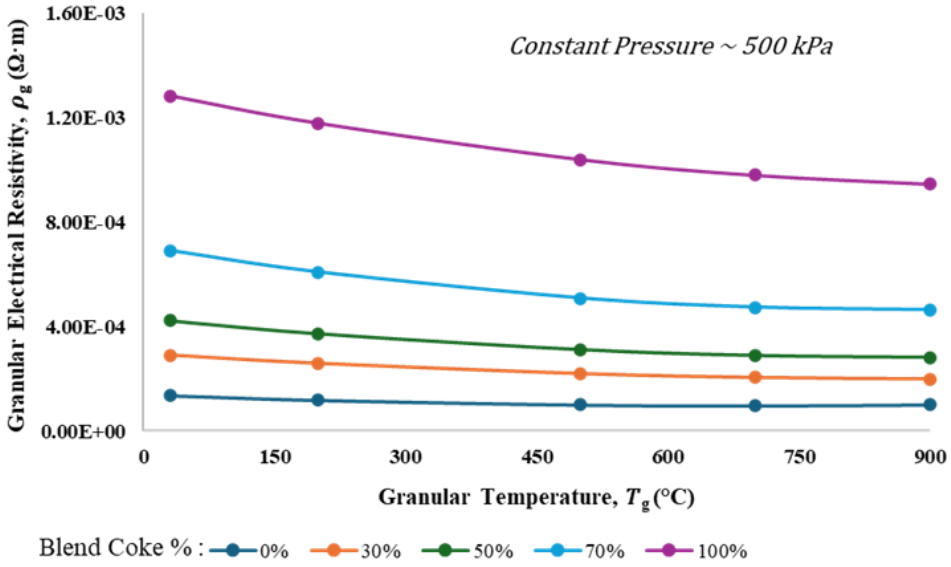

Figure 3-33 : Granular electrical resistivity at 500 kPa

Furthermore, at a constant temperature and pressure, the electrical resistivity increases with increasing coke content in the blend as illustrated in Figure 3-34. It can be noted that the electrical resistivity of C100 is the highest at a particular temperature and pressure as compared to other granular blends and it the lowest for G100. For other granular blends, it stays in between the two extreme values of C100 and G100. It can be said that the lying-bed using the granular blend having more coke content is going to give faster Joule's heating due to their higher electrical resistivity and *vice versa*.

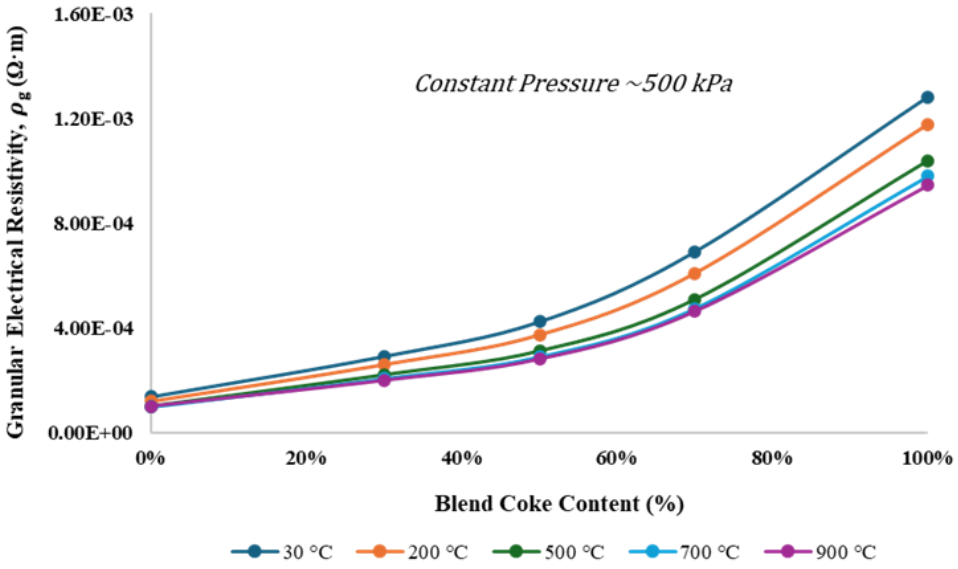

Figure 3-34 : Granular electrical resistivity with blend coke content

A model was developed to represent and predict the experimental data. The model is expressed by the following expression [70]:

$$\rho_g(T, c, p) = C_1(T, c)\, p^{C_2(T,c)} \qquad \textbf{(3-27)}$$

where, p (kPa) is the pressure, $C_1(T, c)$ (Ω·m·kPa^{-1}) and $C_2(T, c)$ $(-)$ are two parameters which are function of the temperature (T) and the blend coke content (c), are determined by using GRG nonlinear solver on experimental data. The model predictions were compared with the experimental results as shown in Figure 3-35. The comparison between the model and experimental data shows good agreement, indicating that the model adequately represents the experimental observations.

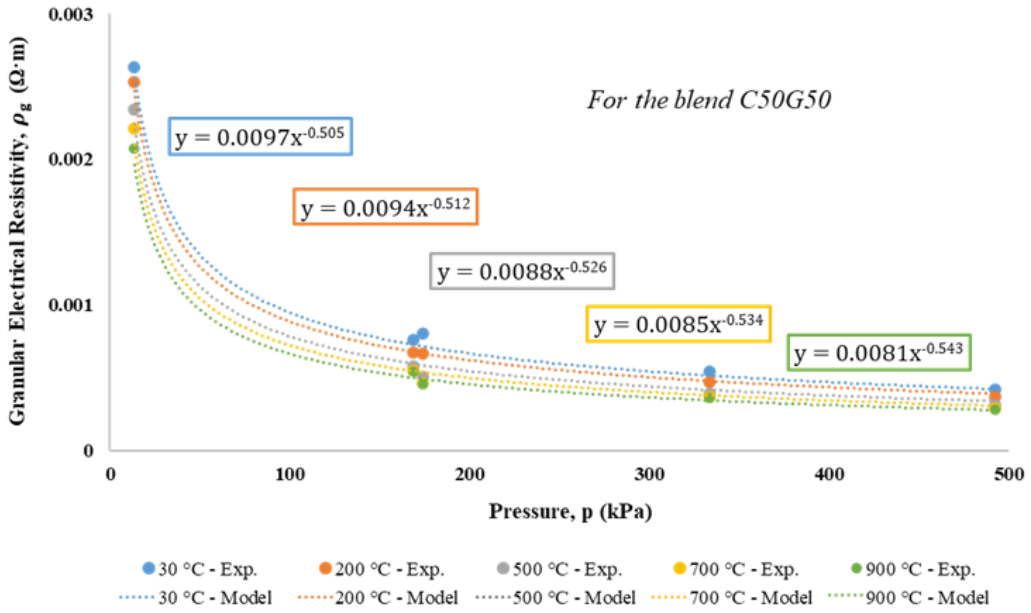

Figure 3-35 : Granular electrical resistivity (Experiment vs. Model)

The variations of the parameter, $C_1(T,c)$ with respect to temperature and blend coke content are shown in Figure 3-36 and Figure 3-37, respectively, and can be expressed as:

$$C_1(T,c) = A_1(T) \cdot B_1(c)$$

$$A_1(T) = a_{10} + a_{11}T \qquad \textbf{(3-28)}$$

$$B_1(c) = b_{10}e^{b_{11}c}$$

where, $A_1(T)$ (Ω·m·kPa^{-1}) and $B_1(c)$ $(-)$ are two functions depending on the fine calibration parameters: a_{10} (Ω·m·kPa^{-1}), a_{11} (Ω·m·kPa^{-1}·°C^{-1}), b_{10} $(-)$ and b_{11} $(-)$.

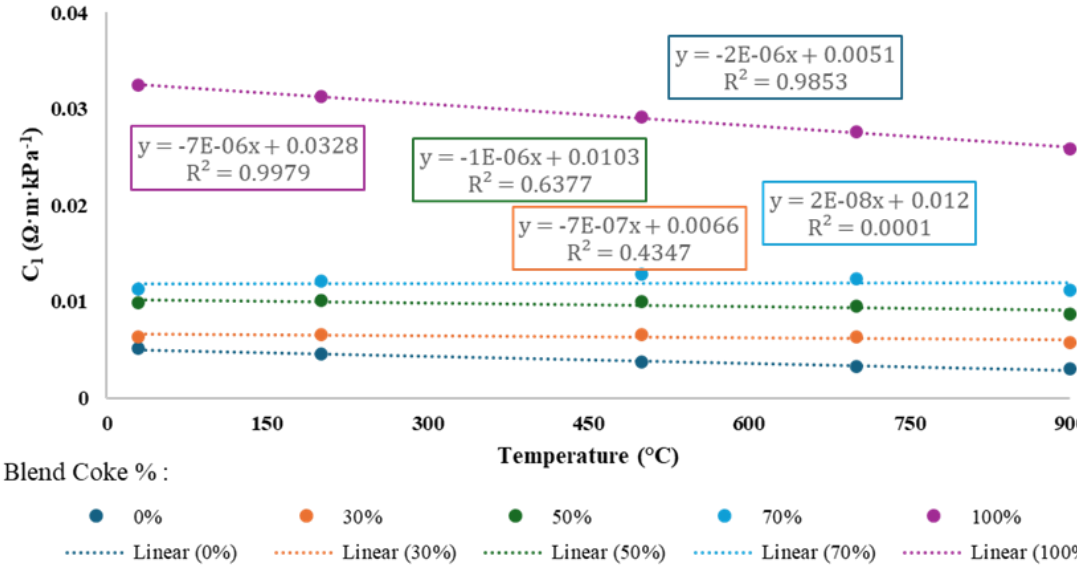

Figure 3-36 : Evolution of the parameter C_1 with temperature

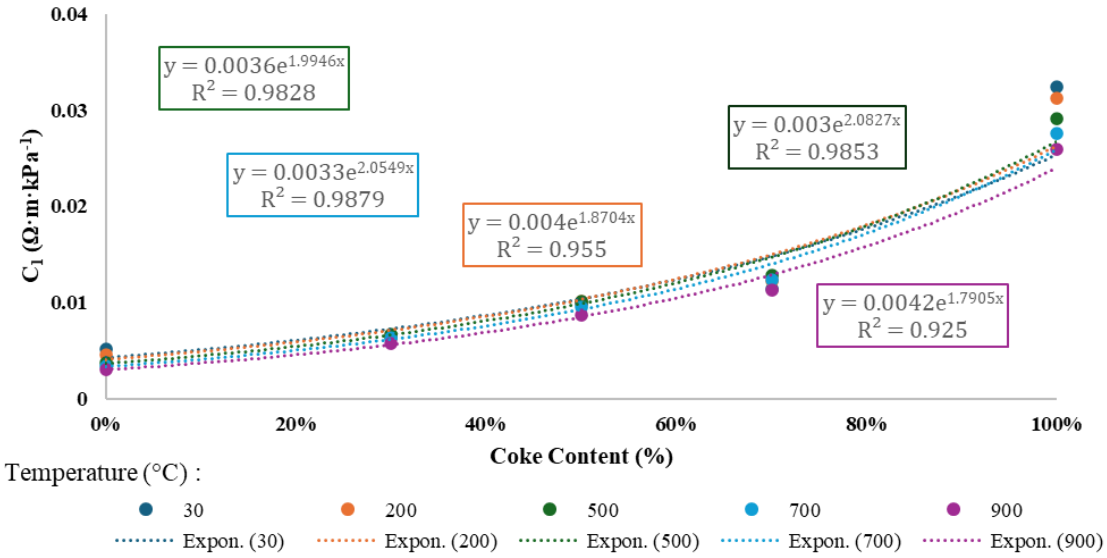

Figure 3-37 : Evolution of the parameter C_1 with blend coke content

Similarly, the variations of the parameter, $C_2(T,c)$ with respect to temperature and blend coke content are shown in Figure 3-38 and Figure 3-39, respectively, and can be expressed as:

$$C_2(T,c) = D_2(T) \cdot E_2(c)$$

$$D_2(T) = d_{20} + d_{21}T \qquad \textbf{(3-29)}$$

$$E_2(c) = e_{20} + e_{21}c + e_{22}c^2$$

where, $D_2(T)$ $(-)$ and $E_2(c)$ $(-)$ are two functions depending on the fine calibration parameters: d_{20} $(-)$, d_{21} $(°C^{-1})$, e_{20} $(-)$, e_{21} $(-)$ and e_{22} $(-)$.

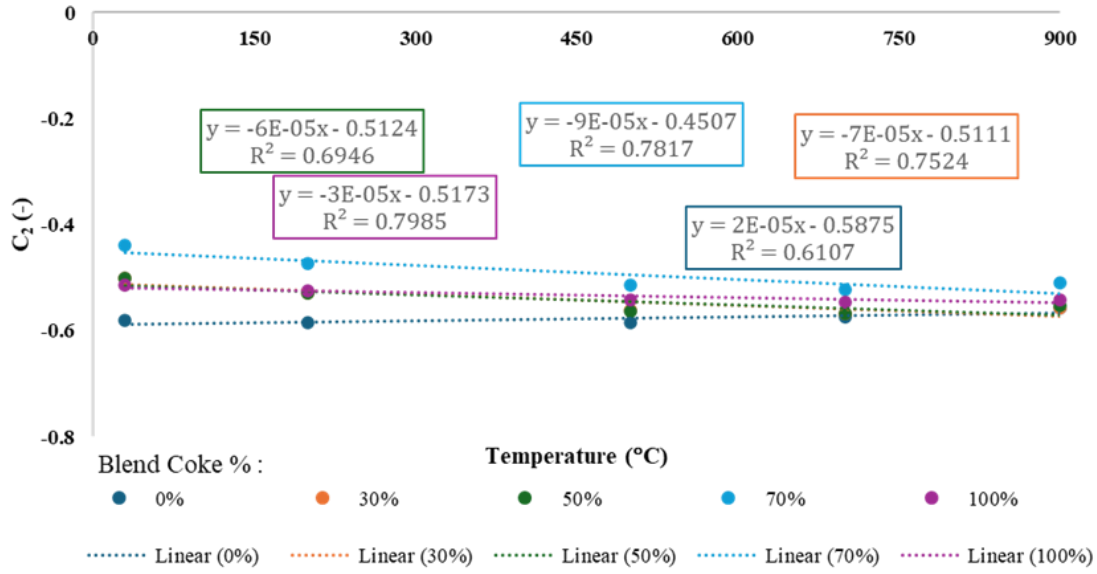

Figure 3-38 : Evolution of the parameter C_2 with temperature

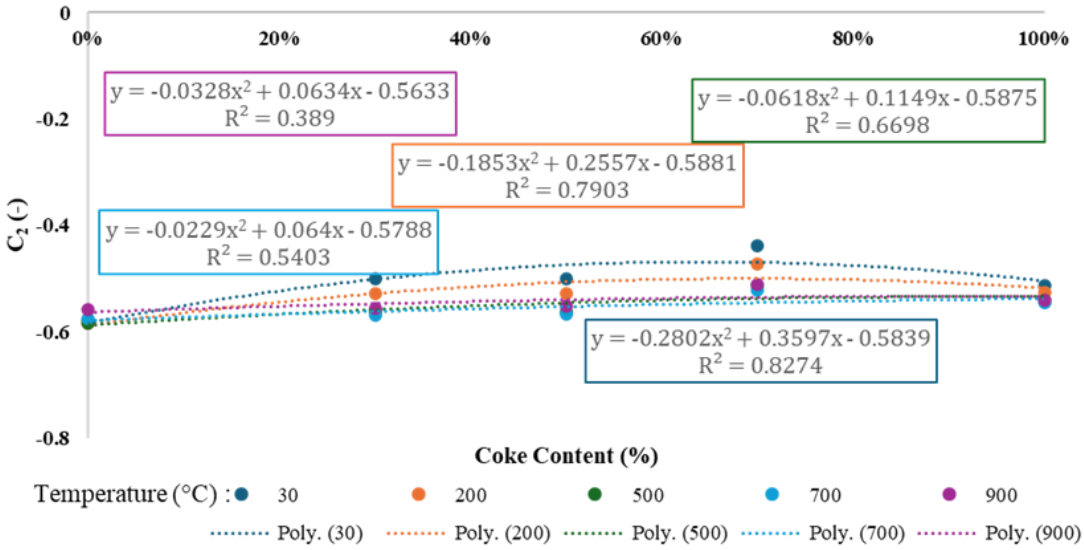

Figure 3-39 : Evolution of the parameter C_2 with blend coke content

Specific Electrical Contact Resistivity between Anode and Granular Blends

The specific electrical contact resistivity (SECR) values were obtained from the voltage drops by extrapolating to the contact surface/interface. The variation of SECR between the anode and the granular blend (ρ_c^{a-g}) with the anode-granular interface temperature (T_{cs}) for different granular blends at constant pressures (175 kPa and 500 kPa) is shown in Figure 3-40 and Figure 3-41 respectively. It can be observed that, there is no significant variation in anode-granular SECR with the interface temperature for a particular granular blend and pressure. A slight decrease in the SECR is observed with the increase in anode-granular interface temperature.

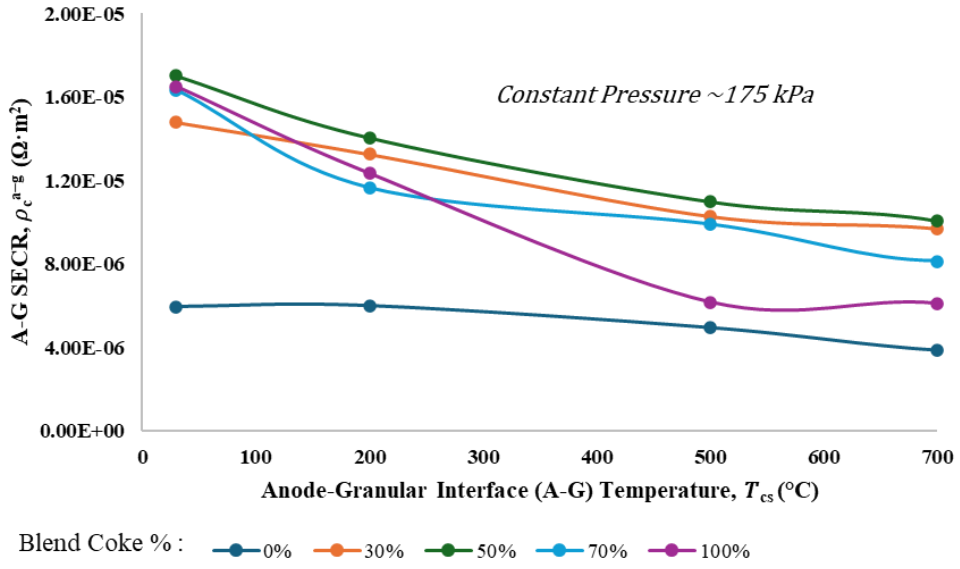

Figure 3-40 : Anode-Granular SECR at 175 kPa

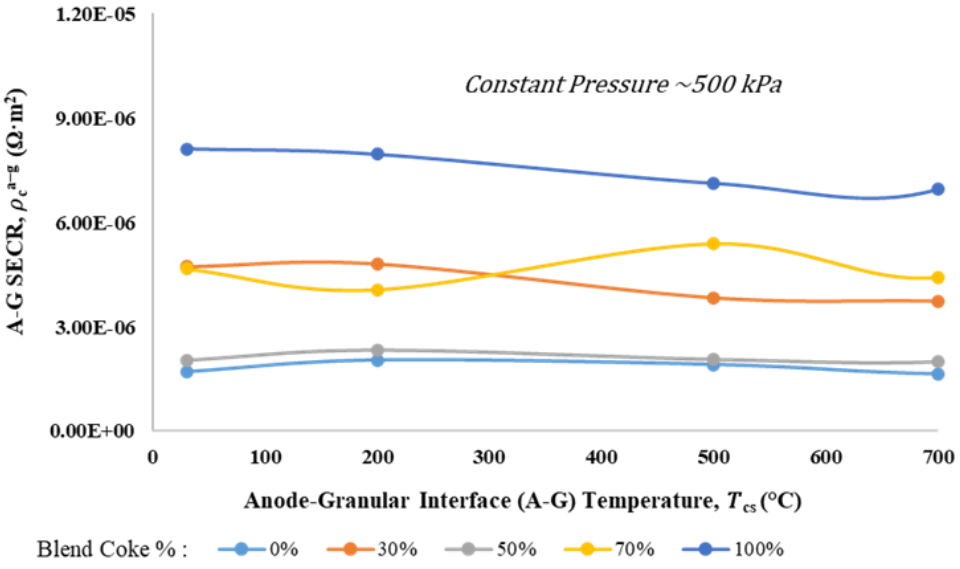

Figure 3-41 : Anode-Granular SECR at 500 kPa

Figure 3-41 demonstrates that, the anode-granular SECR for C100 is the highest whereas it is the lowest for the G100 and the values for C50G50 stays just above the G100 and way below the C100. It is clearly due to the difference in the resistivities of granular coke and granular graphite. However, the tendencies of C30G70 and C70G30, can be explained by the variation of the particle sizes range and the roughness of the anode surface which has a great influence on the interface contact surface area.

In fact, two factors simultaneously influencing the SECR here. First, the lower resistivity granular material (blend coke content) is playing a reducing role. Second, the higher particle size range granular material is playing an amplifying role. Hence, we get the variations in the SECR tendencies for C30G70 and C70G30. Similar conclusions can be made for the variations observed in Figure 3-40.

The variation of SECR between the anode and the granular blend with blend coke content at different interface temperatures at constant pressures (175 kPa and 500 kPa) is shown in Figure 3-42 and Figure 3-43 respectively. It can be observed that, they vary significantly with the coke content of the blends at a particular interface temperature and pressure. The tendencies here can be explained by the simultaneous impact of the blend coke content, the variation in the particle size range and the roughness of the anode surface (as explained before). At 175 kPa SECR values show less variation as compared to that of at 500 kPa for the higher blend coke content granular material.

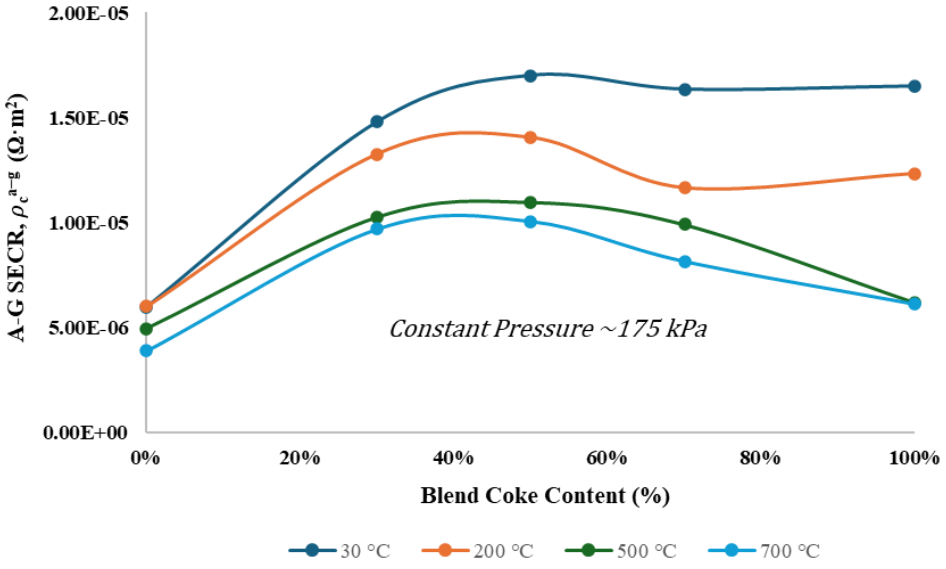

Figure 3-42 : Anode-Granular SECR with blend coke content at 175 kPa

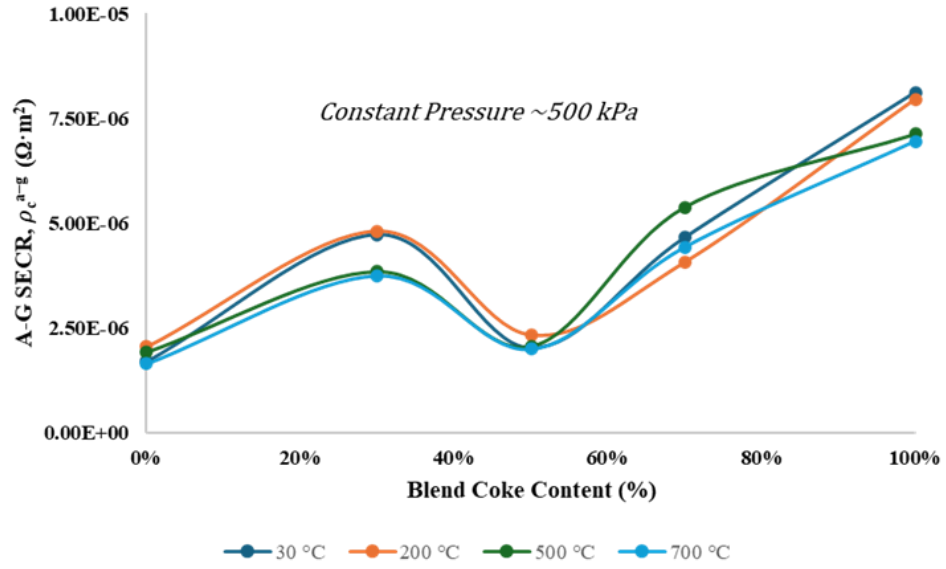

Figure 3-43 : Anode-Granular SECR with blend coke content at 500 kPa

All the experimental data are fitted into the model as per the following equation:

$$\rho_c^{a-g}(T,c,p) = C_3(T,c)\, p^{C_4(T,c)} \qquad \textbf{(3-30)}$$

where, p (kPa) is the pressure, $C_3(T,c)$ ($\Omega{\cdot}m^2{\cdot}kPa^{-1}$) and $C_4(T,c)$ $(-)$ are two parameters which are the function of the temperature (T) and the blend coke content (c), and are determined by using GRG nonlinear solver on experimental data.

The variations of the parameter, $C_3(T,c)$ with respect to temperature and blend coke content are shown in Figure 3-44 and Figure 3-45, respectively, and can be expressed as:

$$C_3(T,c) = A_3(T) \cdot B_3(c)$$

$$A_3(T) = a_{30} + a_{31}T + a_{32}T^2 \qquad \textbf{(3-31)}$$

$$B_3(c) = b_{30}e^{b_{31}c}$$

where, $A_3(T)$ ($\Omega{\cdot}m^2{\cdot}kPa^{-1}$) and $B_3(c)$ $(-)$ are two functions depending on the fine calibration parameters: a_{30} ($\Omega{\cdot}m^2{\cdot}kPa^{-1}$), a_{31} ($\Omega{\cdot}m^2{\cdot}kPa^{-1}{\cdot}°C^{-1}$), a_{32} ($\Omega{\cdot}m^2{\cdot}kPa^{-1}{\cdot}°C^{-2}$), b_{30} $(-)$ and b_{31} $(-)$.

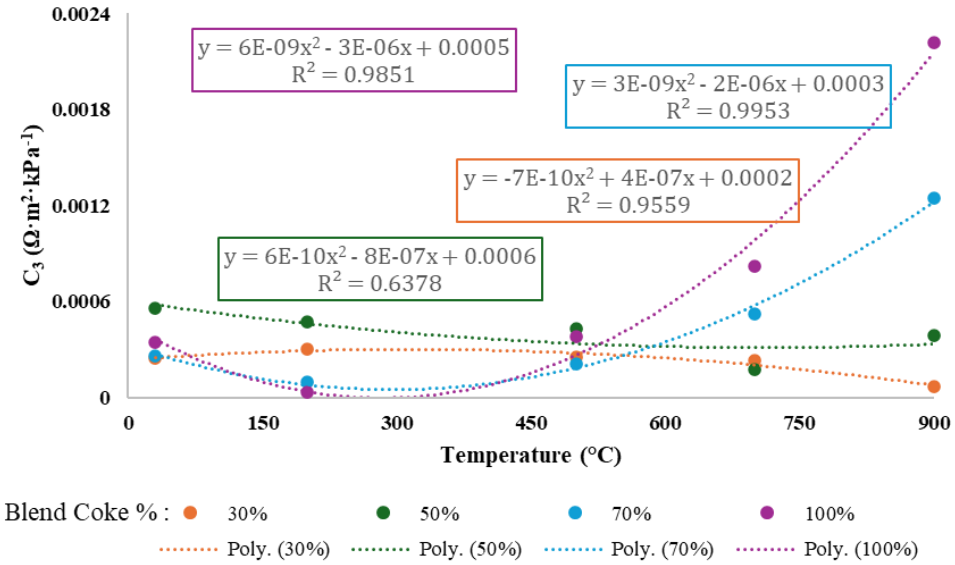

Figure 3-44 : Evolution of the parameter C_3 with temperature

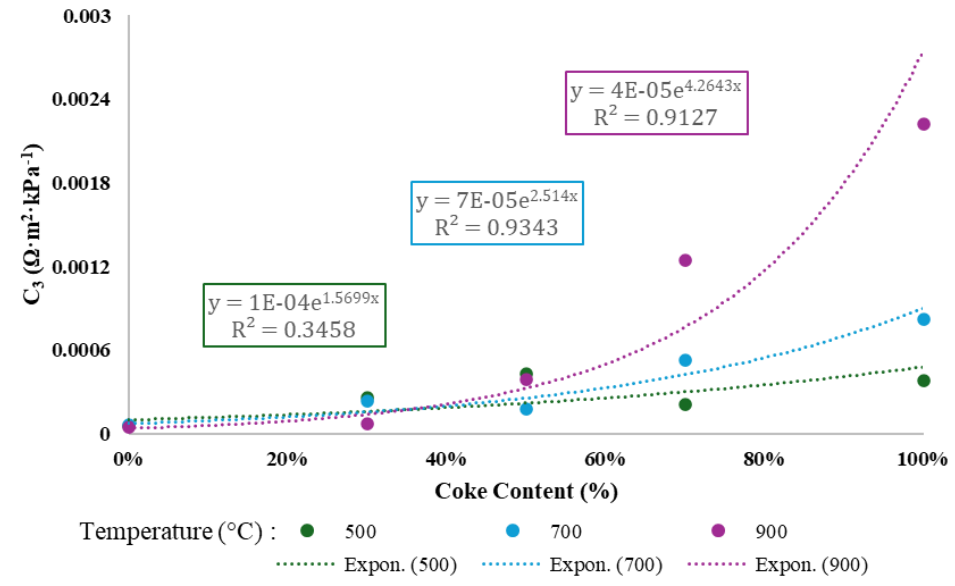

Figure 3-45 : Evolution of the parameter C_3 with blend coke content

Similarly, the variations of the parameter, $C_4(T,c)$ with respect to temperature and blend coke content are shown in Figure 3-46 and Figure 3-47, respectively and can be expressed :

$$C_4(T,c) = D_4(T) \cdot E_4(c)$$

$$D_4(T) = d_{40} + d_{41}T \qquad \textbf{(3-32)}$$

$$E_4(c) = e_{40} + e_{41}c + e_{42}c^2$$

where, $D_4(T)$ $(-)$ and $E_4(c)$ $(-)$ are two functions depending on the fine calibration parameters: d_{40} $(-)$, d_{41} $(°C^{-1})$, e_{40} $(-)$, e_{41} $(-)$ and e_{42} $(-)$.

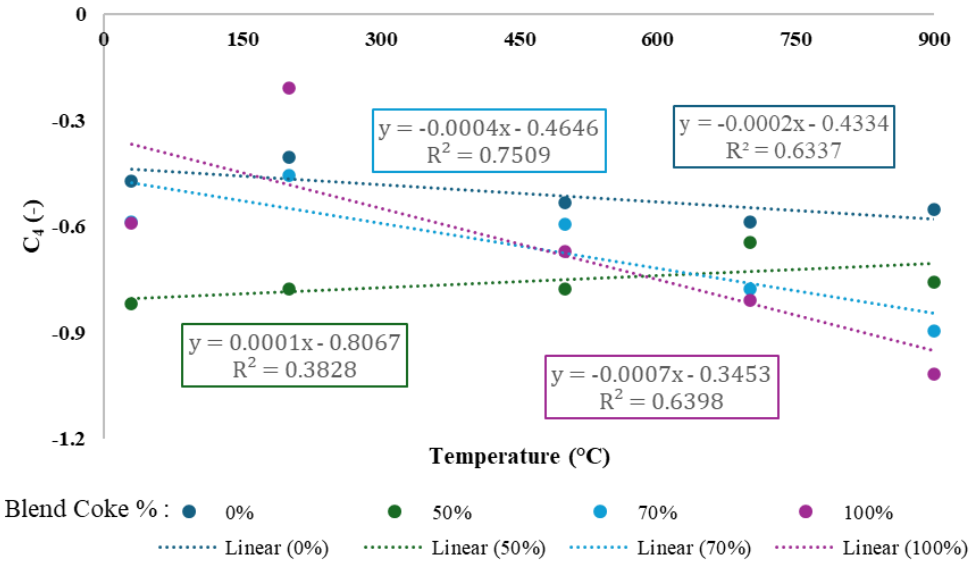

Figure 3-46 : Evolution of the parameter C_4 with temperature

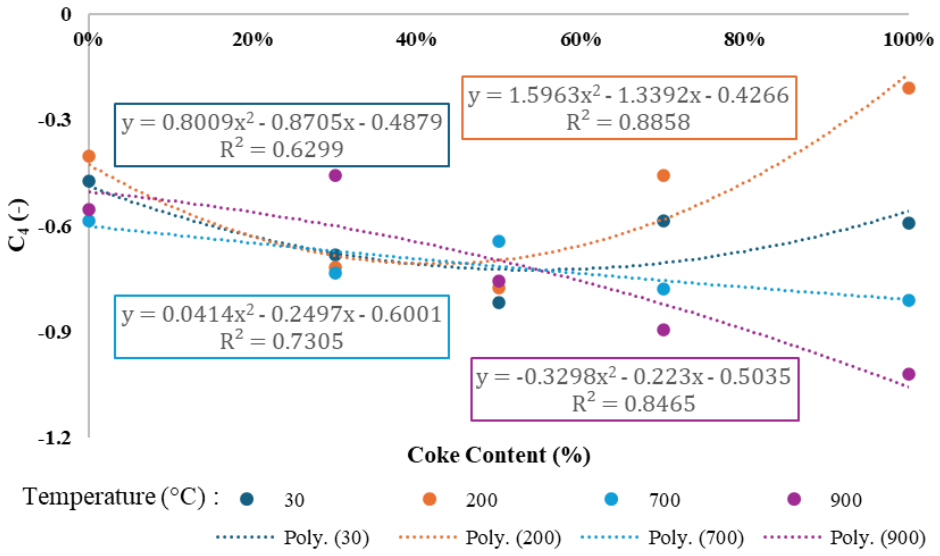

Figure 3-47 : Evolution of the parameter C_4 with blend coke content

Specific Electrical Contact Resistivity between Cathode and Granular Blends

The SECR between the cathode and the various granular blends was determined in the same manner as for the anode and compared with the corresponding values for the anode to establish a scaling factor. The variation of SECR between the cathode and the granular blend (ρ_c^{c-g}) with the cathode-granular interface temperature (T_{cs}) for different granular blends at constant pressure is shown in Figure 3-48. It can be observed that, there is no significant variation in cathode-granular SECR with the interface temperature for a particular granular blend and a pressure. This time they show similar tendencies but in a very orderly and expected manner as compared to the anode-granular SECR. This is probably due to the smoothness of the cathode surface area.

The variation of SECR between the cathode and the granular blends with blend coke content at different interface temperatures at a constant pressure is shown in Figure 3-49. It can be observed that, they vary significantly with the coke content of the blend at a particular interface temperature and pressure.

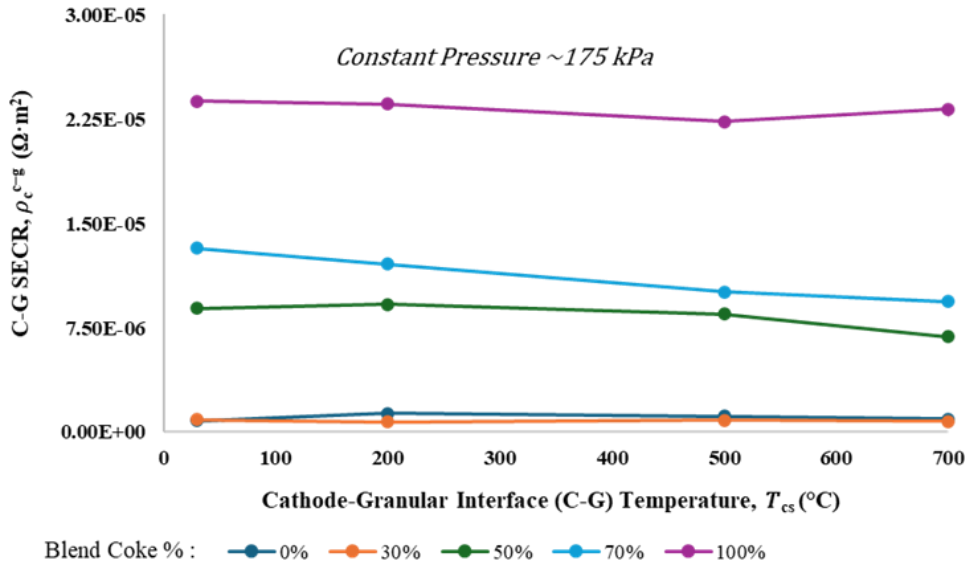

Figure 3-48 : Cathode-Granular SECR at 175 kPa

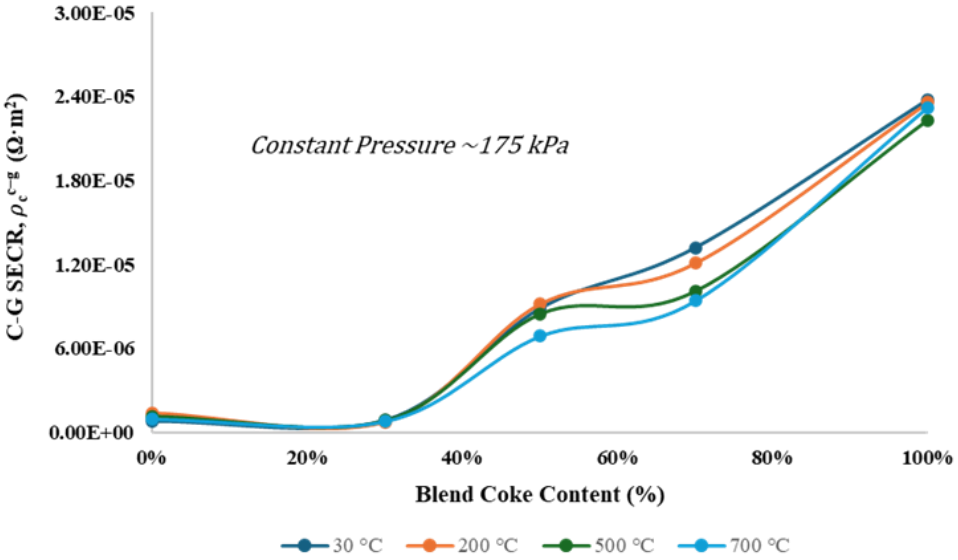

Figure 3-49 : Cathode-Granular SECR with blend coke content

A comparison of the SECR values between the anode–granular blend and the cathode–granular blend can be done by defining a scaling factor (SF) and can be written as:

$$\text{Scaling Factor, SF} = \frac{\rho_c^{a-g}}{\rho_c^{c-g}} \qquad \textbf{(3-33)}$$

For C70G30 blend, a comparison of the SECR values between the anode–granular blend and the cathode–granular blend reveals a scaling factor which depends on the applied pressure and is illustrated in Figure 3-50. As pressure increases the SF decreases and it get saturated towards the higher pressure (of the order of ~500 kPa). It is due to the increase in contact pressure which allows a better electrical conduction. The increase in the pressure nullifies the effect of the roughness of the electrode surfaces. Hence, the

SECR values between the anode–granular blend and the cathode–granular blend becomes similar at higher applied pressures as depicted in Figure 3-50.

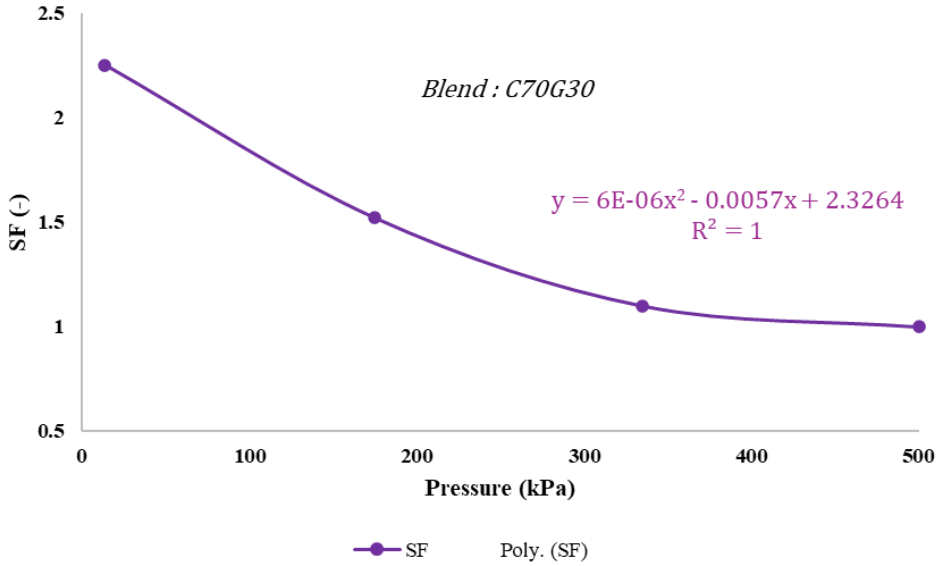

Figure 3-50 : Variation of SF with applied pressure

In a similar manner to the previous case, all the experimental data are fitted into the model as per the following equation:

$$\rho_c^{c-g}(T,c,p) = C_5(T,c)\, p^{C_6(T,c)} \qquad \textbf{(3-34)}$$

where, p (kPa) is the pressure, $C_5(T,c)$ ($\Omega \cdot m^2 \cdot kPa^{-1}$) and $C_6(T,c)$ $(-)$ are two parameters which are the function of the temperature (T) and the blend coke content (c), are determined by using GRG nonlinear solver on experimental data are expressed as follows:

$$C_5(T,c) = A_5(T) \cdot B_5(c)$$

$$A_5(T) = a_{50} + a_{51}T + a_{52}T^2 \quad \textbf{(3-35)}$$

$$B_5(c) = b_{50}e^{b_{51}c}$$

where, $A_5(T)$ ($\Omega \cdot m^2 \cdot kPa^{-1}$) and $B_5(c)$ $(-)$ are two functions depending on the fine calibration parameters: a_{50} ($\Omega \cdot m^2 \cdot kPa^{-1}$), a_{51} ($\Omega \cdot m^2 \cdot kPa^{-1} \cdot °C^{-1}$), a_{52} ($\Omega \cdot m^2 \cdot kPa^{-1} \cdot °C^{-2}$), b_{50} $(-)$ and b_{51} $(-)$.

$$C_6(T,c) = D_6(T) \cdot E_6(c)$$

$$D_6(T) = d_{60} + d_{61}T \quad \textbf{(3-36)}$$

$$E_6(c) = e_{60} + e_{61}c + e_{62}c^2$$

where, $D_6(T)$ $(-)$ and $E_6(c)$ $(-)$ are two functions depending on the fine calibration parameters: d_{60} $(-)$, $d_{61}(°C^{-1})$, e_{60} $(-)$, e_{61} $(-)$ and e_{62} $(-)$.

CHAPTER 4

MODELLING OF HEAT GENERATION DURING PREHEATING

4.1 General Information

In this chapter, the material properties characterised in the earlier chapter were systematically used for the modified puck geometry. Based on the modified geometry, the equivalent electrical resistivity of the system was calculated by accounting for the combined effects of material composition, packing behaviour, and contact conditions. In addition, the puck geometry in the lying-bed pattern of the granular material was determined to represent the realistic arrangement of particles under the applied loading conditions.

The outcomes of this chapter establish a consistent and physically representative set of geometric and electrical parameters. These parameters serve as critical input data for the thermo-electrical simulations presented in the following chapter, thereby ensuring continuity and reliability in the overall modelling approach.

4.2 Heat Generation during Preheating

The lying-bed used for the preheating of reduction cell is composed of a granular coke and graphite blend in a specific ratio. To enable uniform positioning of the lying-bed, a template mould is used consisting of cylindrical holes located at specific locations (see Figure 2-4). After the coke/graphite blend is placed adequately in each hole, the mould is removed, allowing each cylindrical puck to reach its position of repose which correspond to a truncated cone (as illustrated in Figure 4-1a). Before starting the preheating, the anodes are placed on the truncated cones, causing axial and diametral deformation of the latter due to the weight of the anode assembly and solid bath covering (as depicted in Figure 4-1b).

Geometric changes in the puck necessarily imply a modification of the pressure applied to it, which has a direct effect on the confinement of the granular material and, by the same way, on its electrical properties such as the electrical resistivity of the granular material and the specific electrical contact resistivity (SECR) at the granular blend to anode and granular blend to cathode interfaces. Considering that the reduction cell preheating is obtained using Joule effect, it is a crucial issue to determine the efficient quantity of material participating to the heat generation. In the context of numerical modelling, it remains essential to consider representative values of these electrical properties. The objective of this work is to develop a strategy to obtain realistic heat generation in the granular blend during the numerical modelling.

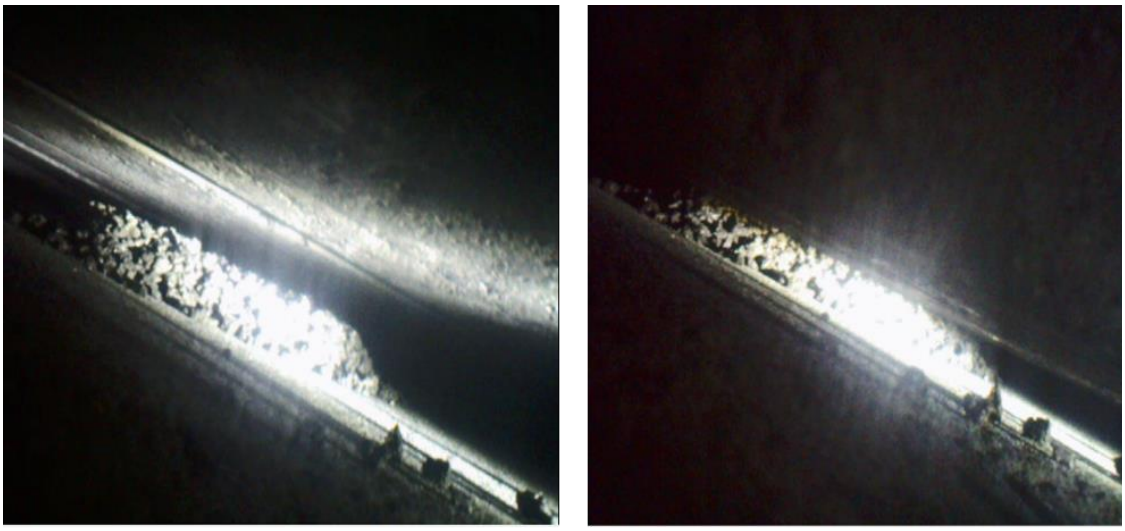

a) Before the anode load b) After the anode load

Figure 4-1 : A typical puck deformation during preparation phase

The traditional industrial procedure used to preheat the reduction cell is based on electrical energy conversion to thermal one (by Joule's heating effect). To do so, DC current of high amperage is applied to the cell during several hours to increase the temperature in the cell components close to the electrolysis zone to the target temperature (960 °C). To accelerate the process, an electrically resistive material, such as coke and/or graphite granular blends, are sandwiched between the cathode and the anode. The granular blend experiences the increase of temperature while being under the load (of anode and crushed bath material). Figure 4-2 shows an operational state of the puck in the lying-bed under pressure and temperature.

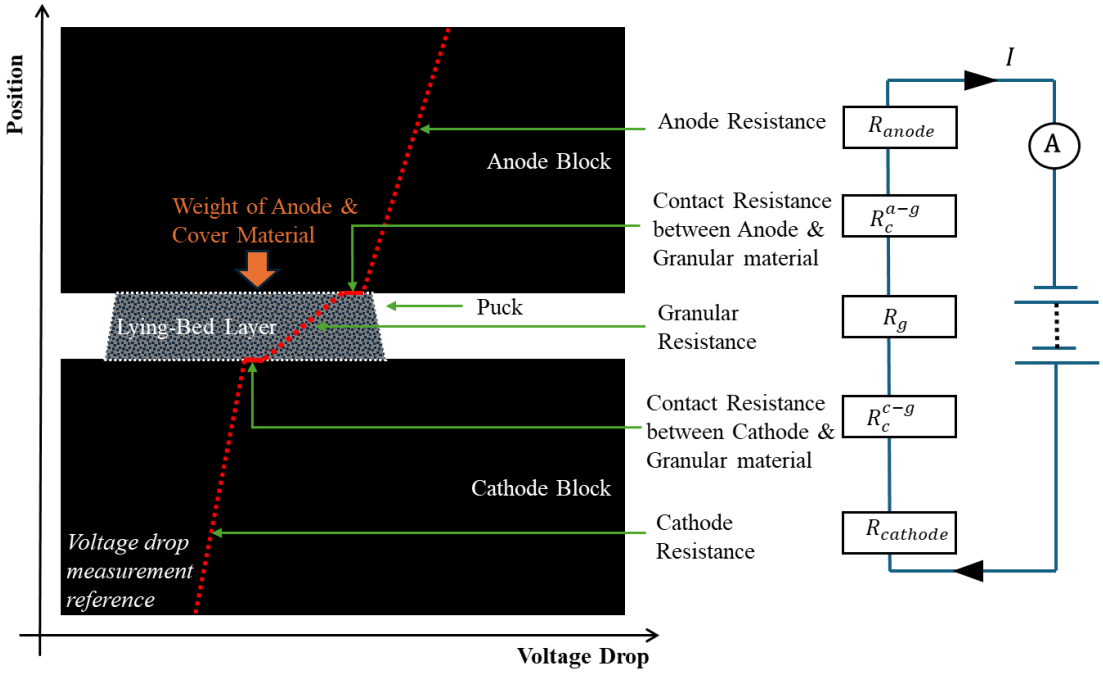

Figure 4-2 : Operational state of the puck under load and direct current

To determine the heat generation, first consider the power (P) in an electrically resistive material is given by:

$$P = RI^2 \qquad \textbf{(4-1)}$$

where R and I are the equivalent electrical resistance and the electrical current respectively. Considering that the medium is a non-cohesive granular coke/graphite cylindrical puck of diameter d and height h in contact on each side with a specific material (anode on top and cathode on bottom), it becomes:

$$P = \left(\rho_c^{a-g} + h\rho_g + \rho_c^{c-g}\right)\frac{I^2}{S} \qquad \textbf{(4-2)}$$

where ρ_g, ρ_c^{a-g} and ρ_c^{c-g} are the electrical resistivity of the granular blend and the SECR at the granular to anode and granular to cathode interfaces respectively and S is the cross-sectional surface area of the puck. These electrical properties have been obtained from experiments and show specific pressure and temperature dependencies. Knowing that the current density (j) crossing the surface area of the granular blend is given by:

$$j = \frac{I}{S} \qquad \textbf{(4-3)}$$

Now, the power can be rewritten as:

$$P = \left(\rho_c^{a-g} + h\rho_g + \rho_c^{c-g}\right)j^2 S \qquad \textbf{(4-4)}$$

4.3 Assumptions and Proposed Approach

Considering the specific behaviour of non-cohesive granular material as well as the industrial procedure for the lying-bed setup and preheating, the following assumptions can be made:

1. During the preheating, the degrees of freedom at the connection of the anode rod suggest that the anode assembly remains in a floating condition over the pucks and the bottom face of the anode remains in the horizontal plane during the preheating.
2. The main deformation (axial and diametral) of the puck occurs during the installation of the anode assembly and the solid crushed bath on it. Any changes in the load will allow negligible change in the shape of the puck but allows changes in the electrical behaviour in the compound and at the interfaces.
3. The only change in contact pressure at the anode to the puck interface during the preheating comes from the movement of the cathode surface.
4. Since electrical current will only pass through the less resistive path, only the cylindrical part of the deformed puck (using the top diameter of the truncated cone as shown in red in Figure 4-5) will contribute to the heat generation. All the granular materials exceeding this volume are useless, not contributing to the heat generation.

In this way, the proposed TE modelling approach is as follows and described in Figure 4-3:

1. The puck is modeled as a cylinder with diameter (d_0) and height (h_0) corresponding to the initial geometry and considered as a thermo-electric component. In this configuration, the pressure (p_{aa}) is evenly distributed over each puck under the anode before starting the preheating.

2. To consider the impact of the puck deformation (compaction and geometry changes) on the energy transfer, the electrical properties of the puck and interfaces will be scaled to represent the properties on the deformed puck.

3. To avoid the computation of a pressure dependent electrical resistivity in the granular blend material (ρ) and simplify the energy transfer, the total electrical resistance (R) of the puck and interfaces will be merged into an equivalent specific electrical resistivity ($\bar{\rho}$) totally applied in the granular blend material and computed using a constant pressure corresponding to the number and diameter of pucks under one anode.

4. To allow electrical and thermal transfer between the granular material and the anode and cathode, infinite thermal contact conductance (TCC) and infinite electrical contact conductance (ECC) at both interfaces are considered.

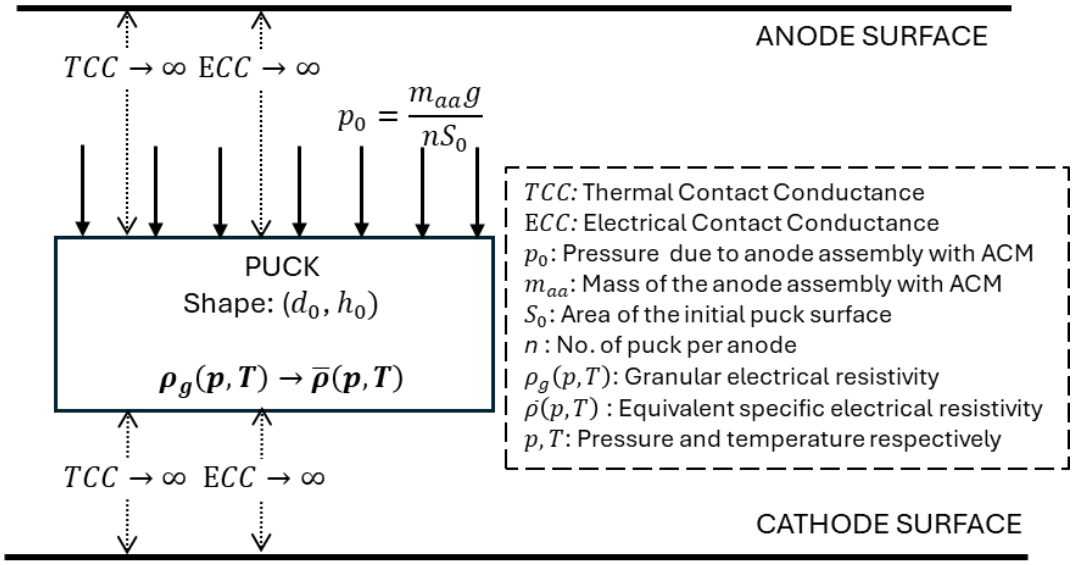

Figure 4-3 : Details of the proposed TE modelling approach

4.3.1 Equivalence and Scaling of the Electrical Power

Points 2 and 3 of the proposed approach require that the power expressed by Equation (4-2) and applied to the final shape of the puck (P_f) be equal to that using an equivalent specific electrical resistivity ($\bar{\rho}$) totally applied in the granular blend material on the initial shape of the puck. To do so, P_f can be written as:

$$P_f = \left(\rho_{cf}^{a-g} + h_f \rho_{gf} + \rho_{cf}^{c-g}\right)\frac{I^2}{S_f} \qquad \textbf{(4-5)}$$

where ρ_{gf}, ρ_{cf}^{a-g} and ρ_{cf}^{c-g} are the electrical properties evaluated on the final geometry of the puck and thus, with at pressure p_f evaluate on the final section area ($S_f = {\pi d_f^2}/{4}$)

and at a specific temperature. Expressing the same electrical power on the initial shape of the puck and using the only equivalent specific electrical resistivity ($\bar{\rho}$) gives:

$$P_0 = \bar{\rho}\, h_0 \frac{I^2}{S_0} \qquad \textbf{(4-6)}$$

where h_0 is the initial height and S_0, the initial section area ($S_0 = {}^{\pi d_0^2}/_4$). Since P_0 must be equal to P_f, maintaining equality between Equation (4-5) and Equation (4-6) we get:

$$\bar{\rho} = \left(\rho_{cf}^{a-g} + h_f \rho_{gf} + \rho_{cf}^{c-g}\right) \frac{1}{h_0} \left(\frac{d_0}{d_f}\right)^2 \qquad \textbf{(4-7)}$$

Computation of Equation (4-7), requires the evaluation of the initial height (h_0) and final diameter (d_f) of the puck. The next sub-sections explain how to obtain these values.

4.4 Geometrical Changes of the Puck

In this section, the geometrical changes of the puck due to the flowability—granular material property and the applied load on it are discussed in detail mathematically. (See *APPENDIX 2 : Effect of Flowability and Load on Granular Blend*)

4.4.1 After Lifting of the Template Mould (from Initial to Intermediate Shape)

Any volume of a granular material resting on a horizontal plane, and subject to its own weight, will flow on its periphery to maintain its static equilibrium. The angle between the horizontal plane and the inclined wall is called the angle of repose. For non-cohesive granular material, the angle of repose (θ_r) can be approximated by the internal friction angle (ϕ) of the material as obtained with a direct shear test for various pressures and expressed using the Mohr-Coulomb law (Figure 4-4).

Applying this concept to the puck having cylindrical volume of diameter (d_0) and height (h_0) will adopt the intermediate truncated conical geometry shown on Figure 4-5 (as dotted line). Considering this shape, the relationship between the intermediate bottom diameter (d_i^b) and intermediate top diameter (d_i^t) is given by:

$$d_i^t = d_i^b - 2a \qquad \textbf{(4-8)}$$

where a is determined using the trigonometric relation between the puck initial height (h_0) and the angle of repose (θ_r) such that:

$$a = \frac{h_0}{tan(\theta_r)} \qquad \textbf{(4-9)}$$

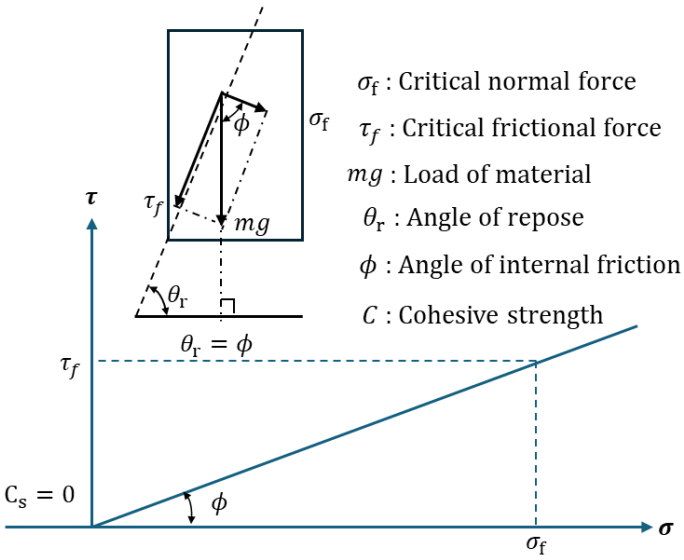

Figure 4-4 : Relationship between angle of repose and angle of internal friction for non-cohesive granular material

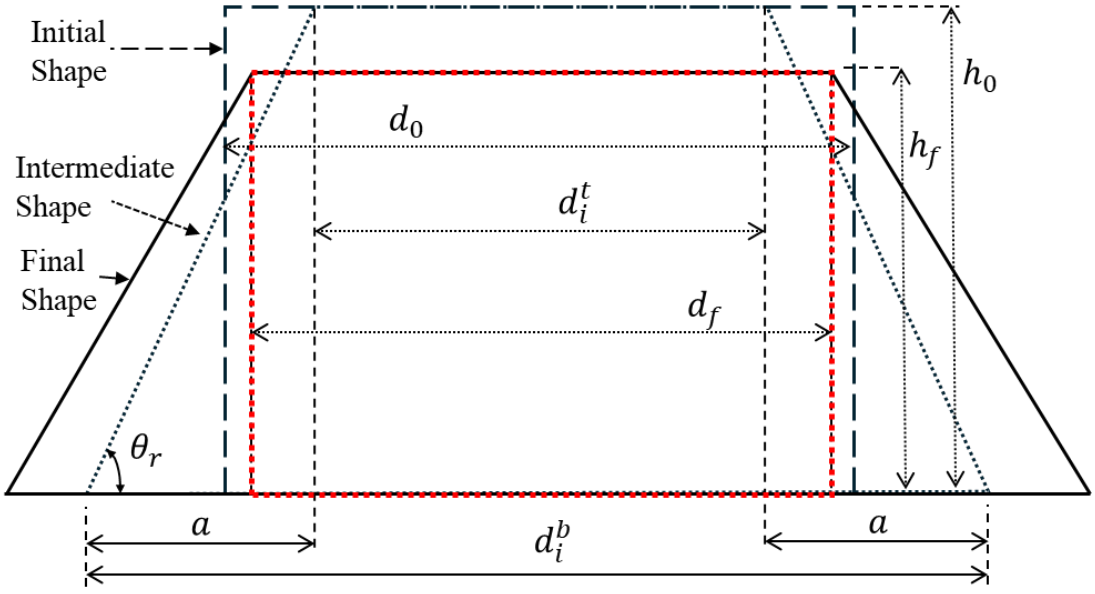

Figure 4-5 : Initial, intermediate and final deformed shape of the granular puck

Considering that the initial and intermediate volumes remain the same and are given respectively by:

$$V_{initial} = \frac{\pi h_0 d_0^2}{4} \tag{4-10}$$

and

$$V_{intermediate} = \frac{\pi h_0 {d_i^b}^2}{12}\left[1 + \frac{d_i^t}{d_i^b} + \left(\frac{d_i^t}{d_i^b}\right)^2\right] \tag{4-11}$$

Replacing Equation (4-8) in Equation (4-11) and assigning equality between Equations (4-10) and Equation (4-11) give the quadratic expression in terms of d_i^t such that:

$$\frac{\pi h_0 d_0^2}{4} - \frac{\pi h_0 \left(3{d_i^t}^2 + 6d_i^t\, cot(\theta_r)\right) + 4h_0^2\, cot^2(\theta_r)}{12} = 0 \tag{4-12}$$

The solution of Equation (4-12) for d_i^t gives:

$$d_i^t = \frac{-h_0 \pm \frac{1}{3}\sqrt{-3h_0^2 + 9d_0^2 tan^2(\theta_r)}}{tan\,(\theta_r)} \tag{4-13}$$

Considering that d_i^t is positive, the only admissible root is given by:

$$d_i^t = \frac{-h_0 + \frac{1}{3}\sqrt{-3h_0^2 + 9d_0^2 tan^2(\theta_r)}}{tan\,(\theta_r)} \qquad \textbf{(4-14)}$$

4.4.2 After the Load Application (from Intermediate to Final Shape)

The final shape can be determined by considering the axial and diametral deformations due to the pressure associated to the anode and ACM loading. In the diametral direction, the strain (ε_d) corresponding to the change in top diameter from the intermediate (d_i^t) to the final shape (d_f) can be determined by using Equation (3-20).

In the axial direction, the strain (ε_a) from the intermediate to the final shape can be calculated from the relation given by Equation (3-15).

To establish the relation with the applied pressure (p), the axial strain (ε_a) can also be expressed using the Voce's law as mentioned in Equation (3-16). Considering that the pressure corresponds to a specific mass (m) applied on the final shape (d_f, h_f), Equation (3-16) can be rewritten as:

$$\varepsilon_a = -\varepsilon_0 \left(1 - e^{-\frac{4Amg}{\pi d_f^2}}\right) \qquad \textbf{(4-15)}$$

The relationship between the axial and diametral strain, defined as the strain ratio (β) can be calculated by using the Equation (3-21). This strain ratio (β), which must not be confused with the Poisson's ratio (ν). Poisson's ratio (ν) is only valid for small deformations and within the elastic limit whereas strain ratio (β) is calculated in a similar manner for the large deformations.

Substituting the values of the axial strain (ε_a) and the diametral strain (ε_d) in the strain ratio (β), gives the cubic expression as follows:

$$ln\left(\frac{d_f}{d_i^t}\right) - \beta\varepsilon_0 \left(1 - e^{-\frac{4Amg}{\pi d_f^2}}\right) = 0 \qquad \textbf{(4-16)}$$

Solution of Equation (4-16) required iterative process such as Newton-Raphson solution technique with $d_f = d_i^t$ as an initial guess.

To complete, the final height (h_f) is obtained using Equation (4-15) in Equation (4-16) such that:

$$ln\left(\frac{h_f}{h_0}\right) = -\varepsilon_0\left(1 - e^{-\frac{4Amg}{\pi d_f^2}}\right) \quad \textbf{(4-17)}$$

By rearranging the terms of Equation (4-17) and using the solution of d_f we get the expression as:

$$h_f = e^{ln(h_0)-\varepsilon_0\left(1-e^{-\frac{4Amg}{\pi d_f^2}}\right)} \quad \textbf{(4-18)}$$

4.4.3 Experimental Verification

Exploiting the proposed approach requires not only knowledge of the electrical properties of the blend and interfaces, but also, the angle of repose as well as the evolution of the axial and diametral strain of the blend under vertical pressure. To do so, extensive experimental program has been conducted to determine:

1. The electrical resistivity of the blend as a function of the pressure and temperature for different coke/graphite ratio.
2. The specific electrical contact resistivity at the blend to anode and blend to cathode interfaces as a function of the pressure and temperature for different coke/graphite ratio.

3. The angle of repose from direct shear tests on coke/graphite blends for different coke/graphite ratio.
4. The axial strain vs. pressure and diametral strain vs. pressure relationships from compaction tests for different coke/graphite ratio and sample shape ratio (r).

Regarding Point 3., Figure 3-19 shows the evolution of the angle of repose (θ_r) for different granular blends. For Point 4., Figure 4-6 shows the parts of the experiment conducted for the validation. Figure 4-7 and Figure 4-8 exhibit the evolution of the axial strain (ε_a) and the strain ratio (β) for a specific sample shape ratio ($r = \frac{54.03}{152.40} = 0.355$).

(a) C100 granular in the mould

(b) Measurement of the top diameter

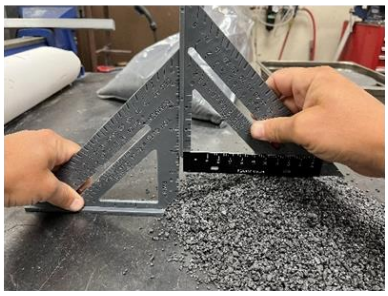

(c) Measurement of the height

Figure 4-6 : Experiment on C100 granular with a specific mould

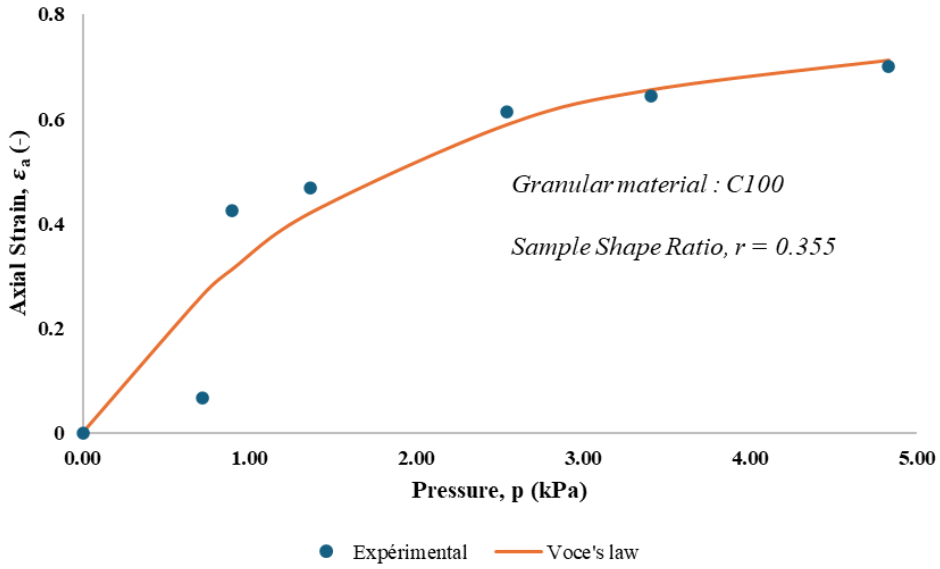

Figure 4-7 : Evolution of axial strain with pressure

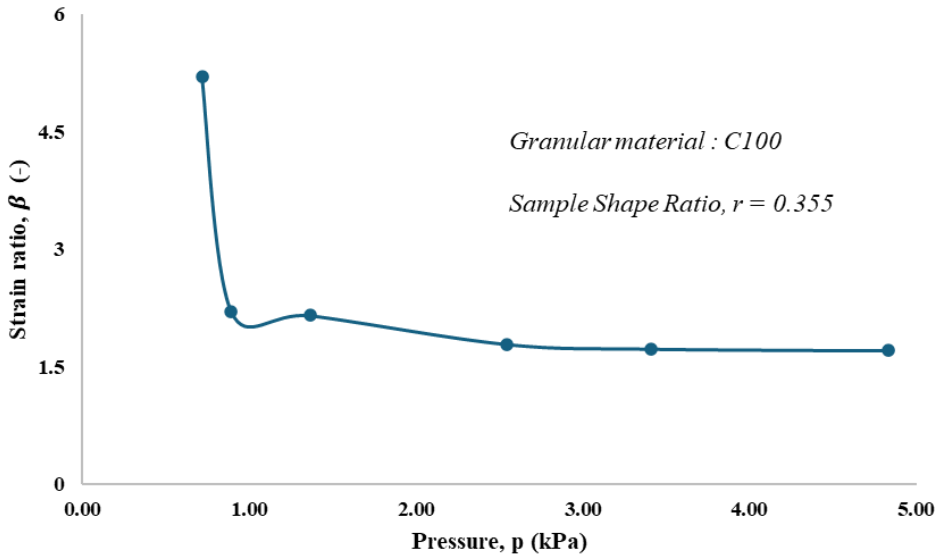

Figure 4-8 : Evolution of strain ratio with pressure

During experiment dedicated to the compaction test, it has been observed, after removing the mould, that the blend did not flow to the intermediate shape as a perfect truncated cone. The side of the intermediate shape over the height shows a curved profile which indicates that the angle of repose seems to evolve over the height of the sample. From the physical point of view, the angle of repose depends only on the granulometry of the material. However, the low height of the samples under study and the relative size of the aggregates (compared to the height of the samples) favor the formation of this profile.

These last observations no longer allow using Equation (4-14) for the computation of the intermediate top diameter since the intermediate volume is not a perfect truncated cone. To overcome this difficulty, it is proposed to express the intermediate diametral ratio (α) as a function of the coke content but also, of the sample shape ratio (r) such as:

$$\alpha = f(c, r) \qquad \textbf{(4-19)}$$

where $f(c, r)$ must be determined using experimental data. Using Equation (4-19) for a given value of c and r gives this intermediate top diameter directly. Figure 3-28 shows that the intermediate top diameter ratio (α), for a given coke content, evolves as a linear function of the sample shape ratio. Therefore, Equation (4-14) and Equation (4-19) can be used to determine the effective angle of repose (θ_r^{eff}) required to maintain a perfect truncated cone such as:

$$\theta_r^{eff} = tan^{-1}\left(\frac{h_0\left(3d_i^t + \sqrt{12d_0^2 - 3{d_i^t}^2}\right)}{3\left(d_0^2 - {d_i^t}^2\right)}\right) \quad \textbf{(4-20)}$$

4.4.4 Validation

To validate the proposed approach, some results are extracted from the experiment and industrial investigation and compared to those obtained using the model. For all the cases, the coke content and shape ratio have been used to determine the effective angle of repose (θ_r^{eff}) and then used in Equation (4-14) to determine the top intermediate diameter (d_i^t). The final diameter (d_f) and height (h_f) are computed using Equation (4-16) and Equation (4-18) respectively. The results obtained from the model show a good match with the experimental data.

Table 4-1 shows these results for blends of different coke/graphite ratio and puck shape ratio (which is the sample shape ratio). The yellow cells indicate an error over 10%. The largest error (17.9%) represents a 2.34 mm difference in the final height of the sample. The orange case shown in Table 4-1 exhibits investigation conducted in the industry to determine the intermediate and final deformed shapes. To do so, four pucks of the common coke/graphite (50%) blend and sample shape ratio ($r = 0.12$) have been released from the mould and then compressed using a standard carbon anode assembly.

On the other hand, Table 4-2 shows the difference between the physical angle of repose and the effective angle of repose for the same cases. The yellow cells indicate differences over 10%. Considering that the top intermediate diameter is accurately measured, this comparison clearly shows that, in some cases, the blend doesn't flow to the intermediate shape as a perfect truncated cone.

Table 4-1 : Comparison of experimental data with model for various granular blends with different sample shape ratio

Geometry			Coke	Intermediate Diameter			Mass	Final Diameter			Final Height		
D0	h0	r=h0/Do	Content	Experiment	Model	Error		Experiment	Model	Error	Experiment	Model	Error
(mm)	(mm)	(-)	%	(mm)	(mm)	%	(kg)	(mm)	(mm)	%	(mm)	(mm)	%
100,00	29,66	0,30	0,0%	56,66	55,36	2,3%	11,00	125,19	110,90	11,4%	14,18	15,93	12,3%
152,40	59,13	0,39	0,0%	59,23	59,31	0,1%	11,00	176,13	182,10	3,4%	25,92	26,88	3,7%
152,40	30,74	0,20	0,0%	106,19	110,38	3,9%	11,00	146,59	149,77	2,2%	20,29	21,00	3,5%
171,56	32,15	0,19	0,0%	128,72	135,43	5,2%	11,22	162,38	163,68	0,8%	22,36	21,49	3,9%
194,80	26,69	0,14	0,0%	167,22	155,76	6,9%	11,22	178,34	175,38	1,7%	23,84	21,77	8,7%
100,00	28,61	0,29	50,0%	55,34	54,45	1,6%	11,00	116,93	103,24	11,7%	13,99	15,83	13,2%
152,40	55,11	0,36	50,0%	59,40	59,85	0,8%	11,00	165,87	168,96	1,9%	25,42	25,96	2,1%
152,40	28,69	0,19	50,0%	114,55	112,96	1,4%	11,00	146,61	144,12	1,7%	19,33	20,20	4,5%
171,56	28,40	0,17	50,0%	136,74	134,99	1,3%	11,22	153,81	160,27	4,2%	22,51	21,38	5,0%
180,00	22,00	0,12	50,0%	145,00	157,30	8,5%	431,00	180,00	173,17	3,8%	18,00	17,63	2,1%
194,85	26,89	0,14	50,0%	165,18	163,46	1,0%	11,22	177,42	183,30	3,3%	22,66	21,98	3,0%
100,00	26,84	0,27	100,0%	56,50	54,55	3,5%	11,00	115,80	103,23	10,9%	13,04	15,38	17,9%
152,40	54,03	0,35	100,0%	50,80	51,41	1,2%	11,00	168,68	173,89	3,1%	26,82	26,28	2,0%
152,40	29,05	0,19	100,0%	115,20	111,78	3,0%	11,00	139,60	141,18	1,1%	20,90	20,30	2,9%
171,56	31,22	0,18	100,0%	131,36	127,00	3,3%	11,22	155,02	156,97	1,3%	23,27	22,68	2,5%
194,80	30,09	0,15	100,0%	160,69	159,90	0,5%	11,22	172,37	176,53	2,4%	25,55	23,81	6,8%

Table 4-2 : Comparison of angle of repose with effective angle of repose for various granular blends with different sample shape ratio

Geometry			Coke Content	Angle of Repose		
D0	h0	r=h0/Do		ϕ	ϕ_{eff}	Error
(mm)	(mm)	(-)	%	(°)	(°)	(%)
100,00	29,66	0,30	0,0%	35,22	36,18	2,7%
152,40	59,13	0,39	0,0%	35,22	34,81	1,2%
152,40	30,74	0,20	0,0%	35,22	34,90	0,9%
171,56	32,15	0,19	0,0%	35,22	37,98	7,8%
194,80	26,69	0,14	0,0%	35,22	44,71	27,0%
100,00	28,61	0,29	50,0%	37,57	34,44	8,3%
152,40	55,11	0,36	50,0%	37,57	32,99	12,2%
152,40	28,69	0,19	50,0%	37,57	38,25	1,8%
171,56	28,40	0,17	50,0%	37,57	40,11	6,8%
180,00	22,00	0,12	50,0%	37,57	32,96	12,3%
194,85	26,89	0,14	50,0%	37,57	42,89	14,2%
100,00	26,84	0,27	100,0%	39,92	33,40	16,3%
152,40	54,03	0,35	100,0%	39,92	30,42	23,8%
152,40	29,05	0,19	100,0%	39,92	39,06	2,1%
171,56	31,22	0,18	100,0%	39,92	38,87	2,6%
194,80	30,09	0,15	100,0%	39,92	42,22	5,8%

4.5 Computation of the Equivalent Specific Electrical Resistivity

Prior to the numerical simulation, the equivalent specific electrical resistivity ($\bar{\rho}$) must be evaluated in a range of admissible pressure and temperature. Considering that ρ_{gf}, ρ_{cf}^{a-g} and ρ_{cf}^{c-g} are a function of the pressure, temperature and coke content, the following procedure is proposed:

1. For a specific coke content (c) and puck shape ratio ($r = \frac{h_0}{d_0}$), determine the value of the top intermediate diameter (d_i^t) using Equation (4-19) as well as the parameters β and S_f in Equation (4-16).

2. Considering a given mass to be applied on the puck, compute the pressure on the initial shape (p_0) and the final diameter (d_f) by solving Equation (4-16) and h_f using Equation (4-18).
3. For a given range of temperature (T_i) to be used for the definition of the equivalent specific electrical resistivity ($\bar{\rho}$) in ANSYS™:
    a. Express the pressure p_0 on the final deformed shape of the puck (p_f) such that: $p_f = p_0 \left(\frac{d_0}{d_f}\right)^2$.
    b. Evaluate $\rho_{gf}(p_f, T_i)$, $\rho_{cf}^{a-g}(p_f, T_i)$ and $\rho_{cf}^{c-g}(p_f, T_i)$.
    c. Compute ($\bar{\rho}$) from Equation (4-7).

Figure 4-9, Figure 4-10 and Figure 4-11 show the resulting evolution of ρ_{gf}, ρ_{cf}^{a-g} and ρ_{cf}^{c-g} as well as $\bar{\rho}$ with the applied pressure at a specific temperature. It is noteworthy to mention that:

1. Computation of the angle of repose using Equation (4-14) is not really required since the main interest is on the computation of d_i^t which can be computed directly using Equation (4-19).

2. To ensure the reliability of d_i^t, d_f and h_f, an associated experimental error computation must be performed.

3. A procedure has been developed in Excel™ to ensure an accurate computation of $\bar{\rho}$.

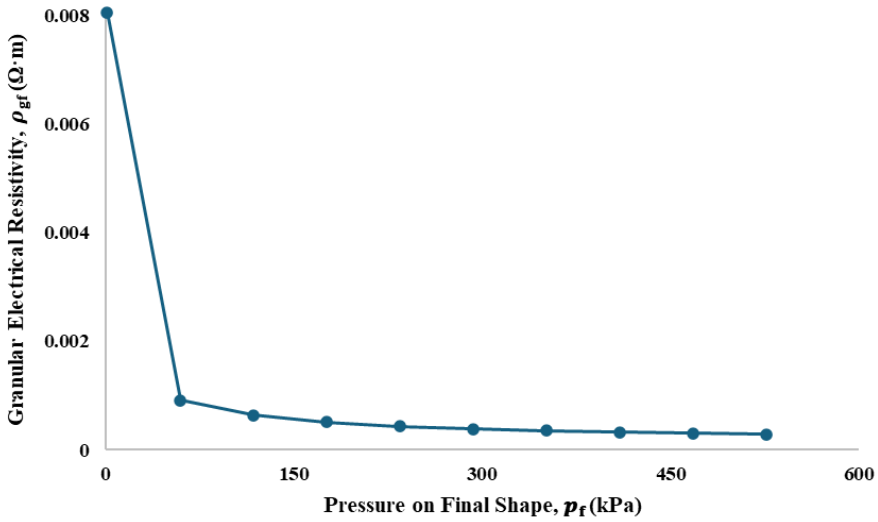

Figure 4-9 : Granular electrical resistivity of the puck

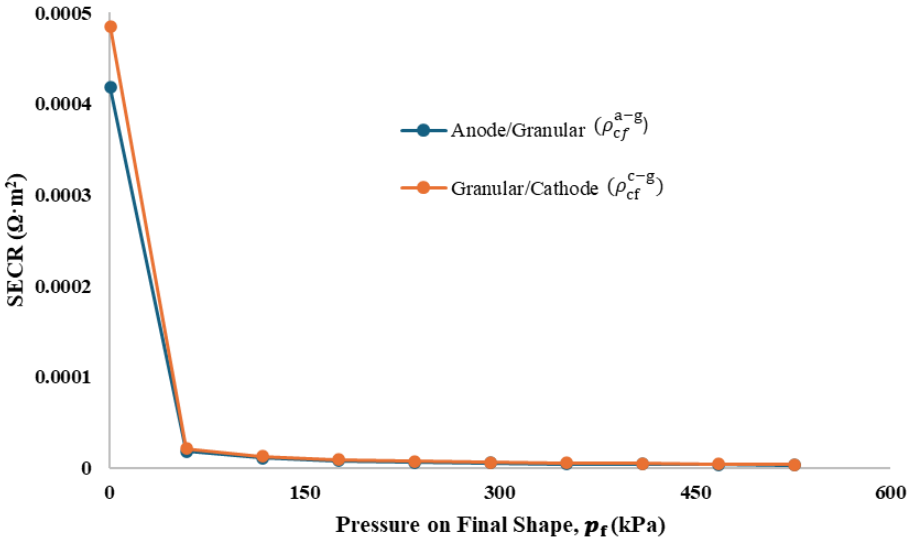

Figure 4-10 : SECR for both the contact surfaces of the puck

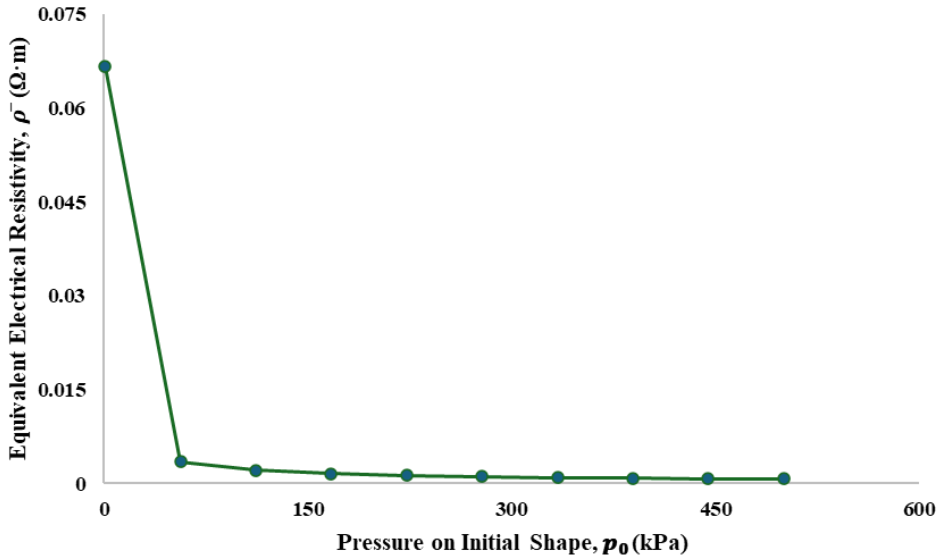

Figure 4-11 : Equivalent electrical resistivity of the puck

CHAPTER 5

OPTIMISATION OF THE LYING-BED PATTERN

The part of the work presented in this chapter was published in Light Metals 2024-Aluminium Reduction Technology and presented at the conference of TMS 2024 Annual Meeting & Exhibition, Orlando, Florida, USA. The paper was written in collaboration with Daniel Marceau[1], Simon-Olivier Tremblay[1], Duygu Kocaefe[1], Antoine Godefroy[2] and Sébastien Charest[2]. It was also presented as a poster in the JER 2023, Québec City, Québec, Canada.

[1] University Research Centre on Aluminium (CURAL) - Aluminium Research Centre (REGAL) - University of Québec at Chicoutimi (UQAC), Chicoutimi, Québec, Canada

[2] Aluminerie Alouette Inc. (AAI), Sept-Îles, Québec, Canada

5.1 General Information

This chapter presents the application of a numerical cell model to investigate the preheating behaviour of the electrolysis cell. The cell model is first introduced, followed by a detailed description of the underlying assumptions adopted to simplify the physical system while retaining the essential thermal and electrical characteristics of the cell. The accuracy and reliability of the developed model are established through a systematic calibration and validation process using relevant experimental and operational data. The

calibrated model demonstrates good agreement with measured values, confirming its suitability for analysing preheating phenomena.

Key performance indicators (KPIs) for cell preheating are also defined to quantitatively evaluate the preheating performance. These KPIs provide a structured basis for assessing the performance of preheating cells. Finally, simulations are carried out using the validated model to analyse the influence of operating parameters on preheating performance. The simulation results provide insights into the thermal, electrical and chemical responses of the cell and serve as a foundation for optimising preheating strategies and operating conditions.

5.2 The Finite Element Model

5.2.1 Description

Due to the double geometrical symmetry (both in material and physical appearance) of the electrolysis cell, only a quarter of the cell geometry is considered using the representative boundary conditions. To accurately represent the cell preheating behaviour, the model includes the proper geometry, material properties, and operational procedures. The TE ¼ cell preheating model (as shown in Figure 5-1) was developed and adapted to be able to consider various configuration of lying-bed. The transient and strongly coupled non-linear model was developed using the ANSYS^{TM} platform [22].

Different components of the aluminium reduction cell as described in Figure 5-1 are included in the model corresponding to the geometry and preparation of electrical cell preheating. Notice that the solid crushed bath occupies the remaining space under the anode yokes as the carbon blocks are fully covered to retain the heat. The top part (anode assemblies, cover product, and anode beam) is considered to better represent the heat propagation due to the joule heating of the coke and graphite mixture and hence to predict a more realistic temperature distribution in the whole cell. It is noteworthy to mention that the model can predict phase change of bath and baking of the ramming paste [22].

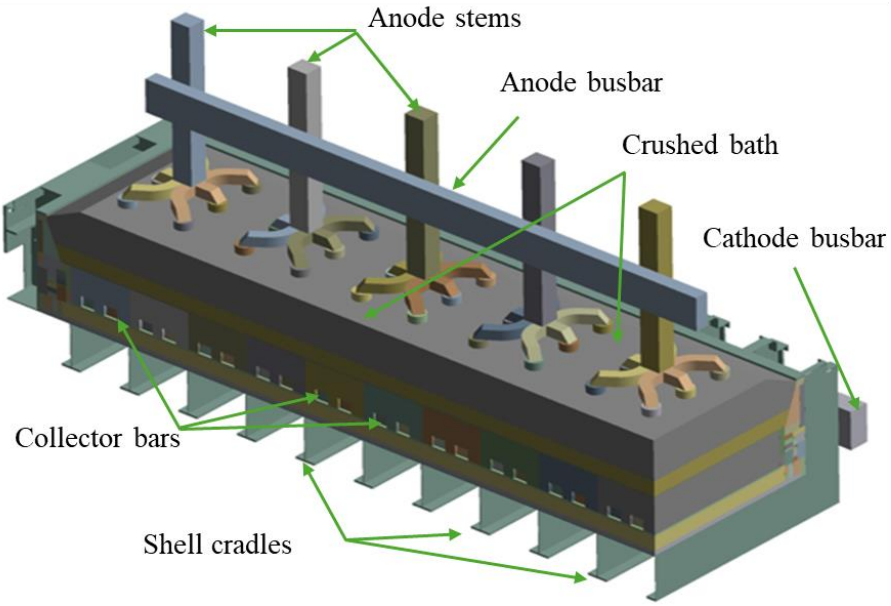

Figure 5-1 : Quarter cell model

5.2.2 Boundary Conditions

The used boundary conditions for the TE analysis, the key material properties, and the process parameters are described as follows [22]:

Thermo-electrical Boundary Conditions

1. Considering a cell operating at 384 kA, a current of 96 kA is applied at the connection surface between the positive risers and the anode beam.

2. Zero voltage (0 V) on the lower surface of the cathode busbar.

3. Ambient temperature of 37 ℃ at the exterior of the cell.

4. Initial temperature of 37 ℃.

5. Ambient temperature inside the cell: varying linearly from 37 ℃ to 140 ℃ (from measurements).

6. An equivalent heat transfer coefficient of 13 W/ m^2·K is applied on surfaces inside the cell (surfaces of anode crust, anode hexapods and anode stems) which is calibrated previously.

7. Equivalent heat transfer coefficient of the cathode shell is 10 W/ m^2·K.

Material Properties

1. Uniform specific electrical contact resistivity of 0.50 Ω·mm^2 is used at the cast iron-carbon interface (based on the measured voltage drop between the metal pad and the cathode bar during steady state).

2. Electrical resistivity of the bath at preheating: 10 Ω·m below 879 °C (solidus) and 0.004232 Ω·m above 955 °C (liquidus).

3. Enthalpy of fusion of electrolyte bath: 115.40 kJ/mol.

4. Electrical resistivity of the preheating resistive bed is 0.001300 Ω·m.

Process Parameters

1. No shunts (without bypassing any current with full line current 384 kA)

2. Preheating duration is 44 h.

5.2.3 Calibration and Validation

Cell behavior is particularly sensitive to some parameters such as lying-bed electrical resistance (mixture of coke and graphite) and the shell equivalent heat transfer coefficient (which includes both convection and radiation coefficients). However, they are also difficult to evaluate accurately. Some preliminary simulations are first carried out to validate the model by analysing the dependency on the finite element mesh, the calibration parameters, and comparing the *in situ* measurements with the simulation results. To do so, a measurement campaign was carried out at AAI. Then, the model has

been calibrated using available thermal, electrical and mechanical data obtained from *in situ* measurements from the AP4X electrolysis cells during its preheating phase. The details regarding the model development, calibration, and validation were briefly described in the literature [22].

Initially, the electrical resistance of the lying-bed was obtained from the calibration as 0.001300 Ω·m. Later this value is replaced by the experimental one (0.001169 Ω·m).

5.3 Lying-bed Patterns under Investigation

Various lying-bed patterns are designed to negate and mitigate some of the specific problems encountered during and after cell start-up. The main intent is to:

1. Avoid the frozen bath on the cathode surface (specially in the 4 cell corners).
2. Maximise the baking level of the ramming paste.
3. Disperse and distribute the central hottest temperature zone (as illustrated in Figure 1-15) throughout the cathode surface.

Redistribution of the cathode surface temperature, which will also reduce the global thermal gradients during the preheating phase, can be an option to avoid the deposition of frozen bath at the corners and to increase the baking level of peripheral ramming paste. The dispersion and distribution of above mentioned hottest central zone are done by changing the lying-bed patterns.

Initially, the simulation is carried out for the reference pattern (Pattern-R) as shown in *APPENDIX 3 : Pattern-R* which is used in the industries for reduction cell preheating. Appendix 3 has been withheld from this document due to confidentiality constraints related to proprietary information. Various lying-bed patterns are suggested considering the variation in the cathode heat flux. In this work, two better performing new lying-bed patterns are discussed and their impact on the cell preheating is compared with the existing reference pattern.

Pattern-1 (*APPENDIX 4 : Pattern-1*) is created with the objective of obtaining a more uniform heat flux along the long side of the cell and keeping the pattern density (the total surface area of lying-bed per anode) uniform under each anode per anode assembly.

Pattern-2 (*APPENDIX 5 : Pattern-2*) is created to get more uniform heat flux in both sides of the cell by keeping non-uniform pattern density. Under each anode per anode assembly, the total surface area of lying-bed is varied to obtain this pattern.

5.4 Preheating Key Performance Indicators

To evaluate the quality of the cell preheating process, the focus is placed on the identification of the key performance indicators (KPIs) in collaboration with our industrial partner. The identified KPIs are the mixture of the PIs that already existed in the literature (as mentioned in the Table 2-1) and the newly established KPIs for the dry start-up of modern reduction cells (using semi- or fully-graphitic/graphitised cathode blocks). They are as follows [31]:

1. Initial bath melt coverage
2. RSD of cathode surface temperature.
3. Average heating rate of cathode.
4. RSD of anode current distribution.
5. Baked portion of the ramming paste.
6. Baked portion of the ramming paste on end/corner zone.

It is noteworthy that the above-listed key performance indicators are not limited to evaluating the cell preheating quality of dry start-up; they can also be applied to assess preheating quality in the more commonly used method involving bath addition from other cells. In the latter case, the first KPI—initial bath melt coverage—should be excluded, while the remaining KPIs remain applicable. All the KPIs are briefly discussed with their acceptable limits subsequently. Furthermore, how the each KPI with respect to the acceptable limits affects performance is established.

Initial Bath Melt Coverage

Initial bath melt coverage is the percentage of cathode surface available/usable for initial bath melting. In other words, at the end of the preheating (*i.e.*, after 44 h), the relative cathode surface having temperature exceeding 955 ℃ is considered as the initial bath melt coverage. This is the ratio between cathode surface having temperature exceeding

955 °C and the total cathode surface and is expressed in percentage. Figure 5-2 shows the variation in the performance with respect to the initial bath melt coverage.

As we are dealing with the dry start-up where initial bath production occurs on the cathode surface, this KPI is very important for the efficient initial bath production. It shows the relative availability of the cathode surface area for the initial bath melting. The KPI performance is assigned as 1 if the utilized surface area for the initial bath generation is equal or more than 50%. The KPI performance drops drastically from 1 towards 0 as the utilized surface area for initial bath generation reduces from 50% towards 20%.

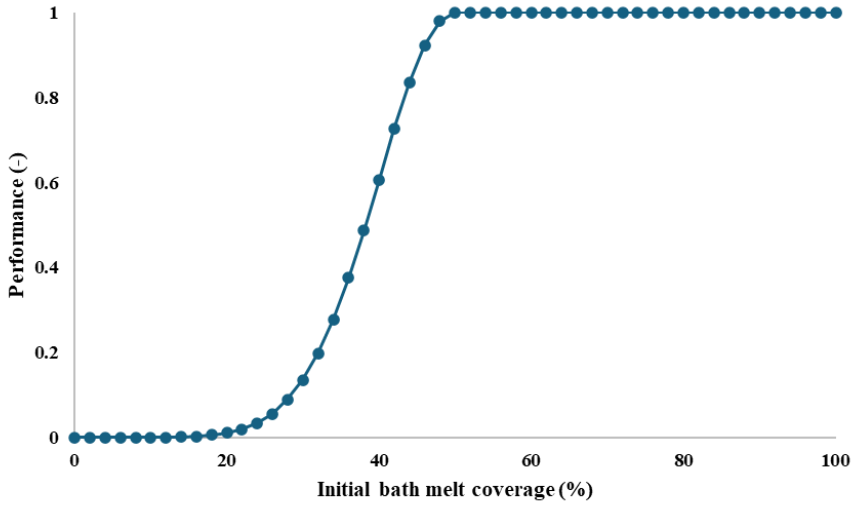

Figure 5-2 : Initial bath melt coverage

RSD of Cathode Surface Temperature

RSD of cathode surface temperature is the ratio of the population standard deviation of cathode surface temperature to the mean cathode surface temperature, expressed as a percentage. The mean cathode surface temperature is calculated while considering the

temperature of the whole cathode top surface from the model after 44 h of preheating. Figure 5-3 illustrates the established variation in the performance with respect to the RSD of cathode surface temperature.

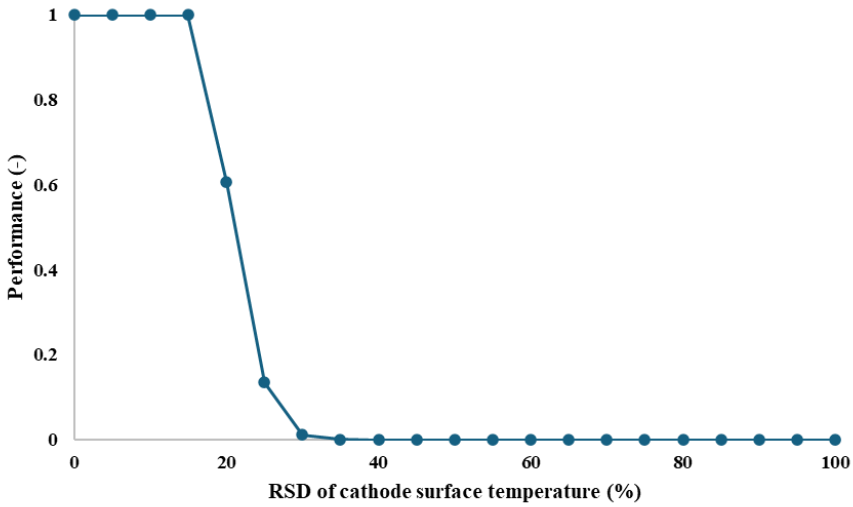

Figure 5-3 : RSD of cathode surface temperature

It conveys the variability in the cathode surface temperature in relation to its mean. In other words, it shows the uniformity of the cathode surface temperature. The lower the RSD, the higher the uniformity. The KPI performance is assigned as 1 if the RSD values are equal or less than 15%. The KPI performance drops drastically from 1 towards 0 as the RSD values increase from 15% towards 35%.

Average Heating Rate of Cathode

Average heating rate is calculated during the first 20 h of preheating and is expressed in °C/h. As reported in the literature [22], our model predicts that the initiation of bath melting happens during the 21st hour. Once it starts melting, it disturbs the electrical

current path, which makes cathode heating non-uniform. In addition, the electrical energy used to melt the crushed bath reduces the heating rate of the cathode. So, the evolution of the cathode surface temperature during the first 20 hours is considered.

The heating rate is calculated from the model using the average cathode surface temperature in the central channel. Figure 5-4 indicates variation in performance with respect to the average heating rate. In cathode preheating, high heating rates increase thermal gradients and the risk of thermal shock, whereas very low heating rates prolong preheating duration; therefore, a moderate heating rate is preferred. So, the KPI performance is assigned higher values for the moderate heating rates (where 35 °C/h being the peak) and the lower values for the heating rates that deviate in both sides from the peak. Hence, the KPI curve takes the shape of a normal distribution curve.

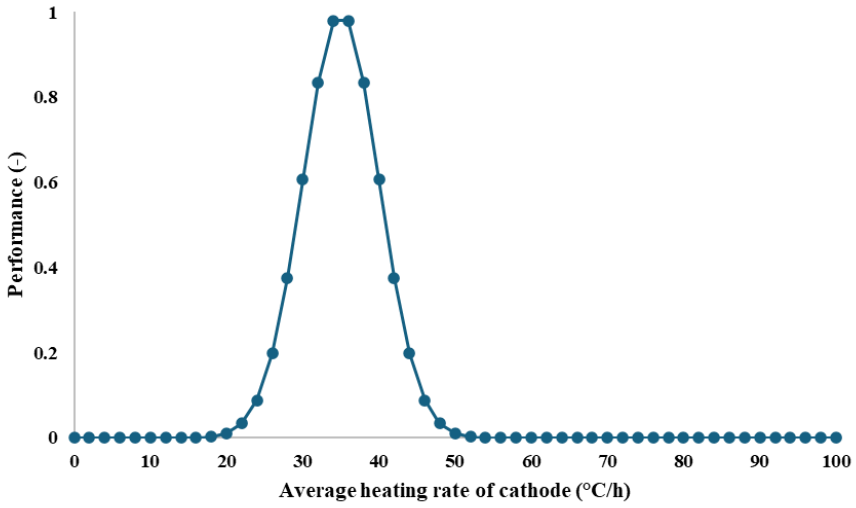

Figure 5-4 : Average heating rate of cathode (First 20 hours)

RSD of Anode Current Distribution

RSD of anode current distribution is defined in the similar manner to RSD of cathode surface temperature while considering the all the anodes from the model after 44 h of preheating. RSD of anode current distribution is calculated from the average anode current passing through each anode.

Figure 5-5 illustrates the established variation in the performance with respect to the RSD of anode current distribution. It conveys the variability in the anode current distribution in relation to its mean. In other words, it shows the uniformity of anode current distribution. The lower the RSD, the higher the uniformity. The KPI performance is assigned as 1 if the RSD values are equal or less than 35%. The KPI performance drops drastically from 1 towards 0 as the RSD values increase from 35% towards 80%.

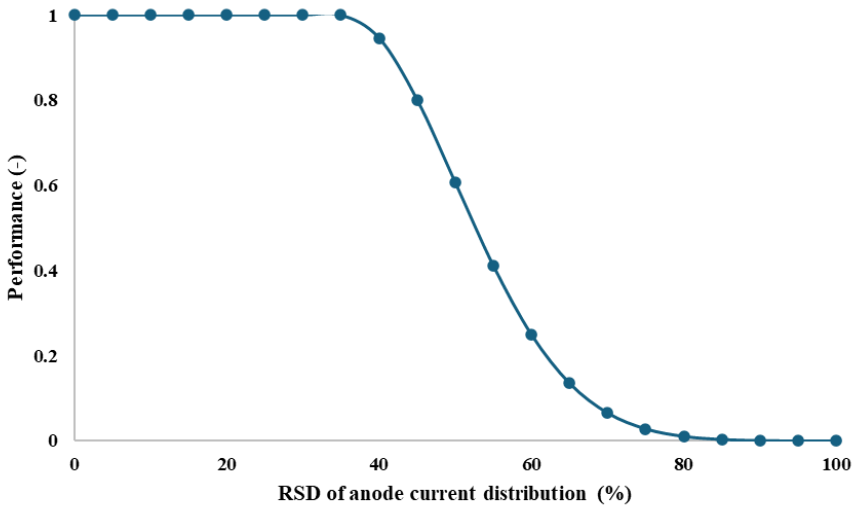

Figure 5-5 : RSD of anode current distribution

Baked Portion of Ramming Paste

Baked portion of the ramming paste is the percentage of the volume of ramming paste get baked at the end of the preheating (*i.e.*, after 44 h). In other words, at the end of the preheating, it is the relative volume of ramming paste exceeding 700 ℃. This is the ratio between volume of ramming paste exceeding 700 ℃ and the total volume of ramming paste (which includes all the inter-cathode block joints and all the peripheral joints of the whole cathode) and is expressed in percentages.

Figure 5-6 shows the variation in the performance with respect to the baked portion of ramming paste. It shows the relative baking of the ramming paste. The KPI performance is assigned as 1 if the baked portion of ramming paste is equal or more than 75%. The KPI performance drops drastically from 1 towards 0 as the baked portion of ramming paste reduces from 75% towards 45%.

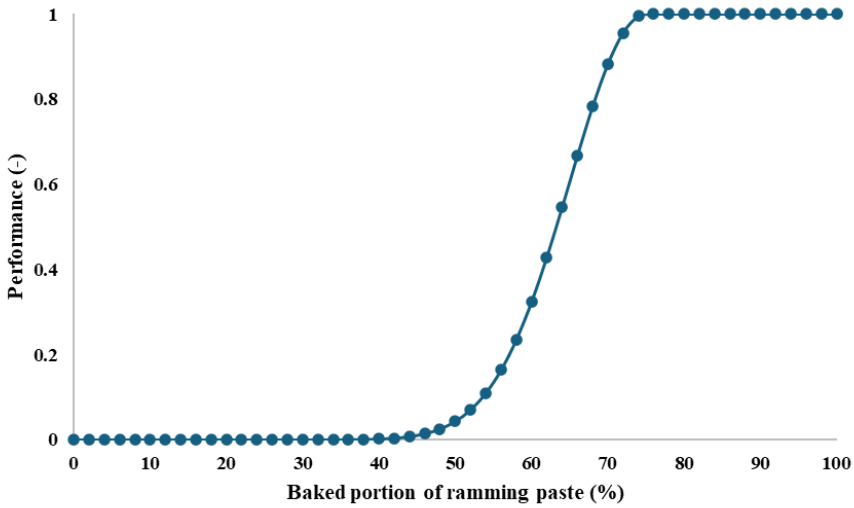

Figure 5-6 : Baked portion of ramming paste

Ramming paste has a typical characteristic property for different temperatures. It keeps on expanding initially and then shrinks as temperature increases further [74]. After reaching at 700 ℃, it can be assumed almost baked without any further significant expansion and shrinkage. Thus, 700 ℃ is considered as a reference temperature in the model to illustrate the baking level of ramming paste.

Baked Portion of Ramming Paste on End/Corner Zone

Baked portion of the ramming paste on end/corner zone is the relative volume of ramming paste exceeding 700 ℃ after 44 h. It is calculated at the vicinity of the two cathode assemblies (inter-cathode joints and peripheral joints which are covered under two extreme cathode assemblies) from the cell long-ends (which are tap end and duct end). The same reference temperature of 700 ℃ is considered due to the reason mentioned for the previous KPI.

Figure 5-7 shows the variation in the performance with respect to the baked portion of ramming paste on end/corner zone. It shows the relative baking of the ramming paste on the end and corner zone. The KPI performance is assigned as 1 if the baked portion of ramming paste is equal or more than 70%. The KPI performance drops drastically from 1 towards 0 as the baked portion of ramming paste reduces from 70% towards 40%.

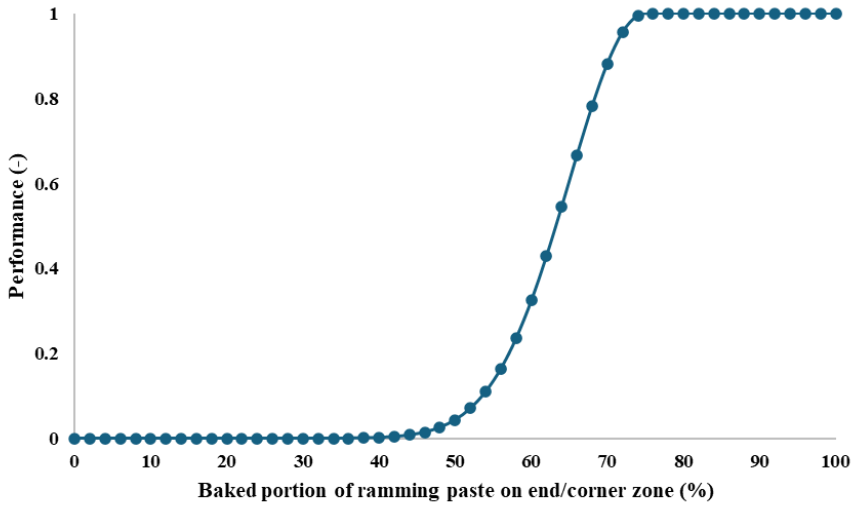

Figure 5-7 : Baked portion of ramming paste on end/corner zone

5.4.1 Evaluation of the Preheating Performance

The lying-bed patterns under investigation are evaluated by considering the previously discussed key performance indicators (KPIs) related to the thermal, electrical and chemical behaviour till now. Each KPI is assigned a weightage according to its importance after consulting with our industrial partner. All the previously discussed KPIs are summarised according to the associated physics, their acceptable range and their

respective weightage according to their importance in preheating (in accordance with our industrial partner-AAI) in the Table 5-1. The total weightage of all the performance indicators remains as a unit.

Table 5-1 : Weightage of KPIs for performance evaluation

No.	Key Performance Indicator (KPI)	Associated Physics	Acceptable range	Weight (W)
1	Initial bath melt coverage	Thermal	> 50% ± 10%	0.15
2	RSD of cathode surface temperature	Thermal	< 15% ± 5%	0.20
3	Average heating rate of cathode	Thermal	35 $°C/h$ ± 10 $°C/h$	0.20
4	RSD of anode current distribution	Electrical	< 35% ± 15%	0.10
5	Baked portion of ramming paste	Chemical	> 75% ± 10%	0.15
6	Baked portion of ramming paste on end/corner zone	Chemical	> 70% ± 10%	0.20
			Total :	**1.00**

Thus, the global performance (GP) of cathode preheating for different lying-bed patterns is therefore defined as:

$$\mathrm{GP} = \sum_{i=1}^{6} (KPI)_i \cdot W_i \quad \text{where,} \quad \sum_{i=1}^{6} W_i = 1 \qquad \textbf{(5-1)}$$

5.5 Simulation Results and Performance Evaluation

The preheating of the reduction cell for various lying-bed patterns is simulated using a transient, strongly coupled, thermo-electrical ¼-cell model developed with ANSYS™ including phase change of bath and baking of the ramming paste. The obtained results are compared to determine the best lying-bed pattern in terms of previously identified key performance indicators, which define the quality of cathode preheating.

Figure 5-8 shows the chosen temperature measurement locations in the model from where they can also be measured practically in the real cell, which will be helpful during industrial trial in future.

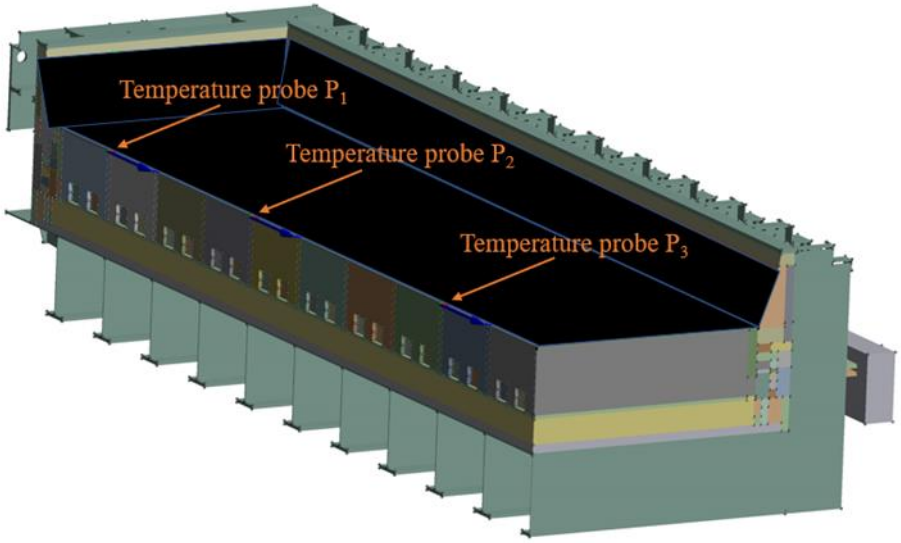

Figure 5-8 : Temperature probe location along the central channel

Thermal Key Performance Indicators

Figure 5-9 indicates the average central channel cathode surface temperatures for both the reference (Pattern-R) and the new patterns under investigation (Pattern-1 and Pattern-2). There is not much variation among the average cathode surface temperatures, which is reflected in the RSD of the cathode surface temperature and average heating rate of cathode (See Table 5-2). RSD of the cathode surface temperature remains similar for all the patterns under investigation whereas the average heating rates are slightly lowered as compared to Pattern-R, which are in acceptable range.

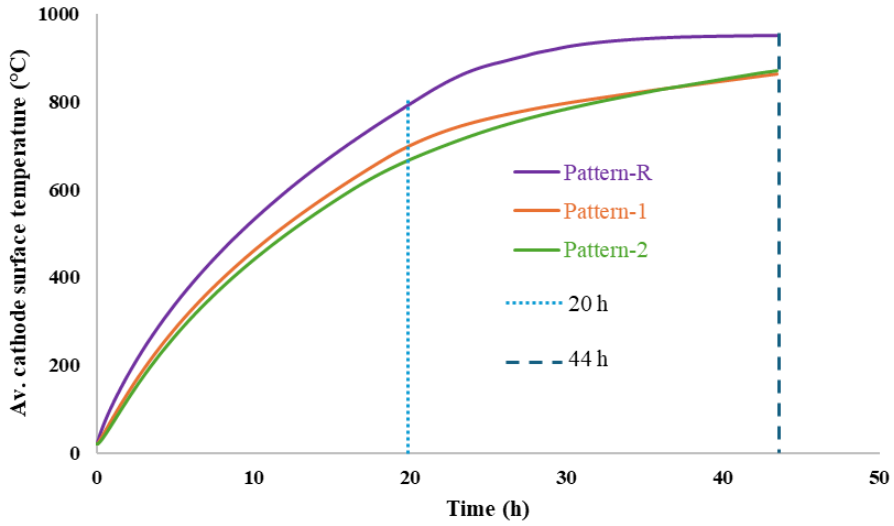

Figure 5-9 : Evolution of average cathode surface temperatures

As shown on Figure 5-10, Pattern-1 shows a slightly better cathode surface temperature distribution. The initial bath-melting zone is right in the center of the cell for Pattern-R. Both new patterns displace the initial bath melting zone obtained with Pattern-R. It shifts from the center of the cell towards the peripheral zone. In the case of Pattern-2, it is more

towards the cell long-end close to the corner, which is necessary to melt the bath and avoid undesirable deposition of frozen bath on the peripheral cathode surface. Figure 5-10 gives a clear idea regarding the cathode surface temperature distribution for all patterns. It can be observed that the hottest central zone seen in Pattern-R is split and is dispersed around the cathode surface into four parts, one in each quarter of the cathode.

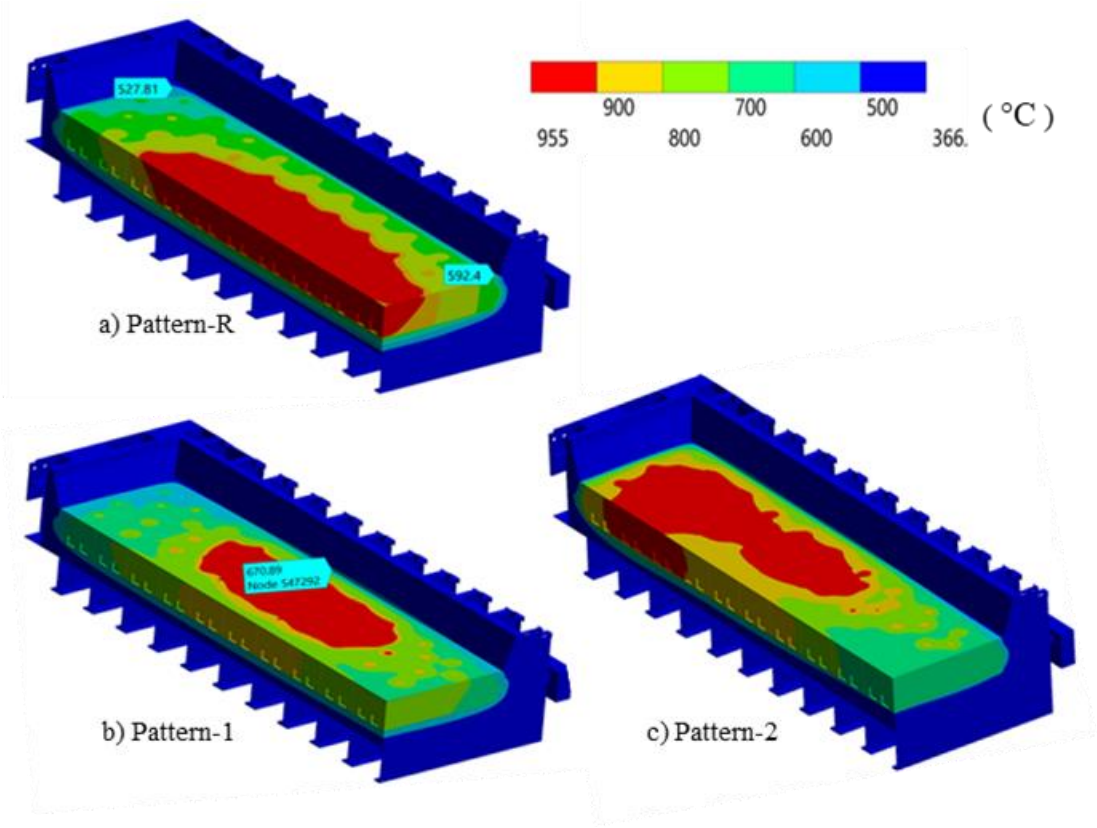

Figure 5-10 : Cathode surface temperature distributions

The available cathode surface for initial bath melting is reduced by 3% in the case of new patterns as compared to the reference. It is due to the splitting and dispersion of the central hot zone towards the periphery, which gives slightly more heat loss towards the potshell.

Electrical Key Performance Indicator

RSD of the anode current distribution (Table 5-2) for all the patterns are in the industrial acceptable limits, although it appears to be slightly higher for the new patterns under investigations. It is important to manage the anode current distribution during preheating carefully to avoid any anode failure.

Chemical Key Performance Indicators

It can be seen in that the peripheral cathode surface temperature distribution for both the new patterns is better than that of the reference case (Figure 5-10), which allows for a better baking level of the peripheral ramming paste. From Table 5-2, it should be noted that the baking level of ramming paste is slightly increased when compared to the reference case as there is a slight increase in the KPI— baked portion of the ramming paste. In addition, Figure 5-11 shows the baking level of ramming paste used for the quarter-cathode for all the patterns under investigation. Both the new patterns show better results in terms of baked portion of the ramming paste, but Pattern-2 shows a significant improvement in the baked portion of ramming paste on end/corner zone (Table 5-2).

It can be seen from the Table 5-2 that Pattern-2 performs better, whether the performance is evaluated using the previously assigned weighting factors or by assigning equal importance to all criteria.

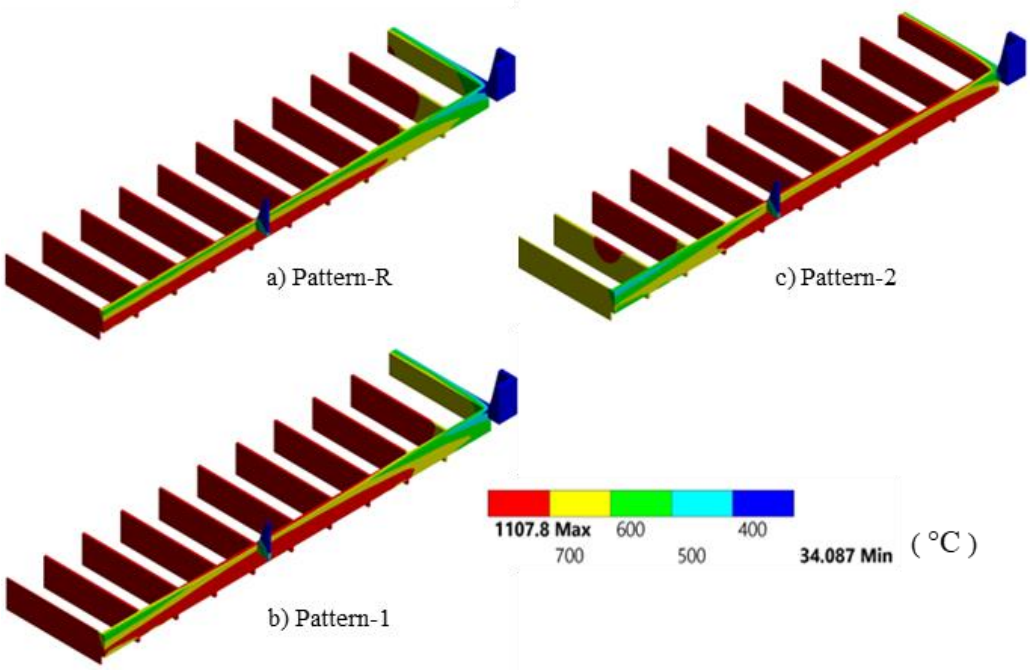

Figure 5-11 : Baking level of ramming paste

Table 5-2 : Global performance of the lying-bed the patterns

No.	Key Performance Indicator (KPI)	Pattern-R	Pattern-1	Pattern-2
1	Initial bath melt coverage (%)	39	36	36
2	RSD - cathode surface temperature (%)	16.9	14.6	16.5
3	Average heating rate ($°C/h$)	37.8	34.9	33.5
4	RSD - anode current distribution (%)	26	43	39
5	Baked portion of ramming paste (%)	69	73	72
6	Baked portion of ramming paste on end/corner zone (%)	28	33	70
Global Performance (GP) with the assigned weightage:		**0.66**	**0.69**	**0.87**
Global Performance (GP) with equal weightage:		**0.69**	**0.70**	**0.86**

As shown in Figure 5-9, the average cathode surface temperature in the central channel stays below 900 °C for both new patterns at the end of the preheating phase (*i.e.*, after 44 hours). To achieve the desired cathode surface temperature in the central channel, the preheating time needs to be extended. Furthermore, in case of Pattern-2, approximately 4 hours of extra preheating time is required to reach 900 °C as shown in Figure 5-12.

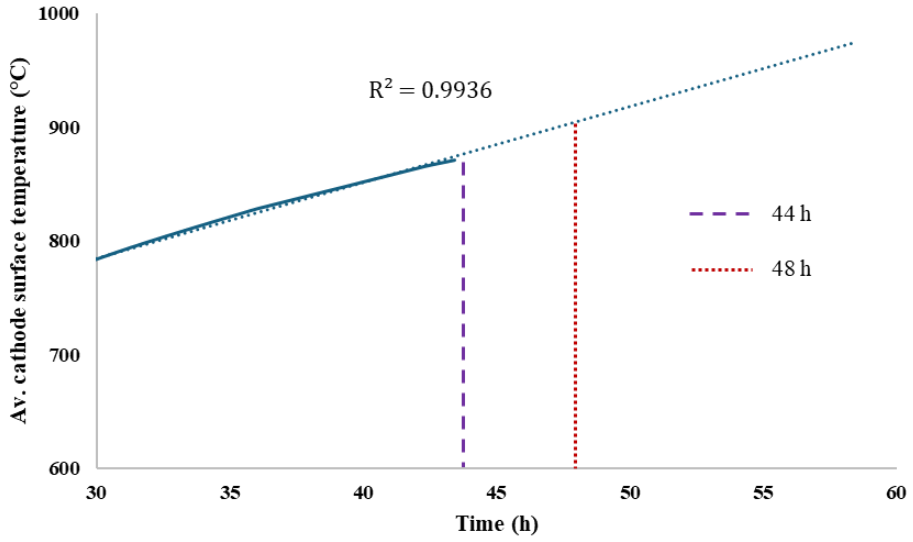

Figure 5-12 : Extension of the preheating time for lying-bed pattern-2

It is important to manage carefully the anode current distribution during preheating to avoid any anode failure in real cell by taking the following measures:

1. Frequent monitoring of anode current distribution
2. Finding the faulty anodes which draw excess current
3. Adding crushed bath on the cathode around the faulty anodes

4. Providing air cooling at bimetallic joints of all the susceptible anodes

5. If required, isolating the faulty anode.

6. Finding the faulty anodes that draw too low current.

7. And then loosen and retighten the anode clamps.

Both the new patterns have shown improved results with respect to the reference case. Pattern-2 gives promising results in terms of baked portion of ramming paste at the end/corner zone and average heating rate of the cathode.

It can be useful for preheating of cells not only for better preheating performance, but also to avoid frozen bath on the corner of the cathode surface, which affects adversely towards the stability of newly started cells.

The central zone of the cell has comparatively lower temperature at the end of the preheating phase. The converged bath in the central zone melts eventually during the bath up phase as the bath temperature in the middle of the cell becomes high enough to melt those incomplete-melted crushed baths.

CHAPTER 6

CONCLUSION AND RECOMMENDATIONS

6.1 Retrospective

This study set out to resolve some of the challenges faced during aluminium reduction cell start-up particularly in its preheating phase which plays a vital role in the cathode life. It reflects a comprehensive effort to understand and address the problems encountered during cathode preheating and its subsequent impact on cathode life.

In this process, it is very important to understand the behaviour of the granular material under different conditions as imposed in the real electrolysis cell. Furthermore, the behaviour of granular material is studied which is used for the *lying-bed*. The physical and the electrical properties of the granular blends are experimentally determined.

The physical properties of the granular blends are used to optimise the puck shape and geometry in the *lying-bed*. New *lying-bed* patterns are designed and tested by simulations using ANSYS^{TM} using the experimentally determined electrical properties of the granular blends. Through a combination of experimental data and simulations, the results from the new *lying-bed* patterns look promising to obtain the better cathode preheating conditions which have a beneficial effect on cathode longevity.

This will impact the aluminium smelters positively by reducing the cathode cost per tonne of Al produced and the environment by reducing the harmful effects due to lesser spent pot linings per tonne of Al produced.

6.2 Highlights

The main highlights of the project are summarised below:

1. Physical properties of the granular blends like angle of repose, axial strain and diametral strain are obtained to optimise the puck geometry in the *lying-bed.* Additionally, the effect of granular blend composition on these properties is also studied.
2. Electrical properties of the granular blends like electrical resistivity and specific electrical contact resistivities (SECR for both the anode and the cathode contact surfaces) are experimentally determined as a function of temperature and pressure which is used to simulate the *lying-bed* patterns more precisely. Furthermore, the impact of granular blend composition on these electrical properties is also investigated.
3. Key performance indicators (KPIs) for aluminium reduction cell preheating are established for the modern cells using (semi- or fully-) graphitic and graphitic cathodes for dry start-up.

4. Baking of the ramming paste specifically in the corner zone of the cathode has substantially increased during the preheating using Pattern-2 which is crucial for the cathode integrity.

6.3 Originality

Although the original aspects are not required for a master's degree project, this project has its originalities and uniqueness. As it can be seen in the literature review chapter, section 2.7 (*Study of the Cathode Preheating in Past Years*), all the researchers have only recommended reducing the thermal stress in the cathode by reducing the thermal gradient during the preheating phase. The most prominent published study on the *lying-bed* pattern was done by Arkhipov *et al.* in DX+ reduction cells [49] and Reny *et al.* in HAL4e Ultra reduction cells [32]. However, they did not study and publish any characterisation of the granular materials under different conditions. They took it into account by means of a modification to the shape of the *lying-bed* pattern only. In the present study associated with AP4X cells, the original aspects are as follows:

1. Characterisation of the granular blends under different conditions. Experimental determination of physical properties and electrical properties of the granular blends as a function of temperature and pressure.
2. Identification of the key performance indicators for modern cells using dry start-up method to evaluate the quality of cathode preheating.

3. Redistribution of the pucks in the *lying-bed* (or modification of the *lying-bed* pattern) for better preheating results.

6.4 Recommendations

The outcomes of the experimental and simulation studies indicate several areas where further investigation and improvement are recommended.

Based on the findings of this thesis, future works should include the following points:

1. It is recommended that industry implement *lying-bed* configurations optimised through thermo-electrical analysis, with future integration of mechanical considerations to minimise cathode stress and enhance operational stability.
2. Particle size distribution (PSD) plays a critical role in determining both the physical and electrical properties of granular materials. Variations in PSD influence packing density, porosity and contact area between particles, which in turn affect mechanical stability and electrical resistivity. Thus, the influence of the PSD on these physical and electrical properties needs to be investigated.
3. Mechanical key performance indicators (KPIs), such as stress developed in the cathode and confinement of the cathode plane, should be included in the evaluation framework with appropriate weightage to assess mechanical performance. Incorporating these parameters would enhance the robustness and completeness of the study.

4. Extension of the model from TE to thermo-electro-mechanical (TEM) is necessary to adequately represent the coupled physical behavior of the reduction cell.

BIBLIOGRAPHY

[1] https://alfed.org.uk/aluminium-is-the-third-most-common-element-in-the-earths-crust-2/, Internet, [Cited 2025].

[2] https://millenniumalloys.ca/most-common-uses-of-aluminium/, Internet, [Cited 2025].

[3] https://natural-resources.canada.ca/our-natural-resources/minerals-mining/mining-data-statistics-and-analysis/minerals-metals-facts/aluminium-facts/20510, Internet, [Cited 2025].

[4] https://amcaluminium.ph/primary-vs-secondary-aluminium/, Internet, [Cited 2025].

[5] Grjotheim K, Welch B J, (1987) Aluminium Smelter Technology-A Pure and Applied Approach. Aluminium-Verlag GmbH, Düsseldorf, Germany.

[6] IAI, https://international-aluminium.org/statistics/primary-aluminium-production/, Internet, [Cited 2025].

[7] Fortune Business Insights (FBI), 24 March 2025, Report ID: FBI100233. https://www.fortunebusinessinsights.com/industry-reports/aluminium-market-100233 .

[8] Grjotheim K, Kvande H, (ed) (1993) Introduction to Aluminium Electrolysis- Understanding the Hall-Héroult Process. Aluminium-Verlag GmbH, Düsseldorf, Germany.

[9] HYDRO, https://www.hydro.com/en/media/on-the-agenda/hydros-roadmap-to-zero-emission-aluminium-production/halzero-zero-emission-electrolysis-from-hydro/, Internet, [Cited 2025].

[10] ELYSIS, https://www.elysis.com/fr/elysis, Internet, [Cited 2025].

[11] RUSAL, https://rusal.ru/en/innovation/technology/inertnyy-anod/, Internet, [Cited 2025].

[12] Kvande H, (2017) TMS Industrial Aluminium Electrolysis Course – The Course on Theory and Practice of Primary Aluminium Production, Reykjavík, Iceland.

[13] Barber M, Tabereaux A, (2013) The evolution of Söderberg aluminium cell technology in North and South America. JOM, December 2013, p 223-234.

[14] Gao B, Wang Z, Shi Z, Hu X (2017) History and recent developments in aluminium smelting in China. ICSOBA Proceedings 2017, p 53-68.

[15] Heil J, (2014) Aluminium reduction cell technology providers - a 2014 review. AWJ 2014.

[16] Tabereaux A, (2017) Super-high amperage prebake cell technologies in operation at worldwide aluminium smelters. Light Metal Age, February 2017,p 30-32.

[17] Hall A, (2018) Arabal 2017: Advances in Primary Aluminium Technology and Sustainability. Light Metal Age Magazine.

[18] Bearne G, Gadd D, Lix S, (2007) The impact of slots on reduction cell individual current variation. Light Metals 2007, p 305-310.

[19] Kvande H, (2013) TMS Industrial Aluminium Electrolysis Course – The Course on Theory and Practice of Primary Aluminium Production. Doha, Qatar.

[20] UK Patent, (2015) Superstructure for electrolytic cell, comprising means of moving anode beam with respect to the frame of this superstructure, Dubai Aluminium, UAE. GB2543788A.

[21] Kvande H, (2000) Electrolyte compositions for aluminium production-Options and Desirable Properties. Semantic Scholar.

[22] Tremblay S-O *et al.* (2023) Numerical Investigation of Thermal, Electrical and Mechanical Behaviour of Aluminium Cell during preheating phase." TMS Light Metals 2023, p 765-772.

[23] Zangiacomi C *et al.* (2005) Preheating study of smelting cells. TMS Light Metals 2005, p 333-336.

[24] Hale W.R. (1989) Improving the useful life of aluminum industry cathodes, JOM Vol. 41, No. 11, p 20-25.

[25] Industrial sources.

[26] Yurkov A, (2017) Refractories for Aluminium – Electrolysis and the Cast House. Springer.

[27] Sørlie M, Øye H, (2010) Cathodes in Aluminium Electrolysis. Aluminium-Verlag GmbH, Düsseldorf, Germany.

[28] Ali M. M., (2013) Preheating and start-up of prebaked aluminium reduction cells. Journal of Engineering Sciences, Assiut University, Faculty of Engineering, Vol. 41, No. 6, November 2013, pp. 2354 - 2364.

[29] Reverdy M, Potocnik V (2022) A historical review of aluminium reduction cell start-up and early operation. Light metals 2022, p 991-997.

[30] Huang Y, (2025) 500 kA Cell Coke Preheating Optimisation. ICSOBA Proceedings 2025, p 1635-1642.

[31] Tripathy RN *et al.* (2024) Thermo-Electrical Analysis of Lying-bed Patterns during Preheating Phase. Light metals 2024, p 499-507.

[32] Reny P *et al.* (2016) Low Energy Start-up for Low Energy Cells. ICSOBA Proceedings 2016, p 485-496.

[33] Kvande H, (1996) The International Course on Process Metallurgy of Aluminium. NTNU, Trondheim, Norway.

[34] Ali M, M. *et al.* (2022) Thermal Behaviour of the Early Life of an Aluminium Electrolysis Cell. International Journal of Engineering Research in Africa, p 1663-4144, Vol 61.

[35] Rye K Å, (2008) Cell preheat/start-up and early operation. TMS Light Metals 2008, p 1007-1011.

[36] Krogerus H *et al.* (2006) Laboratory Investigation of the Electrical Resistivity of Cokes and Smelting Charge for Optimizing Operation in Large Ferrochrome Furnaces. Southern African Pyrometallurgy, Johannesburg, March 2006.

[37] Eidem P A *et al.* (2008) Determination of Electrical Resistivity of Dry Coke Beds, Metallurgical and Material Transactions. Volume 39B, February 2008, p 7-15.

[38] Surup G R *et al.* (2020) Electrical Resistivity of Carbonaceous Bed Material at High Temperature. Processes 2020, Department of Material Science and Engineering, NTNU, Norway, p 1-22.

[39] Miroshnichenko D *et al.* (2024) Electrical Resistance as an Aggregate Characteristics of Coke Properties for Electrochemical and Coke Production. MDPI, Electrochem 2024, 5.

[40] Paraskevoulakos C *et al.* (2022) Temperature Dependence of Electrical Resistivity, Deformation, and Fracture of Polygranular Graphite with Different Amounts of Porosity. SN Applied Sciences, Springer Nature.

[41] Gunter B, Eick I, (2007) Improvements in the Electrical Preheating of Hall-Héroult Pots. TMS Light Metals 2007, p 1001-1006.

[42] Asadi G V *et al.* (1992) Advances in Production and Fabrication of Light Metals and Metal Matrix Composites. 31st Annual Conference of Metallurgists of CIM, Alberta, Canada.

[43] Dupuis M, (2001) Thermo-electro-mechanical modelling of Hall-Héroult cell coke bed preheating, TMS Light Metals 2001, pp. 757-761.

[44] Dupuis M, Ghasem Asadi, (1993) Thermal study of the coke preheating for Hall-Héroult cell. TMS Light Metals 1993, pp. 93-100.

[45] Richard D *et al.* (2006) Thermo-chemo-mechanical modelling of a Hall-Héroult cell thermal bake-out. TMS Light Metals 2006, pp. 669-674.

[46] Ali M. M., (2010) Analysis of the coke bed preheating method for aluminium cells", TMS Light Metals 2010, pp. 1057-1062.

[47] Ali MM, Kvande H, (2017) Recent Advances in Electrical Resistance Preheating of Aluminium Reduction Cells. JOM, February 2017, p 266-280.

[48] Marceau D *et al.* (2011) Advanced numerical simulation of the thermo-elctro-chemo-mechanical behaviour of Hall-Héroult cells under electrical preheating. TMS Light Metals 2011, p. 1041-1046.

[49] Arkhipov A *et al.* (2015) A model-based study of cell electrical preheating practices at DUBAL. TMS Light Metals 2015, pp. 777-782.

[50] Borim A. *et al.* (2025) Optimizing Aluminium Reduction Cell Start-up- A Semi-Conventional Approach at Sohar Aluminium. ICSOBA Proceedings 2025, p 1663-1680.

[51] Welch B, Intensive Training Module (2016) Postgraduate Certificate in Light Metals Reduction Technology, Light Metals Research Centre, The University of Auckland, New Zealand.

[52] Reverdy M, Potocnik V (2021) History of Computer Control of Aluminium Reduction Cells. Light metals 2021, p 591-599.

[53] Kvande H, Drabløs P A (2014) The Aluminium Smelting Process and Innovative Alternative Technologies. JOEM, Vol 56 5S, May 2024, p 23-32.

[54] A Wright (1993) The Dynamic Simulation and Control of Aluminium Smelting Cells. PhD Thesis, University of Newcastle, England.

[55] Till Carsten Reek (2015) Power Modulation of Aluminium Reduction Cells – Operational Constraints and Process Limits. PhD Thesis, UNSW, Sydney, Australia.

[56] Jayson Tessier (2010) Multivariate Statistical Analysis of Hall-Héroult Reduction Cells. PhD Thesis, UL, Quebec, Canada.

[57] Pascale Lavoie (2021) On the Factors Affecting Alumina Dissolution in Industrial Reduction Cells. PhD Thesis, UoA, New Zealand.

[58] Steinar Kolås (2008) Estimation in Nonlinear Constrained Systems with Severe Disturbances. PhD Thesis, NTNU, Norway.

[59] Tabereaux A, Dupuis M, (2019) Key Performance Indicator Comparisons of Global State-of-the-Art Aluminium Cell Technologies. Primary Smelting and Processes, AWJ 2019, p 14-20.

[60] Welch B, (2016) Specific energy consumption and energy balance of aluminium reduction cell. VIII International Congress & Exhibition Non-Ferrous Metals and Minerals, Krasnoyarsk, Russia, September 2016.

[61] Curtolo D C *et al* (2021) High and Ultra-High Purity Aluminium, a Review on Technical Production Methodologies. Metals 2021, Vol 11, p 47-61.

[62] Lindsay S J (2014) Very High Purity Aluminium: An Historical Perspective. JOM Vol 66.

[63] Khaji K *et al.* (2016) The Role of Anode Manufacturing Processes in Net Carbon Consumption. Metals 2026, Vol.6, p 6-18.

[64] Fournier-Sowinski J, (2024) Practical Handbook of Grain Size Analysis Principles and Methods. Marine Station MNHN, Concarneau, 75.

[65] Holtz, R D, Kovacs W. D., (1981) An Introduction to Geotechnical Engineering. Prentice-Hall.

[66] Das B M, (2010) Principles of Geotechnical Engineering. Cengage Learning.

[67] Dieter G E, (1986) Mechanical Metallurgy. McGraw-Hill.

[68] Kasap S O, (2017) Principles of Electronic Materials & Devices. McGraw-Hill.

[69] Rhedey PJ, Castonguay L (1985) Effects of Carbonaceous Rodding Mix Formulation on Steel-Carbon Contact Resistance. Light metals 1985, AIME, p 555-563.

[70] Mathieu Rouleau (2007) Caractérisation thermo-électro-mécanique des interfaces fonte-acier-carbone ans une cuve d'électrolyse. Master's thesis, UQAC.

[71] Braunovic M, Myshkin N K, Konchits V.V., (2007) Electrical Contacts: Fundamentals, Applications and Technology. CRC Press.

[72] Tripathy RN *et al.* (2026) Granular Blends of Coke and Graphite in the Lying-beds: Experimental Insights into Their Mechanical and Electrical Properties. TMS Light Metals 2026, p 813-821.

[73] Carl Laberge (2003) Caractérisation thermoélectrique du lit de coke utilise lors du préchauffage d'une cuve d'électrolyse de type Hall-Héroult. Master's thesis, UQAC.

[74] Hiltmann F, Muelemann K-H, "Ramming paste properties and cell performance", TMS Light Metals 2000, pp. 405-411.

APPENDIX 1 : ELECTRICAL TEST EXPERIMENT PLAN

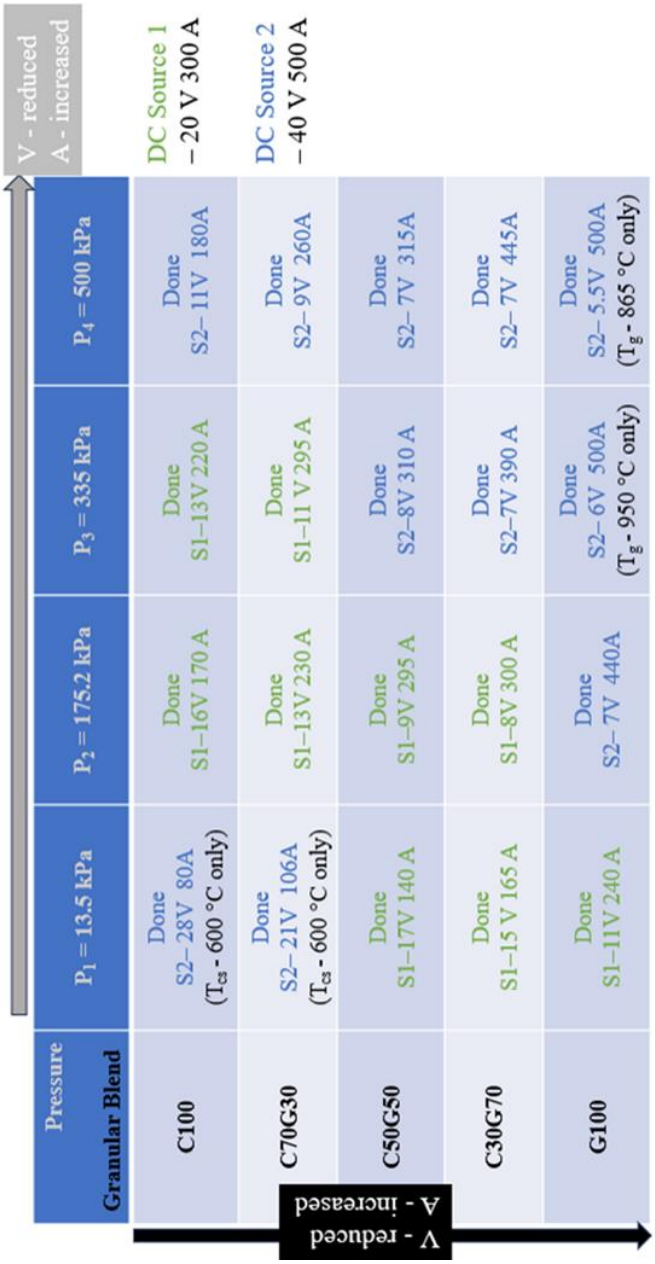

Figure A-1 : Experimental plan for electrical test

APPENDIX 2 : EFFECT OF FLOWABILITY AND LOAD ON GRANULAR BLEND

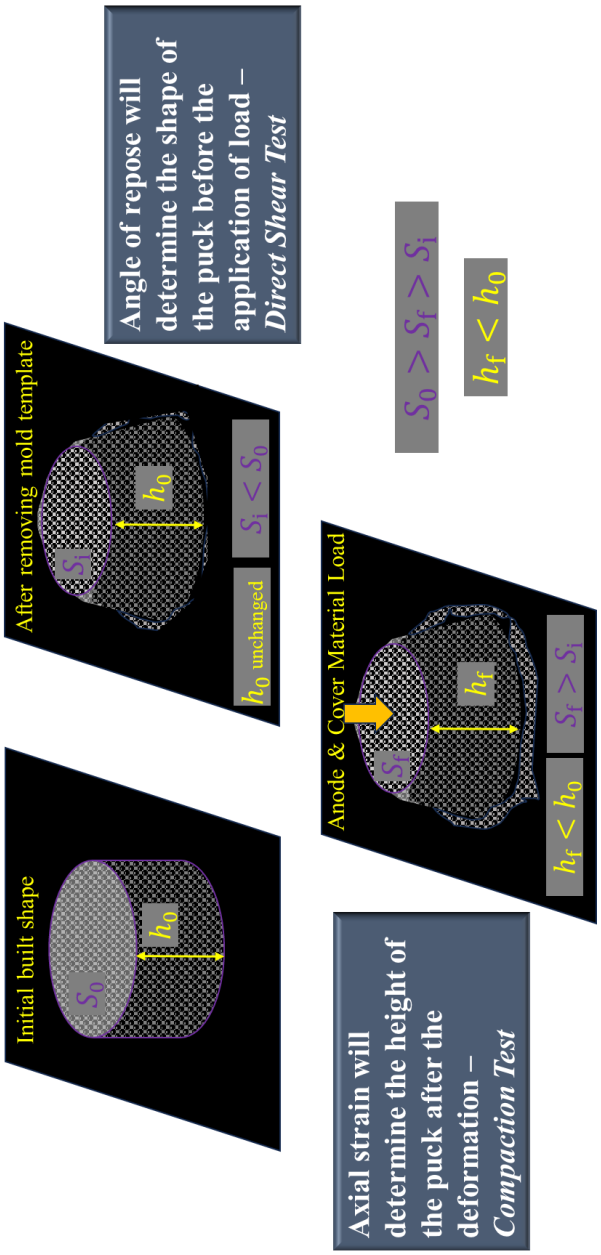

Figure A-2 : Effect of flowability and load on the granular blend

APPENDIX 3 : PATTERN-R

Hidden due to confidential information.

Figure A-3 : Pattern-R

APPENDIX 4 : PATTERN-1

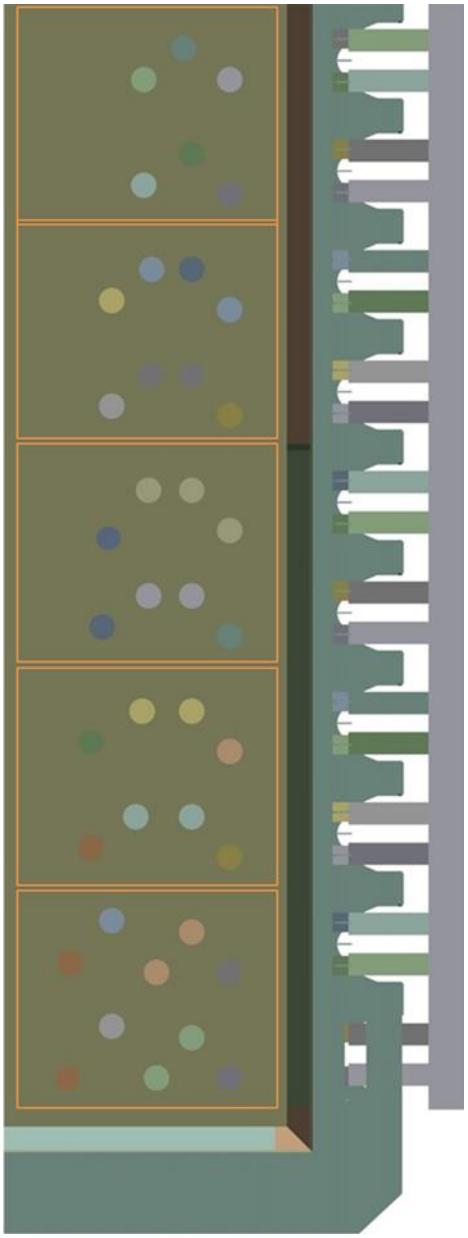

Figure A-4 : Pattern-1

APPENDIX 5 : PATTERN-2

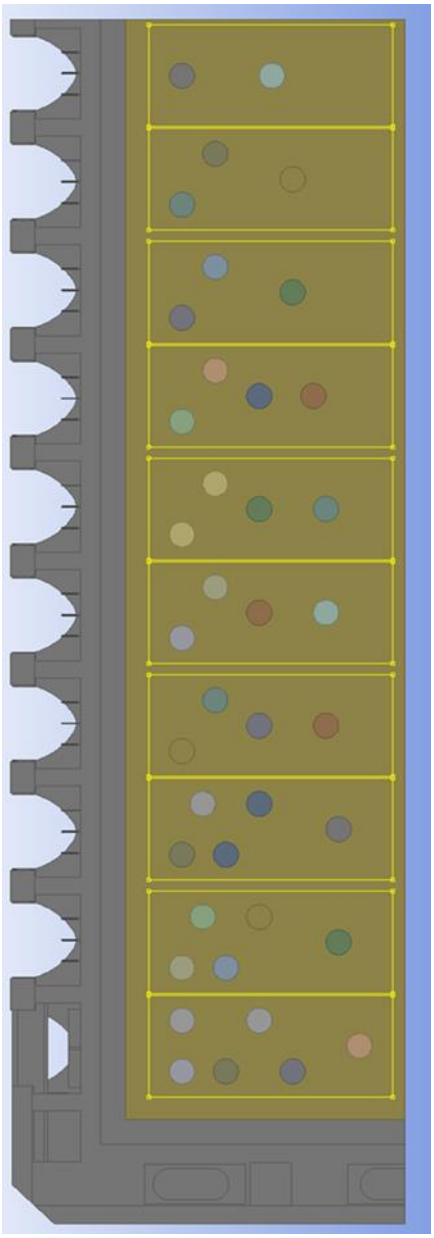

Figure A-5 : Pattern-2

APPENDIX 6 : POSTERS

1. **"Optimisation of the resistive-Bed for the Preheating of Electrolysis Cells"**

   "Optimisation du lit résistif pour le préchauffage des cellules d'électrolyse"

   Tripathy RN, Marceau D, Tremblay SO, Kocaefe D, Godefroy A & Charest S

   JER, 11-13 October 2023, Québec city, Québec, Canada (20th Edition)

   Encyclopédie de la recherche sur l'aluminium au Québec 2023 - https://regal-aluminium.ca/publications-et-outils/

2. **"Resistive-Bed Optimisation: A Key to Enhanced Preheating Performance in Electrolysis Cells"**

   "Optimisation du lit résistif : une clé pour améliorer les performances de préchauffage dans les cellules d'électrolyse"

   Tripathy RN, Marceau D, Tremblay SO, Kocaefe D, Godefroy A & Charest S

   JER, 16-18 October 2024, Chicoutimi, Québec, Canada (21st Edition)

   Encyclopédie de la recherche sur l'aluminium au Québec 2024 - https://regal-aluminium.ca/publications-et-outils/

3. **"Enhancing Aluminium Reduction Cell Preheating via Lying-bed Optimisation"**

   "Amélioration du préchauffage de cuve d'électrolyse grâce à l'optimisation du lit résistif chauffant"

   Tripathy RN, Marceau D, Tremblay SO, Kocaefe D & Godefroy A

   JER, 14-15 October 2025, Trois-Rivières, Québec, Canada (22nd Edition)

   Encyclopédie de la recherche sur l'aluminium au Québec 2025 - https://regal-aluminium.ca/publications-et-outils/

APPENDIX 7 : PUBLICATIONS

1. **"Numerical Investigation of Thermal, Electrical and Mechanical Behaviour of Aluminium Cell during Preheating Phase"**,

   Tremblay S-O, Marceau D, Tripathy RN, Kocaefe D, Godefroy A, Charest S & Coté J.

   TMS Light Metals 2023, p 765-772

2. **"Thermo-Electrical Analysis of Lying-bed Patterns during Preheating Phase"**,

   Tripathy RN, Marceau D, Tremblay S-O, Kocaefe D, Godefroy A & Charest S.

   TMS Light Metals 2024, p 499-507

3. **"Granular Blends of Coke and Graphite in the Lying-beds : Experimental Insights into Their Mechanical and Electrical Properties"**,

   Tripathy RN, Marceau D, Kocaefe D & Godefroy A.

   TMS Light Metals 2026, p 813-821

4. **"Optimization of the Lying-bed Pattern for the Preheating of Aluminium Reduction Cell"**,

   Marceau D, Tremblay S-O, Tripathy RN, Kocaefe D, Godefroy A & Dubé D.

   (In progress & to be published in ICSOBA Proceedings 2026)